

Frequency sensitive moment tensor inversion for light
to moderate magnitude earthquakes in eastern Africa
and derivation of the regional stress field

Frequenzabhängige Momententensorinversion für
schwache bis mittelstarke Erdbeben im östlichen Afrika
und Ableitung des regionalen Spannungsfeldes

Zur Erlangung des akademischen Grades eines
DOKTORS DER NATURWISSENSCHAFTEN

von der Fakultät für Physik der
Universität Karlsruhe (TH)
genehmigte

DISSERTATION

von

Dipl.-Geophys. Andreas Barth

aus Marburg/Lahn

Tag der mündlichen Prüfung:

9. Februar 2007

Referent:

Prof. Dr. Friedemann Wenzel

Korreferent:

Prof. Dr. Domenico Giardini

*“Ferne Kunde
bringt Dir der schwankende Fels-:
Deute die Zeichen !”*

Emil Wiechert, 1902



Contents

| | |
|---|------------|
| Zusammenfassung | vii |
| Abstract | xv |
| 1 Introduction | 1 |
| I Moment tensor inversion | 9 |
| 2 Theory of the seismic moment tensor | 11 |
| 2.1 Definition of the moment tensor | 11 |
| 2.2 Eigenvector representation of the moment tensor | 15 |
| 2.3 Inversion of the moment tensor | 20 |
| 3 Frequency sensitive moment tensor inversion | 23 |
| 3.1 Seismic data | 23 |
| 3.2 Frequency sensitive processing | 27 |
| 4 Moment tensor solutions | 33 |
| 4.1 Inversion results | 33 |
| 4.2 The 4 January 2000 M_W 4.8 earthquake | 35 |
| 5 Discussion | 41 |
| 5.1 Statistical overview | 41 |
| 5.2 Individual moment tensor solutions | 43 |

| | | |
|------------|---|------------|
| 5.3 | Potential and restrictions of the frequency sensitive moment tensor inversion | 49 |
| 5.4 | Singular value decomposition | 52 |
| 5.5 | Magnitude threshold for eastern Africa | 56 |
| II | Stress and strain | 59 |
| 6 | Theory of the stress tensor | 61 |
| 6.1 | Properties of the stress tensor | 61 |
| 6.2 | Formal stress inversion | 64 |
| 7 | Stress and strain calculation | 67 |
| 7.1 | Focal mechanism solutions of eastern Africa | 67 |
| 7.2 | Zonation of eastern Africa and stress inversion | 69 |
| 7.3 | Strain rates | 75 |
| 8 | Discussion of the eastern African stress field | 79 |
| III | Conclusions | 85 |
| 9 | Summary | 87 |
| | References | 89 |
| | List of Figures | 99 |
| | List of Tables | 101 |
| IV | Appendices | 103 |
| A | Tables of earthquake locations and moment tensor inversion results | 105 |
| B | Figures of moment tensor inversion results | 111 |
| C | Equivalent forces | 131 |

Zusammenfassung

Einleitung

Die tektonischen Spannungen der Erdkruste sind eine wichtige Informationsquelle, um das Auftreten von Erdbeben besser zu verstehen und Risiken abschätzen zu können. Um ein möglichst umfassendes Bild des weltweiten Spannungsfelds zu geben, stellt das „World Stress Map Project“ (*WSM*) eine globale Datenbank von horizontalen Spannungsorientierungen zur Verfügung.

Dazu werden Spannungen aus unterschiedlichen Basisdaten wie Bohrlochmessungen, geologischen Indikatoren und Erdbeben Bruchmechanismen abgeleitet und in ein Qualitätsschema eingeordnet, so dass die verschiedenen Daten vergleichbar sind. Der größte Teil stammt dabei aus Erdbeben Herdflächenlösungen (45%), die hauptsächlich durch die automatische „Centroid Moment Tensor“ (*CMT*) Inversion bestimmt werden. Da eine globale Herdflächenbestimmung durch die *CMT*-Methode nur für Erdbeben $M_W \geq 5,5$ gegeben ist (Dziewonski et al., 1987b) und sich seismische Aktivität an Kontinentalplattenrändern konzentriert, sind für Regionen mittlerer Seismizität im zentralen Bereich der Platten (Intraplattenseismizität) kaum Herdflächenlösungen bekannt.

Im Rahmen der *WSM* untersuche ich in dieser Arbeit das Potential der Herdflächenbestimmung schwacher bis mittelstarker Beben ($M_W \leq 5,5$) in Gebieten mittlerer Intraplattenseismizität am Beispiel des östlichen Afrikas. Ich verwende dazu die Methode der Momententensorinversion langperiodischer Raum- und Oberflächenwellen mit Perioden $T \geq 35$ s (Giardini, 1992). Ich zeige in dieser Arbeit, dass die Inversion teleseismischer Seismogramme mit Quell-Empfänger Entfernungen von bis zu 3300 km abhängig von dem invertierten Frequenzband ist. Um diesem Sachverhalt gerecht zu werden, habe ich eine frequenzabhängige Prozedur entwickelt, die zuerst einen geeigneten Datensatz von Wellenformen mit hohem Signal-Rauschen-Verhältnis und den optimalen Frequenzbereich bestimmt, um daraus den Momententensor und die Hypozentraltiefe des Bebens zu berechnen.

Datensatz

Für eine Momententensorinversion schwacher bis mittelstarker Erdbeben wird eine genügend große Menge von Seismometerdaten aus regionalen bis teleseismischen Entfernungen benötigt. Im östlichen Afrika und den angrenzenden Regionen stehen seit 1994 kontinuierlich aufgezeichnete langperiodische Daten von fünf Seismometern zur Verfügung. Seitdem hat sich Anzahl der Seismometer kontinuierlich erhöht, so dass seit 1999 bereits 13 permanente Seismometer die Seismizität registrieren. Zwischen 1994 und 2002 wurden 61 Beben, für die keine *CMT*-Lösung vorhanden ist, im Gebiet von 24°S bis 10°N und 20°E bis 51°E und mit Magnituden $m_b \geq 4,5$ und $M_S \geq 4,5$ aus dem Engdahl-Katalog (Engdahl et al., 1998) ausgewählt, um zu untersuchen, unter welchen Bedingungen für diese Beben eine Momententensorinversion möglich ist. Um störende lokale Effekte der Seismometer wie z.B. Bodenunruhe, atmosphärisch bedingtes Rauschen und den Einfluss heterogener Krustenstrukturen zu minimieren, habe ich in dieser Arbeit eine semi-automatische Prozedur zur Momententensorinversion entwickelt, die der Frequenzabhängigkeit dieser Effekte gerecht wird und das am wenigsten gestörte Frequenzband für eine Inversion bestimmt.

Frequenzabhängige Momententensorinversion

Die aufgezeichneten Seismogramme werden zuerst für die Instrumentenantwort des Seismometers korrigiert und dann derart rotiert, dass die beiden Horizontalkomponenten in Richtung des Rückazimuts (in Richtung des Erdbebens) bzw. orthogonal dazu orientiert sind (Radial- und Transversalkomponente R und T). Die Vertikalkomponente (Z) bleibt dabei unverändert. Die Inversion führe ich nach Giardini (1992) im Frequenzbereich durch und erlaube Laufzeitkorrekturen, um Krustenheterogenitäten auszugleichen, die von dem verwendeten eindimensionalen Standarderdmodell (PREM, Dziewonski and Anderson, 1981) nicht erklärt werden können. Diese Zeitkorrekturen beschränke ich auf ein Viertel der kleinsten invertierten Periode, die für die Z - und R -Komponente identisch sein müssen (P- und Rayleigh-Welle) und für die T -Komponente (S- und Love-Welle) unabhängig bestimmt werden.

Die Inversion wird nun mehrfach durchgeführt, um den Datensatz mit dem besten Signal-Rauschen-Verhältnis, den optimalen invertierten Frequenzbereich und die Tiefe des Erdbebenherds zu bestimmen. Dabei verwende ich eine semi-automatische dreistufige Prozedur:

- 1) Bestimmung des initialen Datensatzes N_{init} für ein initiales und repräsentatives Frequenzband F_{init} .
- 2) Auswahl des optimalen Datensatzes N_{final} in Abhängigkeit von Frequenzband und Hypozentraltiefe.
- 3) Frequenzabhängige Analyse des optimalen Datensatzes zur Bestimmung des optimalen Frequenzbands F_{final} und der Hypozentraltiefe.

Die wichtigsten Inversionsparameter zur Bestimmung des Datensatzes, des Frequenzbands und der Hypozentraltiefe sind die Varianzgrenzen, die festlegen, welche Wellenformen ein

ausreichend hohes Signal-Rauschen-Verhältnis haben und somit durch einen Momententensor und das PREM-Erdmodell erklärt werden können. Diese Grenzen habe ich empirisch derart bestimmt, so dass sowohl eine gute Datenanpassung garantiert ist, als auch eine möglichst große Datenmenge genutzt werden kann. Die minimal invertierbare Datenmenge habe ich auf sechs Seismometerkomponenten festgelegt, da für weniger Wellenforminformation kein generell stabiles Inversionsergebnis erfolgt.

Ergebnisse der Momententensorinversion

Die frequenzabhängige Auswertung der 61 ausgewählten Erdbeben resultiert in 38 Momententensoren. Für die übrigen Beben kann aufgrund einer zu geringen Datenmenge mit gutem Signal-Rauschen-Verhältnis (weniger als sechs Komponenten) keine stabile Inversion durchgeführt werden. Für die 38 Beben habe ich Momentenmagnituden zwischen M_W 4,4 und M_W 5,5 errechnet. Sie konzentrieren sich mehrheitlich entlang des ostafrikanischen Grabens, während ich 13 Ereignisse abseits der Hauptstörungen ausgewertet habe. Die Beben zeigen hauptsächlich Abschiebungsmechanismen, die für kontinentale Riftsysteme wie den ostafrikanischen Graben charakteristisch sind.

Die Anpassung der beobachteten Daten durch die synthetischen Wellenformen, die aus den Momententensoren berechnet werden, ist generell gut und zeigt kleine Datenvarianzen, die ähnlich zu Resultaten aus dem Mittelmeerraum mit geringeren Quell-Empfänger Entfernungen sind (Bernardi et al., 2004). Die gute Datenanpassung ist zurückzuführen auf die adäquate Wahl der Varianzgrenzen und die Beschränkung der Datenmenge auf sechs Komponenten, was ein stabiles Inversionsergebnis gewährleistet. Für die 38 berechneten Momententensoren steigt dabei die Varianz mit kleiner werdender Magnitude an, da für schwache Beben das Signal in teleseismischen Entfernungen ähnlich groß wie die Amplitude von lokalen Störsignalen werden kann.

Ein weiterer Kontrollparameter für eine stabile Inversion ist der Anteil eines einfachen Scherbruchs („double couple“, DC) am Momententensor. Da speziell für schwache Beben solch ein einfacher DC -Bruchmechanismus häufig angenommen wird, werden nicht- DC Anteile auf inkonsistente Daten zurückgeführt (Kuge and Lay, 1994). Um diesen Sachverhalt zu untersuchen, habe ich eine Eigenvektorzerlegung (SVD) durchgeführt, die zeigt, dass für die vorliegenden Momententensoren niedrige DC -Anteile zwar eine Konsequenz nicht erklärter Krustenheterogenitäten sein können, aber in den meisten Fällen der eigentliche Scherbruchmechanismus nicht verändert wird. So zeigt sich für die invertierten Mechanismen ein Trend von abnehmendem DC -Anteil für kleiner werdende Magnituden als eine Konsequenz vermehrter Störsignale, die zwar durch einen einfachen Scherbruch nicht erklärt werden können, aber bei der Inversion dennoch die Form des Scherbruchmechanismus' nicht entscheidend verändern.

Darüber hinaus existiert eine Abhängigkeit des automatisch bestimmten optimalen Frequenzbands zur Magnitude. Wie schon von anderen Autoren beschrieben, zeigen auch

meine Inversionsergebnisse die Notwendigkeit höhere Frequenzen zu invertieren, wenn für schwächere Erdbeben Momententensoren bestimmt werden sollen (Braunmiller et al., 2002; Šílený, 2004). Generell steigt die Anzahl der invertierten Seismometerkomponenten von 1994 bis 2002 an, da auch die Anzahl der permanent betriebenen Seismometer kontinuierlich erhöht wurde.

Individuelle Ergebnisse der Momententensorinversion

Um die frequenzabhängige Momententensorinversion zu testen, habe ich den Bruchmechanismus des M_W 6,4 Bebens vom 2. Oktober 2000 bestimmt, der auch von verschiedenen Agenturen (CMT, USGS) berechnet wurde. Dabei zeigt mein Ergebnis einen stabilen Abschiebungsmechanismus für einen breiten Frequenzbereich der den beiden anderen Herdflächenlösungen sehr ähnlich ist. Dieses Beben im südlichen Tanganyika See hat den verschiedenen Lösungen zufolge in einer Tiefe von 36–42 km stattgefunden. Diese ungewöhnliche Seismizität unterhalb der Oberkruste wurde schon mehreren Autoren beschrieben (z.B. Nyblade and Langston, 1995) und wird unterstützt von neun weiteren Erdbeben mit Hypozentraltiefen von 33 km und einem in 42 km Tiefe, die ich in dieser Arbeit bestimmt habe.

Während des Untersuchungszeitraums von 1994 bis 2002 haben sechs Erdbebenfolgen stattgefunden, für welche ich Herdmechanismen berechnet habe. Darin enthalten sind zwei Nachbeben des erwähnten Tanganyika Bebens. Zusätzlich habe ich noch für ein weiteres Nachbeben (24. Oktober 2002) eine Momententensorinversion durchgeführt, während die vier verbleibenden bearbeiteten Bebenserien keinen vorangegangenes Hauptbeben besitzen. Innerhalb dieser Erdbebenfolgen habe ich teilweise gemeinsame Nodalflächen gefunden, die ich somit als Bruchfläche identifizieren konnte.

Eine zusätzlich Besonderheit stellen drei von mir invertierte Herdmechanismen dar, welche gegen den allgemeinen Trend von Abschiebungen im östlichen Afrika Überschiebungsbeben zeigen. Alle drei liegen am Rand des Untersuchungsgebiets und sind möglicherweise ein Hinweis auf den Übergang von der Extension des ostafrikanischen Grabenbruchs zu Kompressionsgebieten in Richtung der mittelozeanischen Rücken (Coblentz and Sandiford, 1994).

Potential und Beschränkung der Methode

Um die Methode weltweit anwendbar zu machen, habe ich ein eindimensionales Standardmodell zur Berechnung der synthetischen Wellenformen gewählt (Dziwonski and Anderson, 1981). Dies beschränkt die verwendbaren seismischen Signale auf langwellige Anteile, die von kleinskaligen Heterogenitäten in der Erdkruste kaum beeinflusst werden (Larson and Ekström, 2001). Allerdings ist der Periodenbereich für meine Untersuchung

auch zu langen Perioden hin beschränkt, da für Erdbeben von Magnituden $M_W \leq 5,5$, die in Entfernungen bis zu 3300 km aufgezeichnet werden, die transienten Signale für lange Perioden in den Amplitudenbereich des seismischen Rauschens fallen. Dies beschränkt den Periodenbereich, den ich für diese Studie verwenden kann auf $\mathcal{T} = 35\text{--}100$ s.

Eine genaue Auflösung der Hypozentraltiefe mit einer Momententensorinversion ist für langperiodische Signale nur begrenzt möglich (Giardini, 1992). Daher habe ich sechs diskrete Krustentiefen ausgewählt, um die Tiefe des Bebenherds zu bestimmen. Einige Resultate haben nur ein sehr undeutliches Varianzminimum für die verschiedenen Herdtiefen und sind somit weniger verlässlich als die Mehrheit der Ergebnisse, die für eine diskrete Tiefe ein deutliches Varianzminimum aufweisen. Im Allgemeinen zeigt sich, dass die Beschränkung der Laufzeitkorrektur auf ein Viertel der kleinsten invertierten Periode und die Beschränkung der Datenmenge auf mindestens sechs Seismometerkomponenten stabile Herdflächenlösungen für schwache Erdbeben gewährleistet.

Eigenvektorzerlegung

Die Eigenvektorzerlegung (*SVD*) des Momententensors ermöglicht die Reduzierung des Einflusses inkonsistenter Signale durch das Entfernen des Eigenvektors höchster Ordnung (kleinster Eigenwert, Forbriger, 2001). Da besonders für die von mir untersuchten schwachen Erdbeben der Einfluss des seismischen Rauschens nicht vernachlässigt werden darf, habe ich für alle 38 Momententensoren die *SVD* zur Untersuchung der Auswirkungen inkonsistenter Datenanteile auf die Herdflächenlösung durchgeführt. Auffällig ist, dass sich bei denen um den Eigenvektor höchster Ordnung reduzierten Lösungen in der Hälfte der Fälle der *DC*-Anteil des Mechanismus nicht ändert und somit inkonsistente Datenanteile entfernt werden. Andererseits erfolgt keine generelle Erhöhung des *DC*-Prozentsatzes wie er für rein statistisch verteiltes Rauschen in den Daten zu erwarten wäre. Letztendlich zeigt die Eigenwertzerlegung besonders für Beben mit kleinem *DC*-Prozentsatz - was als instabiles Inversionsergebnis gedeutet werden kann (Kuge and Lay, 1994), dass hier das Reduzieren des Momententensors kaum zu Veränderungen des *DC*-Herdmechanismus führt und somit die Stabilität des Inversionsergebnisses zeigt.

Vollständigkeit der Herdflächenlösungen

Durch die frequenzabhängige Momententensorinversion kann ich Herdmechanismen von Erdbeben bis zu M_W 4,4 bestimmen und damit schwächere Beben auswerten, als es bisher durch die automatische *CMT*-Bestimmung möglich war ($M_W \geq 4,7$ im Untersuchungsgebiet). Eine Analyse der Häufigkeitsverteilung der Herdmechanismen in Abhängigkeit von der Magnitude zeigt, dass *CMT*-Lösungen bis etwa M_W 5,3 vollständig sind. Wie weit dieses Niveau mit dieser Arbeit abgesenkt wird, kann nur abgeschätzt werden, da der Untersuchungszeitraum von sieben Jahren keine vollständige Statistik zulässt. Ein Vergleich

mit der Verteilung der *CMT*-Lösungen der Jahre 1977–2002 zeigt jedoch eine deutlich verringerte Magnitudenschwelle für Beben meiner Arbeit, wonach ich das Vollständigkeitsniveau auf etwa M_W 5,0 senken kann.

Spannungsinversion

Um das Spannungsfeld im östlichen Afrika zu bestimmen, invertiere ich Gruppen von Momententensoren für einen gemeinsamen Spannungstensor, der die Verschiebungsrichtungen auf den Herdflächen am besten erklärt (Michael, 1987b). Neben den von mir berechneten Herdflächenlösungen verwende ich 90 *CMT*-Lösungen und 17 weitere aus verschiedenen Quellen. Ausgehend von der Zonierung des „Global Seismic Hazard Assessment Programs“ (*GSHAP*, Midzi et al., 1999) passe ich die Einteilung des Untersuchungsgebiets an, um in den einzelnen Zonen eine separate Spannungsinversion durchzuführen. Darüber hinaus untersuche ich weitere Einteilungen, um Zonen mit möglichst konsistenten Ergebnissen zu erhalten. Eine detaillierte Studie des westlichen Riftzweigs offenbart eine systematische, orthogonal zum Grabenverlauf ausgerichtete Extension.

Die endgültige Einteilung besteht aus zehn Zonen, die eine generelle Ost/West Extension zeigen. Bis auf die Zone östlich des Viktoria Sees weisen alle Inversionen eine eindeutige Richtung der minimalen Horizontalspannung S_h auf. Dabei zeigt sich eine S_h -Rotation von West-Nordwest/Ost-Südost im Nordwesten zu Ost-Nordost/West-Südwest im Südosten.

Deformationsraten

Zur Bestimmung der jährlichen Öffnungsrate des ostafrikanischen Grabens habe ich die Zonierung und Daten aus der Spannungsinversion übernommen. Bei den seismischen Daten beschränke ich mich auf die Jahre 1985–2005, da frühere, vereinzelt bestimmte Herdmechanismen kein vollständiges Abbild der Seismizität geben. Nach Kostrov (1974) summiere ich die Momententensoren für die einzelnen Riftsegmente und berechne daraus die jährlichen Öffnungsraten.

Im Vergleich mit *GPS*-Studien sind die Werte sehr klein, was hauptsächlich auf zwei Ursachen zurückzuführen ist. Zum einen ist der Beobachtungszeitraum im Vergleich zu einem seismischen Zyklus zu kurz und unterschätzt so das kumulative seismische Moment. Fügt man das M_W 7,0 Beben vom 22. Februar 2006 zur Berechnung hinzu, verdoppelt sich die gesamte Öffnungsrate für das östliche Afrika auf 0,46 mm/a (7–25% der Vergleichsstudien). Der Hauptgrund für die kleinen Öffnungsraten liegt vermutlich in aseismischen Deformationen, die seismisch nicht messbar sind und auf die ein Großteil der Dehnung in Extensionsgebieten zurückgeführt werden kann.

Diskussion des Spannungsfelds

Für die meisten Zonen liefert die Spannungsinversion stabile Resultate, die eine Rotation der minimalen horizontalen Spannung von Nordwesten nach Südosten anzeigen. Mein Ergebnis wird ergänzt durch Bohrlochdaten und geologischen Indikatoren der *WSM*, die mit den von mir bestimmten Spannungsrichtungen in teilweise guter Übereinstimmung stehen. Als Erklärung für die Spannungsrotation schlage ich die Existenz zweier Mikroplatten zwischen dem westlichen und östlichen Zweig des ostafrikanischen Grabens vor (Calais et al., 2006). Während das Spannungsfeld in erster Näherung eine Extension in Ost/West Richtung aufweist und durch die Wirkung der potentiellen Gravitationsenergie des afrikanischen Hochplateaus zustande kommt (Coblentz and Sandiford, 1994), führt eine gegenläufige Rotation der Mikroplatten (Calais et al., 2006) zu Änderungen des Spannungsfelds. Weiterhin interpretiere ich die Seismizität am östlichen Kontinentalrand als südliche Fortsetzung des östlichen Grabenzweigs und Reaktivierung der Davie-Ridge, die ursprünglich eine mesozoische Transformstörung darstellt. Ein Grund dafür könnten z.B. Konvektionsströme unterhalb der Lithosphäre sein.

Zusammenfassung

Ich habe in dieser Arbeit gezeigt, dass die frequenzabhängige Momententensorinversion ein großes Potential für die Herdflächenbestimmung schwacher bis mittelstarker Erdbeben bietet. Als Fallbeispiel habe ich für das östliche Afrika 38 Herdflächenlösungen mit M_W 4,4–5,5 von teleseismischen Daten aus bis zu 3300 km Entfernung berechnet.

Die Momententensorinversion langperiodischer Raum- und Oberflächenwellen unter Verwendung eines eindimensionalen Erdmodells und Perioden größer als 35 s weist eine Frequenzabhängigkeit für die Herdflächenbestimmung von schwachen und mittelstarken Beben auf. Zur Auswertung der Daten habe ich eine frequenzabhängige Prozedur entwickelt, die neben einem geeigneten Datensatz von Wellenformen mit hohem Signal-Rauschen-Verhältnis den optimalen Frequenzbereich bestimmt, bevor der Momententensor und die Hypozentraltiefe berechnet werden. Sowohl Datenvarianzen als auch *DC*-Anteile zeigen dabei die Verlässlichkeit der Inversionsergebnisse, so dass ich dadurch die Schwelle für Herdmechanismenbestimmung im östlichen Afrika auf $M_W \approx 5,0$ senken kann.

Die Spannungsinversion von 145 Herdmechanismen zeigt eine vorherrschende Ost/West Extension im östlichen Afrika. Darüber hinaus lässt sich eine Rotation der Spannungsorientierung erkennen, die mit der Existenz zweier Mikroplatten begründet wird.

Durch die Verwendung eines globalen Erdmodells ist die frequenzabhängige Momententensorinversion leicht auf andere Regionen weltweit übertragbar und kann dazu beitragen die globale Magnitudenschwelle für Herdflächenbestimmungen absenken.

Abstract

The East African Rift intersects the African continent from North to South for over 3000 km. For this region of intermediate seismicity only limited information about the tectonic stress regime is available. This is primarily due to a lack of earthquake source mechanism data, from which stress orientations can be deduced. Focal mechanisms for the limited number of strong earthquakes are calculated routinely by the Harvard *CMT*-group using moment tensor inversion of teleseismic data. However, earthquake magnitudes of the numerous smaller events are often below the *CMT*-threshold of $M_W \approx 5.3$ and thus, focal mechanism solutions are hardly available.

To study these earthquakes I developed a semi-automatic and frequency sensitive moment tensor inversion, that allows to calculate source mechanisms of light to moderate magnitude events $M_W \leq 5.5$. Used data are provided by 13 broadband and long-period permanent seismometers from the global seismic network with source-receiver distances up to 3300 km. The frequency sensitive procedure determines a waveform dataset and an optimum frequency pass-band for which stable moment tensor solutions are obtained. For the years 1995–2002 I present focal mechanism of 38 earthquakes within a magnitude range from M_W 4.4 to M_W 5.5, that were not studied previously. The calculated solutions show predominantly normal faulting mechanisms, that are mainly concentrated on the major rift branches. The inversions result in generally low data variances and reliable moment tensor solutions for frequency pass-bands between 10 mHz and 29 mHz (periods 35–100 s). A study of the double couple (*DC*) parts reveals a small number of low *DC*-percentages, that can be increased by cutting off the highest order eigenvector with a singular value decomposition (*SVD*).

An estimation of the seismic deformation for eastern Africa is difficult, since a complete set of focal mechanisms (this study and *CMT*-solutions) is only available for a time period shorter than one seismic cycle. However, the average opening rate calculated from 1985–2005 and including the major M_W 7.0 event from 2006-02-22 is 0.46 mm/a for the East African Rift System. Nevertheless, this value is only 7–25% of the *GPS*-measurements, probably as a consequence of aseismic deformation.

For a formal stress inversion I combine the 38 newly calculated focal mechanisms with others determined by moment tensor inversion: 90 mechanisms are taken from the *CMT*-catalogue (1977–2005) and 17 additional mechanisms of strong events are given by other

authors between 1964 and 1977. I perform a stress inversion for ten separate areas, that are adopted from the Global Seismic Hazard Assessment Program (*GSHAP*) and adapted to the event distribution used in this study. A special zonation is applied along the western branch of the East African Rift System, that shows minimum horizontal stress approximately perpendicular to the rift valley orientation and thus the trend of the main fault. All over eastern Africa I obtain stable stress tensors, that show a general east/west extension. From northwest to southeast a smooth counter-clockwise rotation from west-northwest/east-southeast to east-northeast/west-southwest extension is visible.

The supposed stress rotation is partly supported by three averaged stress orientations of the World Stress Map (*WSM*) database in the northeastern part of the study region. While the first-order pattern of east/west extension in eastern Africa can be explained by the effect of gravitational potential energy differences, a possible reason for the stress change is probably related to the existence of two microplates. Both of them are located between the eastern and western rift branch and are supposed to rotate versus each other, involving a change of stress orientation along their boundaries. For the eastern continental margin I calculate an extensional stress regime, that could be evidence of the re-activation of the Davie-Ridge as a spreading centre possibly due to sublithospheric mantle flow.

I presented a frequency sensitive moment tensor inversion, that considers the dependency of the focal mechanisms on the inverted frequency pass-band. Since I use a one-dimensional earth model and waveform data of the permanent global seismometer network, the method is easily transferable to other regions worldwide and thus can improve the understanding of regional tectonics.

Chapter 1

Introduction

The World Stress Map Project (*WSM*) is a compilation of stress orientations of different indicators on different scales. Stress information is deduced from earthquake focal mechanisms, well bore breakouts, drilling-induced fractures, in-situ measurements (hydraulic fracturing, overcoring data and borehole slotter), strain relief measurements and young geological data (Heidbach et al., 2004). The aim of the *WSM* is to provide standardised and quality-ranked stress data on a world wide scale and to combine different data resources on a user-friendly and online available database.

The major part of *WSM* stress data, however, is deduced from earthquake focal mechanism data (Zoback, 1992a), mainly provided by the routinely determined Harvard centroid moment tensor (*CMT*) solutions (Dziewonski et al., 1987a) and moment tensors by other institutions. Excluding the so-called “possible plate boundary event”-focal mechanisms, that rather reflect the kinematic behaviour of an existing fault-zone than the intraplate stress field, the quota of *WSM* stress orientations deduced from focal mechanisms is 45% (Heidbach et al., 2005). Nevertheless, the distribution of stress information obviously reflects the global seismicity pattern (Fig. 1.1), since the global earthquake distribution is strongly connected to the plate boundaries. However, focal mechanism determination is restricted by the regional seismometer coverage. So for regions with only sparse seismometer distribution, focal mechanisms are determined only for higher earthquake magnitudes. Figure 1.2a shows the magnitude statistics of *CMT*-solutions determined per year since 1976. Below $M_W = 5.0$ – 5.5 the number of evaluated seismic events decreases significantly. Since earthquake magnitude statistics follow the logarithmic Gutenberg-Richter relation, the number of events $M_W \geq 4.5$ per year for which no moment tensor solution is calculated is greater than 2000. Thus the determination of low magnitude earthquake focal mechanisms for intraplate regions of moderate seismicity holds a high potential of new intraplate stress information that can give important insights into active tectonics (Fan and Wallace, 1991; Brazier et al., 2005) and detailed informations in terms of seismic hazard assessment.

Source-relevant teleseismic recordings with a high signal-to-noise ratio of light to moderate events ($M_W = 4.0$ – 5.9 , magnitude classes see Figure 1.2) are available only for intermediate-

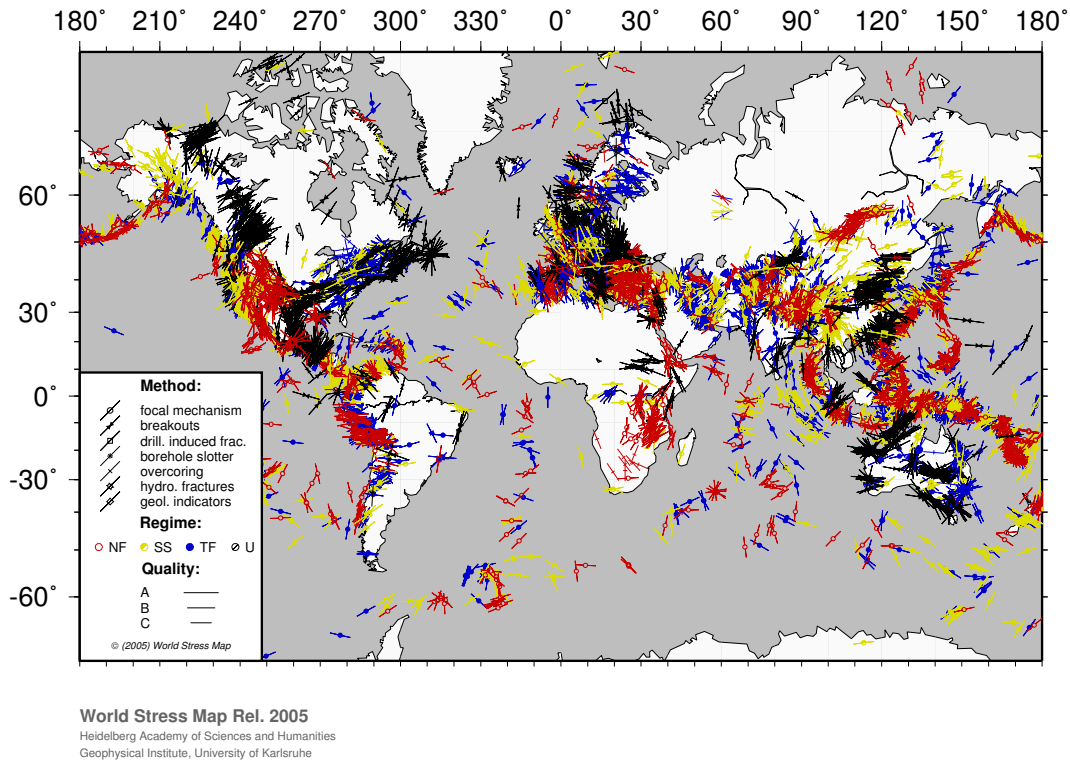


Figure 1.1: World Stress Map release 2005 (Reinecker et al., 2005). Shown are maximum horizontal stress orientations for qualities A, B, C. Symbols indicate type of stress measurement, colours correspond to tectonic regimes for stress indicators deduced from focal mechanism solutions. Red indicates normal, yellow strike-slip and blue thrust faulting regimes.

period surface waves ($40 \text{ s} \leq \mathcal{T} < 150 \text{ s}$, Arvidsson and Ekström, 1998). Reliable data of these waves are obtained only in a limited frequency band, that is restricted by seismic noise at the station-site (e.g. Stutzmann et al., 2000), the intrinsic attenuation of the wave-energy (e.g. Anderson and Hart, 1978) and heterogeneities in the surface wave phase velocity pattern (Arvidsson and Ekström, 1998). Dependent on the earthquake magnitude and source-receiver distances the inverted frequency band of waveform data has to be chosen adequately (Braunmiller et al., 2002).

Harvard *CMT*-solutions are calculated automatically inverting long-period body and surface waves using periods of $\mathcal{T} > 45 \text{ s}$ respective $\mathcal{T} > 135 \text{ s}$ recorded by different sets of permanent stations of the global seismic network in teleseismic distances (Dziewonski et al., 1987b, compare Table A.2 Σ_b and Σ_m). On a global scale the level of completeness for *CMT*-solutions is approximately $M_W \approx 5.5$ and slightly lower for regions with a dense seismometer coverage (Arvidsson and Ekström, 1998). To lower this magnitude threshold, regional station networks have been used to calculate source mechanisms by moment tensor inversion for $M_W < 5.0$ (e.g. Pinar et al., 2003; Stich et al., 2003). Commonly, these

studies inverted waveform data with periods ranging from 10 s to 50 s recorded at distances up to 1000 km. [Stich et al. \(2003\)](#) used waveform data of light to moderate magnitude earthquakes in Spain recorded in local to regional distances up to 1000 km. They inverted periods from 20 s to 50 s and 15 s to 35 s for events with $M_W \geq 4.0$ and $M_W < 4.0$, respectively.

In this work I present a frequency sensitive moment tensor inversion that allows to determine low magnitude earthquake focal mechanisms using data from regional and teleseismic seismometers. For each event the procedure automatically selects high quality waveform data and adjusts the frequency band to the individual setting, i. e. source-receiver locations and the earthquake magnitude. Intraplate regions where only sparse stress information is available but intermediate seismicity is present are for example eastern Africa, inner Asia including the Baikal region, western Australia and eastern South-America (Fig. 1.2b). As a case study I analyse dependencies of the moment tensor inversion on hypocentral depth and frequency pass-band for light to moderate magnitude earthquakes ($4.5 \leq M_W < 5.0$) in eastern Africa using the permanent seismometer network with source-receiver distances of up to 3300 km.

The so-called East African Rift System (*EARS*) is a rare example of active continental rifting. Passing for nearly 3000 km through the continent, the *EARS* separates the Nubian subplate to the west from the Somalian subplate to the east (Fig. 1.3). Beginning on the Afar triple junction, it crosses the Ethiopian highland and leads to the eastern rift branch dispersing in northern Tanzania. [Grimison and Chen \(1988\)](#), however, proposed an extended eastern branch that connects to the Davie Ridge along the continental margin on the coast of eastern Africa, to explain the seismic activity in the northern Mozambique Channel. The Aswa fault-zone north of Lake Victoria is a northwest-southeast striking left-lateral fault system that connects the eastern branch with the northernmost part of the western branch. The western branch starts in southern Sudan and runs through the rift valley lakes—including Lake Tanganyika and Lake Malawi—to Mozambique. The characteristics of the southern end of the *EARS* are highly discussed. [Chu and Gordon \(1999\)](#) used seafloor spreading rates to determine the Euler pole of rotation between Nubian and Somalian subplate in the southern Mozambique Channel. Hence, the tectonic regime changes from extensional north of the pole to compressional south of it. However, there is no agreement where the system connects to the Southwest Indian ridge ([Horner-Johnson et al., 2005](#); [Lemaux et al., 2002](#)). To determine earthquake source mechanisms this work focuses on eastern African events that are located on the eastern and western branch of the rift system (excluding the Afar depression and the Main Ethiopian Rift), the seismic active region west of it, the Mozambique channel and Madagascar (Fig. 1.4).

Source mechanisms in eastern Africa were examined by several studies using both first motion analysis (e.g. [Fairhead and Girdler, 1971](#)) and waveform inversion. [Shudofsky \(1985\)](#) used Rayleigh-waveform inversion to calculate source mechanisms for earthquakes with magnitudes $M_W \geq 5.0$ from the years 1964 to 1977. He obtained 23 focal mechanisms all over Africa including 18 events located in the study region of this work and thus demonstrated the viability of this technique in a region of moderate seismicity and sparse data.

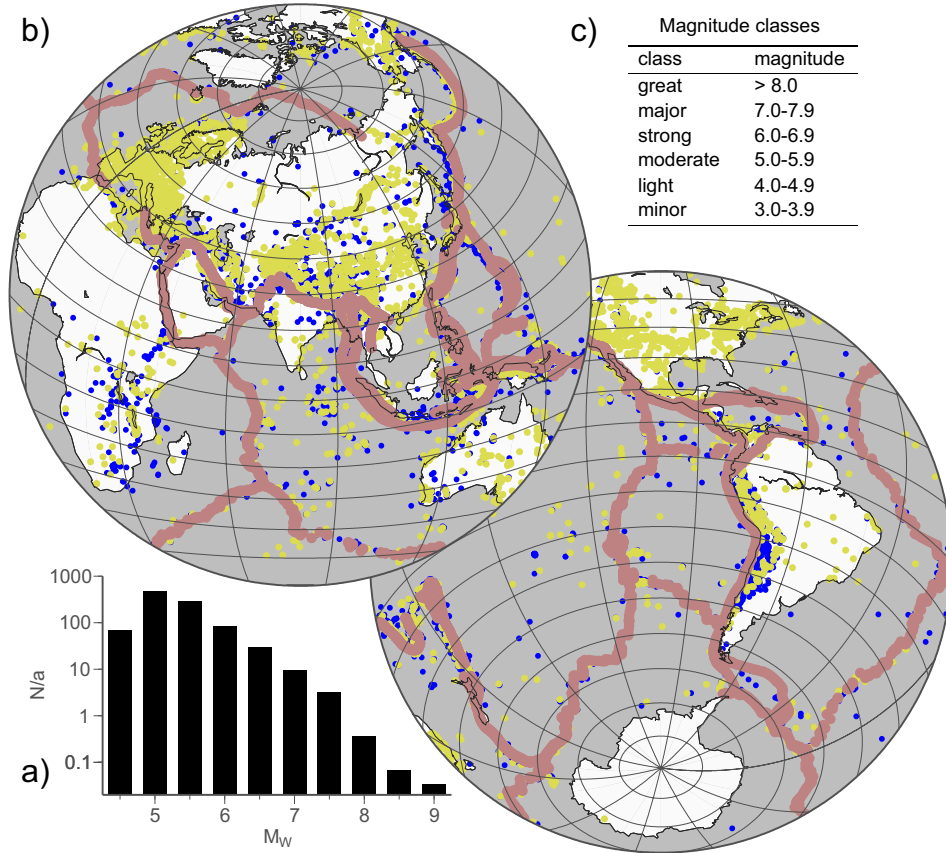


Figure 1.2: a) Number of *CMT*-solutions per year versus moment magnitude M_W since 1976. b) Global seismicity $M_W \geq 4.5$ (blue dots, Engdahl et al., 1998) since 1996, overlaid by plate-boundaries after Bird (2003) (red dots, diameter approx. 300 km) and *WSM*-data locations (yellow dots). Accumulation of blue symbols indicate intraplate regions of intermediate seismicity where only sparse stress information available. c) Magnitude classes (*USGS*).

Since 1977 - the beginning of routine determination of the Harvard *CMT*'s (Dziewonski et al., 1987b) - 90 focal mechanisms were given in the study region until end 2005 [*CMT* catalog, available online]. The level of completeness for *CMT*-solutions is approximately $M_W \approx 5.5$ (Arvidsson and Ekström, 1998), whereas for eastern Africa the level of completeness is $M_W \approx 5.1$, including events as low as $M_W = 4.7$. Thus for strong and most of moderate magnitude events the *CMT*-solution is given. Foster and Jackson (1998) performed a P- and SH-waveform inversion to calculate 38 source mechanisms from 1966 to 1997 with magnitudes $M_W \geq 5.1$. 24 events were located in eastern Africa, including five mechanisms before 1977 that were not determined by *CMT*-solutions. To examine focal mechanisms of three small to minor magnitude events on the western branch ($M_W = 2.0-3.3$), Ferdinand and Arvidsson (2002) used data of a mobile station network to perform a body waveform

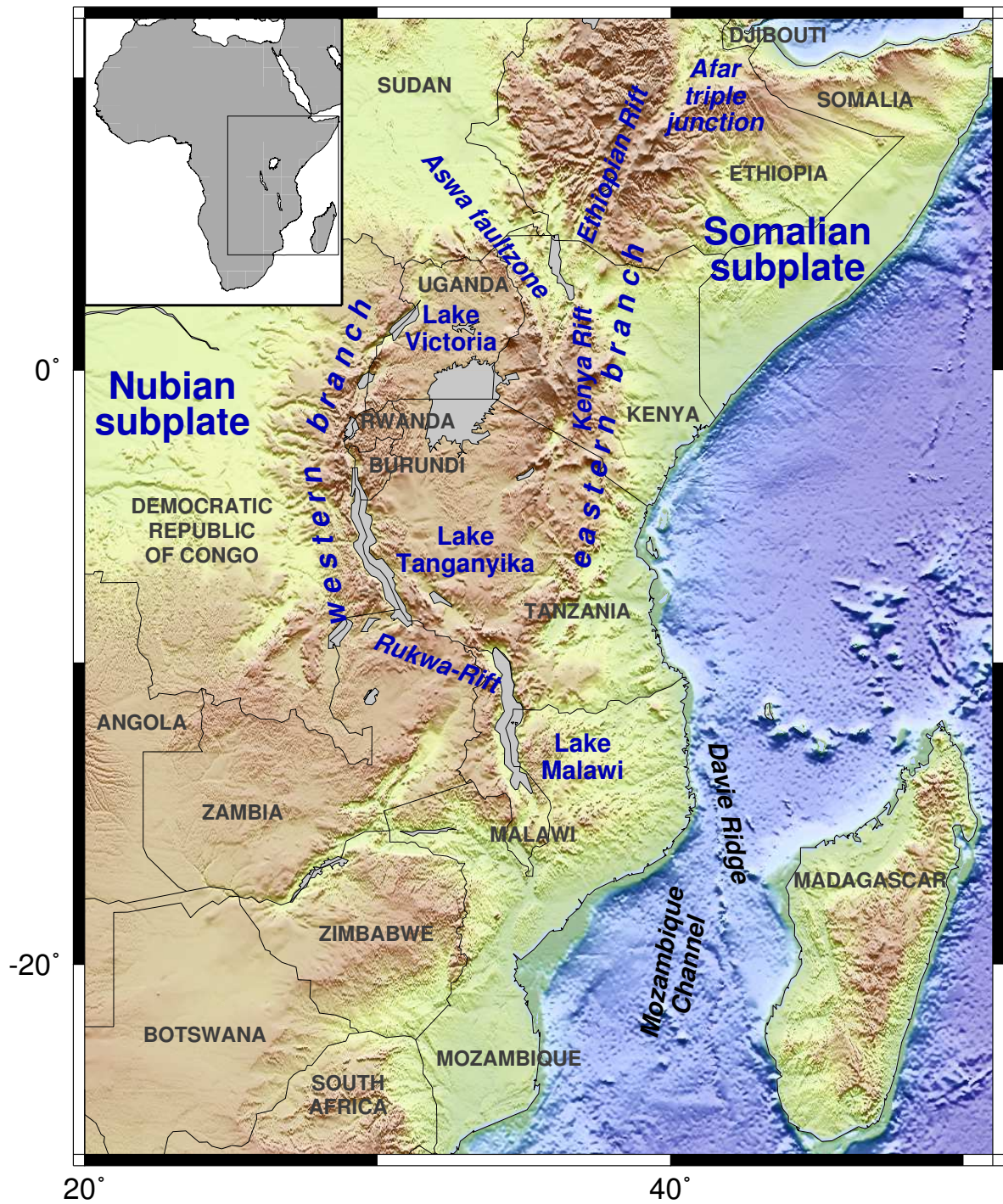


Figure 1.3: Topographic map of eastern Africa, including the eastern and western branch of the East African Rift System (*EARS*) that separates the Nubian and Somalian subplate. Details see text.

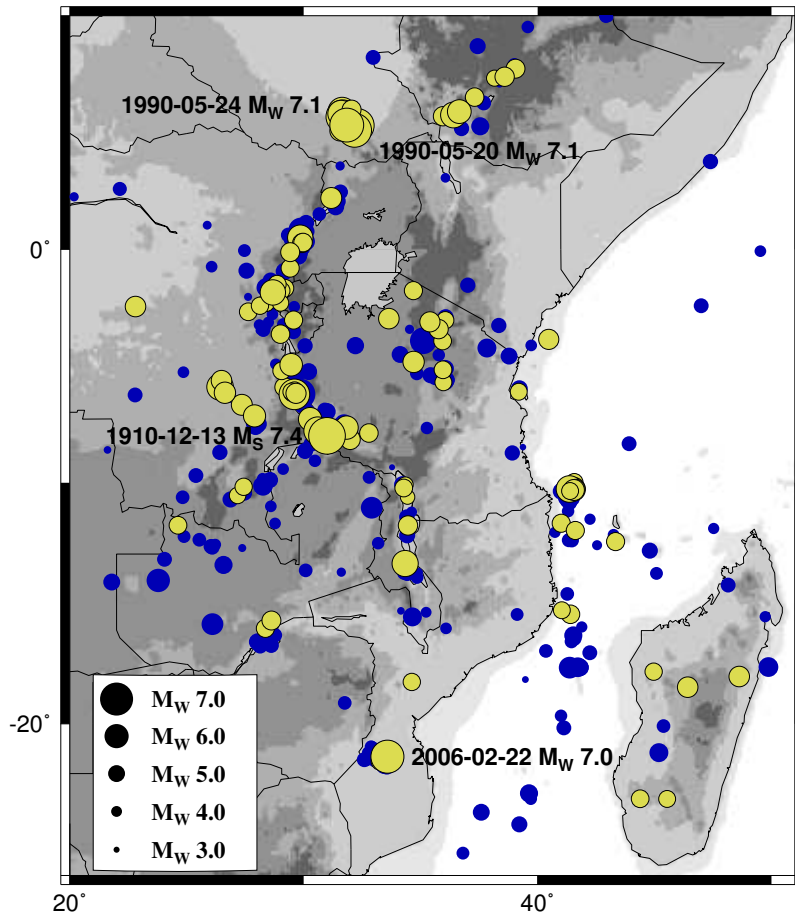


Figure 1.4: Seismicity of eastern Africa (Engdahl catalogue, Engdahl et al., 1998, 1964–2004 and *ISC*-catalogue 2005–2006). Symbol size is scaled by moment magnitude M_W . Events for which *CMT*-solutions are determined are coloured yellow. The four largest earthquakes with $M_W \geq 7.0$ are labeled by their date of occurrence.

inversion. Beside the latter for no other seismic event focal mechanisms were analysed in eastern Africa by waveform inversion than these also determined by *CMT*-solutions since 1977.

Therefore focal mechanism determination in eastern Africa using data from the permanent seismometer network is restricted to earthquakes $M_W \geq 5.0$. Since eastern African seismicity is mainly focused on the *EARS*, especially higher magnitude events seldom occur beside the rift structures. Thus also focal mechanism information concentrates on the rift itself, whereas lower magnitude events with unknown source mechanisms tend to spread on regions neighbouring the rift. Figure 1.4 displays the eastern African seismicity since 1964. Four major events with magnitudes greater than $M_W = 7.0$ occurred in eastern Africa within the last 100 years. The strongest event took place on the Rukwa-Rift in southern Tanzania on 13 December 1910 and had a magnitude of $M_S = 7.4$ (Ambraseys and Adams,

1992) (correlates with $M_W \approx 7.4 \pm .1$ (Atkinson and Boore, 1998)). In May 1990 an earthquake sequence occurred in the southern Sudan on the Aswa fault-zone (Gaulon et al., 1992). The main-shock on 20 May was determined by Harvard *CMT*-solution to $M_W = 7.1$ and the largest aftershock on 24 May likewise to $M_W = 7.1$. Recently a $M_W = 7.0$ event struck the southernmost part of the western rift branch in Mozambique on 22 February 2006.

Focal mechanisms of strong and moderate magnitude events ($5.0 \leq M_W < 7.0$) in eastern Africa are mostly determined by Harvard *CMT*-solutions. In this study I will determine new focal mechanism solutions for earthquakes $M_W \leq 5.0$ by frequency sensitive moment tensor inversion and analyse the applicability of the developed procedure. Finally, I will combine the new mechanisms with *CMT*-solutions and other datasets to perform stress inversions for separate regions and discuss the results in terms of eastern African tectonics.

Part I

Moment tensor inversion

Chapter 2

Theory of the seismic moment tensor

2.1 Definition of the moment tensor

Consider a continuous, elastic and spherical earth. To describe the processes and consequences of an earthquake occurring, the physical laws have to be evaluated in terms of internal deformations. The four conservation laws are: conservation of mass, momentum, angular momentum and energy. Adding Newton's law of gravitational attraction, the initial equilibrium state of the earth can be described. When an earthquake occurs, the displacement $\mathbf{s}(\mathbf{x}, t)$ at a location \mathbf{x} is perturbed from its equilibrium position at time t within a medium of density ρ_0 . The following discussion of relevant forces and conditions after [Dahlen and Tromp \(1998\)](#) finally leads to the introduction of the seismic moment tensor \mathbf{M} and the necessary assumptions for a point-source approximation.

The linearised form of the Eulerian momentum equation, including the conservation laws, is valid for small perturbations of the equilibrium state of the earth (with initial density ρ_0 and gravitational potential ϕ_0):

$$\rho_0 \partial_t^2 \mathbf{s} = \underbrace{\nabla \cdot \boldsymbol{\sigma} - \rho_0 (\nabla \phi + \mathbf{s} \nabla^2 (\phi_0 + \psi) + 2\boldsymbol{\Omega} \times \partial_t \mathbf{s})}_{\mathbf{L}(\mathbf{s})}. \quad (2.1)$$

The left hand side is the force density of accelerated mass. The four terms on the right hand side correspond to: 1) the force density of stress perturbation $\boldsymbol{\sigma}$, 2) the gravitational force density expressed as the gradient of the gravitational potential perturbation ϕ , 3) the force density resulting from the initial gravitational potential ϕ_0 and the centrifugal potential ψ and 4) the Coriolis force caused by the earth's rotation with uniform angular velocity $\boldsymbol{\Omega}$.

Assuming an infinitesimal and oriented surface element dS with the normal unit vector $\hat{\mathbf{n}}$, the stress tensor $\boldsymbol{\sigma}$ is defined by an infinitesimal and instantaneous surface force $d\mathbf{F}$ acting on the deformed area of the surface element (so-called Cauchy stress in contrast to the

Piola-Kirchhoff stress that is force per undeformed area):

$$d\mathbf{F} = \hat{\mathbf{n}} \cdot \boldsymbol{\sigma} dS. \quad (2.2)$$

Hence, the second order stress tensor $\boldsymbol{\sigma}$ is defined at a point within an arbitrary continuous medium. The traction vector \mathbf{t} however, is stress acting on a plane and can be defined by Cauchy's formula:

$$\mathbf{t} = \hat{\mathbf{n}} \cdot \boldsymbol{\sigma}. \quad (2.3)$$

To guarantee continuity across the internal interfaces of the earth, following boundary conditions have to be valid: Between interfaces of two solid materials the displacement vector \mathbf{s} must be continuous, i.e. no slip is allowed. On a fluid-solid boundary however, tangential slip is allowed, since an ideal fluid cannot support shear stress. Generally at all boundaries, the gravitational potential ϕ as well as tractions \mathbf{t} have to be continuous and thus a free surface condition with no tractions must be valid at the earth's surface:

$$\mathbf{t} = \hat{\mathbf{n}} \cdot \boldsymbol{\sigma} = \mathbf{0}. \quad (2.4)$$

Since the average frequency of the earth's rotation is $\bar{\Omega} = (\text{sidereal day})^{-1} = 11.6 \mu\text{Hz}$, the ratio between displacements due to accelerated mass and Coriolis force in equation 2.1, regarding frequencies greater than 10 mHz as done in this work, is less than 0.1%. Only if very long periods of normal modes are studied, these terms are not negligible. Beside this, also the centrifugal acceleration is small for the studied frequencies, so the centrifugal potential ψ can be neglected as well and $\mathbf{L}(\mathbf{s})$ reduces to:

$$\mathbf{L}(\mathbf{s}) = \nabla \cdot \boldsymbol{\sigma} - \rho_0 (\nabla \phi + \mathbf{s} \nabla^2 \phi_0) \quad (2.5)$$

and the linearised homogeneous equation of motion can be written as:

$$\rho_0 \partial_t^2 \mathbf{s} - \mathbf{L}(\mathbf{s}) = \mathbf{0}. \quad (2.6)$$

Beside the trivial solution $\mathbf{s} = \mathbf{0}$ —a silent earth in its state of equilibrium—equation 2.6 can be solved by solutions of the form:

$$\mathbf{s}(\mathbf{x}, t) = \sum_k \mathbf{s}_k(\mathbf{x}) e^{i\omega_k t}, \quad (2.7)$$

with the eigenfunctions $\mathbf{s}_k(\mathbf{x})$ and eigenfrequencies ω_k of the normal modes k of the earth, that satisfy:

$$\mathbf{L}(\mathbf{s}_k) + \rho_0 \omega_k^2 \mathbf{s}_k = \mathbf{0}. \quad (2.8)$$

Hence, seismic waves can be described by the summation of normal modes, which are the free oscillations of the earth. A detailed description of the eigenfunctions $\mathbf{s}_k(\mathbf{x})$, which are expressed by spherical harmonics, is given in [Dahlen and Tromp \(1998\)](#). However, when an earthquake occurs and the earth is ruptured, obviously this solution is not valid any longer.

The introduction of an additional internal body force density \mathbf{f} leads to the inhomogeneous equation of motion:

$$\rho_0 \partial_t^2 \mathbf{s} - \mathbf{L}(\mathbf{s}) = \mathbf{f}. \quad (2.9)$$

An earthquake is an anelastic process resulting in coseismic slip \mathbf{s} and a corresponding strain tensor $\boldsymbol{\epsilon}$:

$$\epsilon_{ij} = \frac{1}{2} (\partial_i s_j + \partial_j s_i). \quad (2.10)$$

Thus, the failure of material implies the failure of Hook's law, which is the linear elastic relation between stress $\boldsymbol{\sigma}$ and strain $\boldsymbol{\epsilon}$. The hypothetical stress modelled by Hook's law using the large anelastic strain within the source volume is:

$$\sigma_{ij} = C_{ijpq} \epsilon_{pq} \quad (2.11)$$

and results in a much larger stress than supposed to be present because of the surrounding stress field. Thus, the stress glut $\boldsymbol{\Gamma}$ is defined by the difference between the physical stress $\boldsymbol{\sigma}_{true}$ within the source region and the modelled stress $\boldsymbol{\sigma}_{model}$ that is calculated if Hook's law would be valid:

$$\boldsymbol{\Gamma} = \boldsymbol{\sigma}_{model} - \boldsymbol{\sigma}_{true}. \quad (2.12)$$

It will be shown in section 6.1 that the symmetry of the stress tensor—and thus the symmetry of the stress glut tensor $\boldsymbol{\Gamma}$ —follows from the conservation of angular momentum. The internal forces of the rupture process can be represented by the equivalent force densities \mathbf{f} and \mathbf{t} :

$$\mathbf{f} = -\nabla \cdot \boldsymbol{\Gamma}, \quad \mathbf{t} = \hat{\mathbf{n}} \cdot \boldsymbol{\Gamma}. \quad (2.13)$$

Since the equivalent force densities represent no external forces, neither a net force nor a net torque is exerted upon the earth (the explicit derivation is given in Appendix C).

Using the definitions of stress glut and equivalent forces, a solution of the inhomogeneous equation of motion (eqn. 2.9) will be given. Because of the completeness of the complex eigenfunctions $\mathbf{s}_k(\mathbf{x})$ and their conjugate complex $\mathbf{s}_k^*(\mathbf{x})$, the solution of equation 2.9 can be expressed as (considering implicitly the real part of the displacement $\mathbf{s}(\mathbf{x}, t)$):

$$\mathbf{s}(\mathbf{x}, t) = \sum_k a_k(t) \mathbf{s}_k(\mathbf{x}). \quad (2.14)$$

With the initial conditions, that no motion occurs within the earth volume V_E and on the earth's surface S_E before the earthquake occurs:

$$\begin{aligned} \mathbf{s}(\mathbf{x}, t) &= 0 \\ \partial_t \mathbf{s}(\mathbf{x}, t) &= 0, \quad \text{for } t \leq 0, \end{aligned} \quad (2.15)$$

equation 2.14 is (Dahlen and Tromp, 1998):

$$\begin{aligned} \mathbf{s}(\mathbf{x}, t) &= \sum_k \omega_k^{-2} \mathbf{s}_k(\mathbf{x}) \int_{-\infty}^t \partial_{t'} C_k(t') \left(1 - e^{i\omega_k(t-t')}\right) dt' \\ &= \sum_k (i\omega_k)^{-1} \mathbf{s}_k(\mathbf{x}) \int_{-\infty}^t C_k(t') e^{i\omega_k(t-t')} dt', \end{aligned} \quad (2.16)$$

with

$$\begin{aligned}
 C_k(t) &= \int_{V_E} \mathbf{f}(\mathbf{x}, t) \cdot \mathbf{s}_k^*(\mathbf{x}) dV + \int_{S_E} \mathbf{t}(\mathbf{x}, t) \cdot \mathbf{s}_k^*(\mathbf{x}) dS \\
 &= \int_{V_F} -[\nabla \cdot \mathbf{\Gamma}(\mathbf{x}, t)] \cdot \mathbf{s}_k^*(\mathbf{x}) + \nabla \cdot [\mathbf{\Gamma}(\mathbf{x}, t) \cdot \mathbf{s}_k^*(\mathbf{x})] dV \\
 &= \int_{V_F} \text{tr} [\mathbf{\Gamma}(\mathbf{x}, t) \cdot (\nabla \mathbf{s}_k^*)^T(\mathbf{x})] dV \\
 &= \int_{V_F} \text{tr} [\mathbf{\Gamma}(\mathbf{x}, t) \cdot \boldsymbol{\epsilon}_k^{*T}(\mathbf{x})] dV
 \end{aligned} \tag{2.17}$$

by inserting equation 2.13 and the conjugate complex strain tensor $\boldsymbol{\epsilon}_k^*(\mathbf{x})$ of mode k . According to the solution of the equation of motion for displacement \mathbf{s} (eqs. 2.16 and 2.17), [Dahlen and Tromp \(1998\)](#) showed that the acceleration field \mathbf{a} for times t later then the source duration t_f becomes:

$$\mathbf{a}(\mathbf{x}, t) = \sum_k c_k e^{i\omega_k t} \mathbf{s}_k(\mathbf{x}, t), \quad t \geq t_f, \tag{2.18}$$

where the complex excitation amplitude of the earth's free oscillations are:

$$c_k = \int_{t_0}^{t_f} \int_{V_F} \text{tr} [\partial_t \mathbf{\Gamma}(\mathbf{x}, t) \cdot \boldsymbol{\epsilon}_k^{*T}(\mathbf{x})] e^{-i\omega_k t} dV dt. \tag{2.19}$$

Now the seismic moment tensor \mathbf{M} is defined as:

$$\begin{aligned}
 \mathbf{M} &= \int_{t_0}^{t_f} \int_{V_F} \partial_t \mathbf{\Gamma}(\mathbf{x}, t) dV dt \\
 &= \begin{pmatrix} M_{11} & M_{12} & M_{13} \\ M_{21} & M_{22} & M_{23} \\ M_{31} & M_{32} & M_{33} \end{pmatrix}.
 \end{aligned} \tag{2.20}$$

Because of the symmetry of the stress glut $\mathbf{\Gamma}$ (see eqn. 2.12), the seismic moment tensor is an symmetric tensor of second order and describes the moment released by an earthquake and is given in Nm or dyn-cm. The scalar seismic moment is:

$$M_0 = \sqrt{\frac{\sum M_{ij}^2}{2}}, \tag{2.21}$$

and the moment magnitude M_W is defined as ([Hanks and Kanamori, 1979](#)):

$$M_W = \frac{2}{3} \log M_0 - 10.73, \quad M_0 \text{ in dyn}\cdot\text{cm}. \tag{2.22}$$

An approximation often used in seismology when the distance to a seismic source is large, is the assumption of a point-source that radiates the seismic energy. Since in that case

the excitation amplitudes are independent on the source dimension and source duration, they can be computed once and reused for the analysis of different sources, that is a major simplification for automatised moment tensor inversion (Giardini et al., 1993, see section 2.3). Working with long-period waveforms (period $\mathcal{T} \geq 35$ s), it can be assumed that the modes being excited are much longer than the source dimensions and the periods much longer than the source duration (point-source approximation). Hence the first part of a Taylor series of equation 2.19 around the fiducial origin time t_s and fiducial hypocentre \mathbf{x}_s is:

$$c_k = \text{tr} [\mathbf{M} \cdot \boldsymbol{\epsilon}_k^{*T}(\mathbf{x}_s)] e^{-i\omega_k t_s}. \quad (2.23)$$

Considering the next term of the Taylor expansion results in a more complex estimation of c_k including the first spatial and temporal moments which are used for defining the centroid time and location (Backus, 1977) of the maximum energy concentration during the source process. That kind of approach is used within the centroid moment tensor (CMT) inversion routine (Dziewonski et al., 1987a), while in this work an inversion for centroid time and location is not performed. However, individual time-shifts for the different traces are allowed to take account of inadequate estimations of time and source location (Giardini, 1992, section 3.2).

Corresponding to equation 2.23, expansion of equation 2.17 around t_s and \mathbf{x}_s including the seismic moment tensor \mathbf{M} (eqn. 2.20) allows to calculate seismic displacements for long periods (Dahlen and Tromp, 1998):

$$\mathbf{s}(\mathbf{x}, t) = \sum_k \text{tr} [\mathbf{M} \cdot \boldsymbol{\epsilon}_k^{*T}(\mathbf{x}_s)] \omega_k^{-2} \mathbf{s}_k(\mathbf{x}) (1 - e^{i\omega_k(t-t_s)}). \quad (2.24)$$

Equation 2.20 can be simplified by replacing the time dependent stress glut and source volume by constant values for times $t \geq t_f$. Thus inserting the static stress glut $\boldsymbol{\Gamma}_f$ and the final source volume V_f gives:

$$\mathbf{M} = \int_{V_f} \boldsymbol{\Gamma}_f dV; \quad \boldsymbol{\Gamma}_f = \int_{t_0}^{t_f} \partial_t \boldsymbol{\Gamma}(\mathbf{x}, t) dt. \quad (2.25)$$

For the limit of a zero source volume the stress glut equals the moment tensor per volume. Hence, in case of an isotropic physical stress $\boldsymbol{\sigma}_{true}$ (eqn. 2.12) within the source volume, the principle axes of moment tensor \mathbf{M} and modelled stress tensor $\boldsymbol{\sigma}_{model}$ would be identical. Since the moment tensor is defined as a stress difference integrated over the source volume, it is indirectly linked to the stress field outside the source. It will be shown in sections 6.2 and 7.3, that stress as well as strain can be derived under certain assumptions from the moment tensor (Gephart and Forsyth, 1984; Kostrov, 1974).

2.2 Eigenvector representation of the moment tensor

The nine elements of the seismic moment tensor represent the nine couples of equivalent body forces (Fig. 2.1). The off-diagonal elements are assigned to opposite forces that are

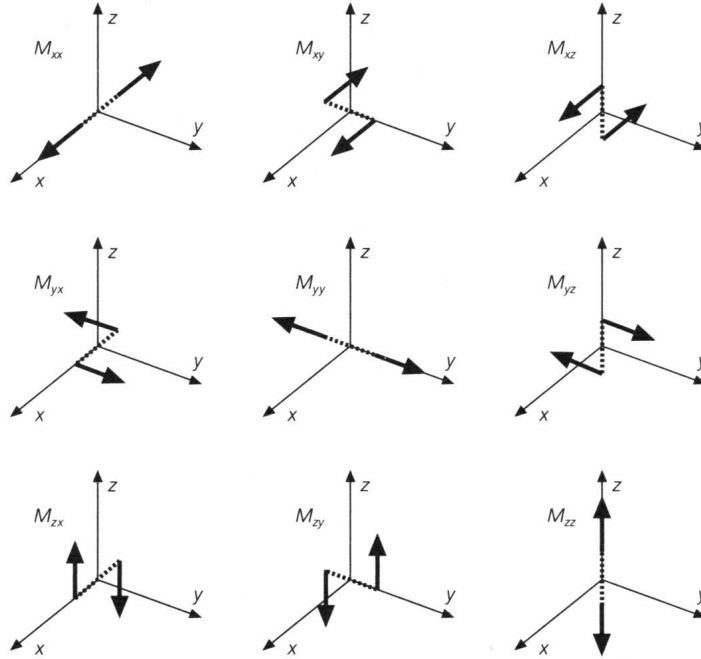


Figure 2.1: The nine force couples of the seismic moment tensor (from Stein and Wyssession (2003)).

offset in direction normal to their orientation and thus apply a net torque. However, because of the symmetry of the moment tensor, the conservation of angular momentum is guaranteed. The diagonal elements correspond to force dipoles acting along the coordinate axes. As all tensors \mathbf{M} can be rotated into its system of principal axes $\hat{\mathbf{e}}^i$. Thus each arbitrary isotropic moment tensor can be expressed as three force dipoles that are eigenvectors of \mathbf{M} , using the eigenvalue equation:

$$\mathbf{M}\hat{\mathbf{e}}^i = \lambda\hat{\mathbf{e}}^i \quad (2.26)$$

Hence by rotating a moment tensor into its system of eigenvectors, it is expressed by three force dipoles: the so-called pressure-/P-axis $\hat{\mathbf{e}}^P = \hat{\mathbf{e}}^1$, the tension-/T-axis $\hat{\mathbf{e}}^T = \hat{\mathbf{e}}^2$ and the null-/B-axis $\hat{\mathbf{e}}^B = \hat{\mathbf{e}}^3$, with eigenvalues $\lambda_T \geq \lambda_B \geq \lambda_P$, respectively (e.g. Stein and Wyssession, 2003). As the trace of a tensor is an invariant on arbitrary rotations, $\text{tr}(\mathbf{M})$ represents the volumetric part of the earthquake. A moment tensor that describes a volume change $\text{tr}(\mathbf{M}) > 0$ is called isotropic. For $\text{tr}(\mathbf{M}) = 0$ no change of volume takes place, and the moment tensor is denoted deviatoric. Double couple mechanisms are special cases of a deviatoric moment tensors with $\lambda_T = -\lambda_P$ and $\lambda_B = 0$.

A pure double couple focal mechanism describes a slip on a planar fault and is the simplest model for an earthquake. While the moment tensor represents a seismic source by the equivalent forces, slip on a plane describes a concrete fracture process. Thus moment

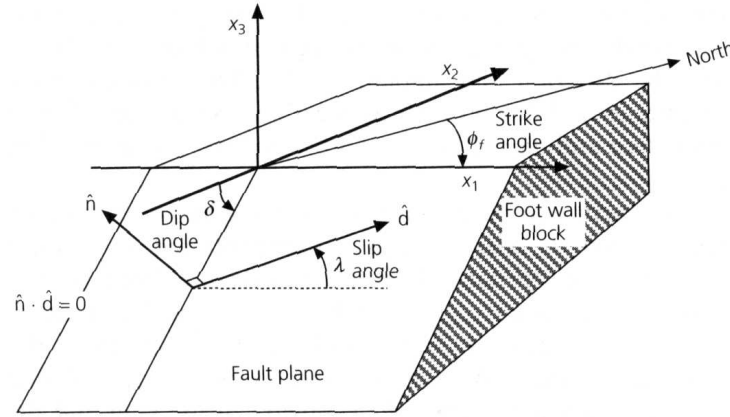


Figure 2.2: Definition of strike ϕ , dip δ and slip λ (from Stein and Wysession (2003)).

tensors can be derived even if the geometrical representation of the source process is more complex than simple slip. The moment tensor elements according to a double couple mechanism can be expressed as the product of shear modulus μ , the rupture area A_F with fault normal vector $\hat{\mathbf{n}}$ and the slip vector $\hat{\mathbf{d}}$ (Jost and Hermann, 1989):

$$M_{ij} = \mu A_F (n_i d_j + n_j d_i) = M_0 (n_i d_j + n_j d_i), \quad (2.27)$$

As a consequence of the symmetry of \mathbf{M} , the slip vector $\hat{\mathbf{d}}$ and the normal vector $\hat{\mathbf{n}}$ are interchangeable in equation 2.27. Thus $\hat{\mathbf{n}}$ and $\hat{\mathbf{d}}$ are often denoted as the normal vectors of the two nodal planes, since for a given moment tensor it is not possible to determine which plane is the true fault plane. The nodal plane on which the rupture really occurred can only be determined by additional information, such as known geological faults, aftershock distributions and directivity effects. The fault geometry can be deduced from the moment tensor eigenvectors and vice versa by:

$$\hat{\mathbf{e}}^P = \frac{1}{\sqrt{2}} (\hat{\mathbf{n}} - \hat{\mathbf{d}}), \quad \hat{\mathbf{e}}^T = \frac{1}{\sqrt{2}} (\hat{\mathbf{n}} + \hat{\mathbf{d}}), \quad \hat{\mathbf{e}}^B = \hat{\mathbf{n}} \times \hat{\mathbf{d}} \quad (2.28)$$

and

$$\hat{\mathbf{n}} = \frac{1}{\sqrt{2}} (\hat{\mathbf{e}}^P + \hat{\mathbf{e}}^T), \quad \hat{\mathbf{d}} = \frac{1}{\sqrt{2}} (\hat{\mathbf{e}}^T - \hat{\mathbf{e}}^P). \quad (2.29)$$

The B-axis is oriented parallel to the line of intersection of the two nodal planes, whereas P- and T-axis bisect the orientation of the plane normals. For a seismic event the P- and T-axis give the resulting directions of compressional and dilatational quadrants, respectively, but generally not the initial orientation of stress. This is due to pre-existing faults, that can be re-activated by various oriented stress tensors, and the fact that newly created rupture mostly occurs at 25° – 30° rather than 45° from orientation of maximum principle stress (section 6.1).

Figure 2.2 shows the angles describing a simple slip on a planar fault that is represented by a double couple moment tensor. The fault geometry is defined by the strike ϕ of the fault measured clockwise against north, the dip δ from the horizontal surface and the slip λ as the counter-clockwise angle between horizontal and slip vector $\hat{\mathbf{d}}$. Using the normal vectors of fault and auxiliary plane gives:

$$\begin{aligned}\tan \phi &= \frac{n_2}{n_3} \\ \tan \delta &= \frac{\sqrt{1 - n_1^2}}{n_1} \\ \tan \lambda &= \frac{d_1}{d_3 n_2 - d_2 n_3}.\end{aligned}\tag{2.30}$$

The introduction and discussion of a pure double couple mechanisms enables the decomposition of an general moment tensor \mathbf{M} to separate isotropic, deviatoric and pure double couple components (*DC*). With

$$\mathbf{M}_{iso} = \frac{1}{3} \text{tr}(\mathbf{M}) \cdot \mathbf{I},\tag{2.31}$$

\mathbf{M} decomposes in an isotropic and a deviatoric component:

$$\mathbf{M} = \mathbf{M}_{iso} + \mathbf{M}_{dev}.\tag{2.32}$$

Since $\text{tr}(\mathbf{M}_{dev}) = 0$ and the set of principle axes do not change for the deviatoric moment tensor \mathbf{M}_{dev} , it can be separated into two *DC*-mechanisms or a *DC* and a *CLVD* (Compensated Linear Vector Dipole). For this purpose the deviatoric moment tensor is rotated in its system of eigenvectors, so the eigenvalues become the diagonal elements, as off-diagonal elements are zero:

$$\begin{aligned}\mathbf{M}_{dev} &= \begin{pmatrix} \lambda_1 & 0 & 0 \\ 0 & \lambda_2 & 0 \\ 0 & 0 & \lambda_3 \end{pmatrix}; \quad |\lambda_1| \geq |\lambda_2| \geq |\lambda_3| \\ &= \underbrace{\begin{pmatrix} \lambda_1 & 0 & 0 \\ 0 & -\lambda_1 & 0 \\ 0 & 0 & 0 \end{pmatrix}}_{\text{major DC}} + \underbrace{\begin{pmatrix} 0 & 0 & 0 \\ 0 & -\lambda_3 & 0 \\ 0 & 0 & \lambda_3 \end{pmatrix}}_{\text{minor DC}} \\ &= \underbrace{\begin{pmatrix} \frac{2\lambda_1 + \lambda_3}{2} & 0 & 0 \\ 0 & -\frac{2\lambda_1 + \lambda_3}{2} & 0 \\ 0 & 0 & 0 \end{pmatrix}}_{DC} + \underbrace{\begin{pmatrix} -\frac{\lambda_3}{2} & 0 & 0 \\ 0 & -\frac{\lambda_3}{2} & 0 \\ 0 & 0 & \lambda_3 \end{pmatrix}}_{CLVD}.\end{aligned}\tag{2.33}$$

The double couple percentage p contained in an arbitrary moment tensor arises from the ratio of the smallest to the largest eigenvalue or the moments of minor to major *DC* (eqn. 2.21):

$$p = (1 - 2\epsilon) \cdot 100\%; \quad \epsilon = \left| \frac{\lambda_3}{\lambda_1} \right| = \frac{M_{0,min}}{M_{0,maj}}.\tag{2.34}$$


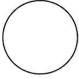










| Moment Tensor | Beachball | Moment Tensor | Beachball |
|---|--|--|--|
| $\frac{1}{\sqrt{3}} \begin{pmatrix} 1 & 0 & 0 \\ 0 & 1 & 0 \\ 0 & 0 & 1 \end{pmatrix}$ |  | $-\frac{1}{\sqrt{3}} \begin{pmatrix} 1 & 0 & 0 \\ 0 & 1 & 0 \\ 0 & 0 & 1 \end{pmatrix}$ |  |
| $-\frac{1}{\sqrt{2}} \begin{pmatrix} 0 & 0 & 0 \\ 0 & 0 & 1 \\ 0 & 1 & 0 \end{pmatrix}$ |  | $\frac{1}{\sqrt{2}} \begin{pmatrix} 0 & 0 & 0 \\ 0 & 1 & 0 \\ 0 & 0 & -1 \end{pmatrix}$ |  |
| $\frac{1}{\sqrt{2}} \begin{pmatrix} 0 & 1 & 0 \\ 1 & 0 & 0 \\ 0 & 0 & 0 \end{pmatrix}$ |  | $\frac{1}{\sqrt{2}} \begin{pmatrix} 0 & 0 & 1 \\ 0 & 0 & 0 \\ 1 & 0 & 0 \end{pmatrix}$ |  |
| $\frac{1}{\sqrt{2}} \begin{pmatrix} 1 & 0 & 0 \\ 0 & -1 & 0 \\ 0 & 0 & 0 \end{pmatrix}$ |  | $\frac{1}{\sqrt{2}} \begin{pmatrix} 1 & 0 & 0 \\ 0 & 0 & 0 \\ 0 & 0 & -1 \end{pmatrix}$ |  |
| $\frac{1}{\sqrt{6}} \begin{pmatrix} 1 & 0 & 0 \\ 0 & 1 & 0 \\ 0 & 0 & -2 \end{pmatrix}$ |  | $\frac{1}{\sqrt{6}} \begin{pmatrix} 1 & 0 & 0 \\ 0 & -2 & 0 \\ 0 & 0 & 1 \end{pmatrix}$ |  |
| $\frac{1}{\sqrt{6}} \begin{pmatrix} -2 & 0 & 0 \\ 0 & 1 & 0 \\ 0 & 0 & 1 \end{pmatrix}$ |  | $-\frac{1}{\sqrt{6}} \begin{pmatrix} -2 & 0 & 0 \\ 0 & 1 & 0 \\ 0 & 0 & 1 \end{pmatrix}$ |  |

Figure 2.3: Standard moment tensors and their beachball representation (from [Dahlen and Tromp \(1998\)](#)). Row 1: isotropic moment tensor (pure explosion and implosion); Rows 2–4: pure *DC*. Row 2: strike slip (left-lateral N-S and NW-SE); Row 3: vertical dip-slip (strike E-W and N-S); Row 4: thrust (strike E-W and N-S); Rows 5–6: *CLVD*'s.

Hence, for a pure *CLVD* applies $p = 0\%$ ($\epsilon = 0.5$) and for a pure *DC*: $p = 100\%$ ($\epsilon = 0$) ([Giardini, 1984](#)). Since the most stable part of the moment tensor is the *DC*-component, a high *DC*-percentage p is often used as an indicator for a stable inversion result ([Bernardi et al., 2004](#)). [Kuge and Lay \(1994\)](#) showed that the poor resolution of $M_{xy} = M_{yx}$ and $M_{xz} = M_{zx}$ present in surface wave moment tensor inversion can lead to artificial non-*DC* parts and thus a high *DC*-percentage p . Other reasons for a high *DC*-percentage p that do not imply an unstable inversion can be found in inaccurate source locations or crustal heterogeneities ([Zhang and Lay, 1990](#); [Henry et al., 2002](#)).

Moment tensors are graphically represented by so-called beachballs. They show compressional areas (blackened or coloured, containing the P-axis) and dilatational areas (no fill, containing the T-axis) projected on a lower hemisphere stereographic map. In case of a double couple mechanism the nodal planes, that correspond to the orientations of fault and auxiliary plane, divide the earth in quadrants of compression and dilatation. Figure 2.3 gives an overview of some characteristic examples.

2.3 Inversion of the moment tensor

If the earth's structure is known and long-period waveform data is available, the seismic moment tensor \mathbf{M} and thus the focal mechanism of an earthquake can be calculated by inversion. Since generally more independent data than model-parameters are available, the inversion problem is over-determined. After [Kennett \(1976\)](#) equation 2.24 can be written as:

$$\mathbf{s} = \mathbf{G}\mathbf{m}, \quad (2.35)$$

with the model vector $\mathbf{m} = (m_1, m_2, m_3, m_4, m_5, m_6)^T$ that consists of the six independent elements of the symmetric moment tensor:

$$\mathbf{M} = \begin{pmatrix} m_1 & m_4 & m_5 \\ m_4 & m_2 & m_6 \\ m_5 & m_6 & m_3 \end{pmatrix}. \quad (2.36)$$

The data vector \mathbf{s} contains the frequency amplitudes and phase informations for every waveform included. Since the isotropic component of the moment tensor \mathbf{M} is not well resolvable for shallow events ([Kawakatsu, 1996](#); [Dziewonski et al., 1981](#)), \mathbf{M} is constrained to be deviatoric by setting $\text{tr}(\mathbf{M}) = 0$ ([Bernardi et al., 2004](#); [Giardini, 1992](#)) that reduces the moment tensor to five independent elements.

The Green's function \mathbf{G} consists of the excitation amplitudes (eqn. 2.23) that—in approximation of a point source—can be calculated beforehand using the one-dimensional earth model PREM ([Dziewonski and Anderson, 1981](#)). During inversion in the frequency domain the excitation amplitudes can be accessed without renewed calculation, since they are only dependent on azimuth, distance and degree k of the normal modes.

Since \mathbf{G} is not symmetric and hence equation 2.37 describes an overdetermined problem, it is necessary to calculate the generalised inverse of the Green's function \mathbf{G} to solve equation 2.35 for the model vector \mathbf{m} :

$$\mathbf{m} = (\mathbf{G}^T \mathbf{G})^{-1} \mathbf{G}^T \mathbf{s}. \quad (2.37)$$

The misfit between input data $\mathbf{s}(\omega)$ and synthetic data $\mathbf{s}'(\omega)$ calculated by the obtained moment tensor is given by the variance

$$\sigma = \frac{[\text{Re}(\mathbf{s}) - \text{Re}(\mathbf{s}')]^2 + [\text{Im}(\mathbf{s}) - \text{Im}(\mathbf{s}')]^2}{\text{Re}(\mathbf{s})^2 + \text{Im}(\mathbf{s})^2}. \quad (2.38)$$

To investigate the resolvability of the moment tensor in this work a different inversion approach is used additionally. The singular value decomposition (*SVD*) separates the moment tensor into its eigenvectors. A detailed description of the *SVD* can be found at [Parker \(1994\)](#). Thus the matrix \mathbf{G} decomposes into three parts:

$$\mathbf{G} = \mathbf{U}_p \mathbf{\Lambda}_p \mathbf{V}_p^T. \quad (2.39)$$

Matrix \mathbf{V}_p contains the non-zero model-eigenvectors \mathbf{v}_i and matrix \mathbf{U}_p the non-zero data-eigenvectors \mathbf{u}_i . $\mathbf{\Lambda}_p$ is a diagonal matrix including the eigenvalues λ_i . After [Kawakatsu \(1996\)](#) the moment tensor trace elements can be written by a nearly independent set of model parameters:

$$\begin{aligned} m'_1 &= (m_1 + m_2 + m_3) / 3 \\ m'_2 &= (-2m_1 + m_2 + m_3) / 3 \\ m'_3 &= (m_2 + m_3) / 2 \\ m'_4 &= m_4; \quad m'_5 = m_5; \quad m'_6 = m_6, \end{aligned} \quad (2.40)$$

to explicitly discriminate between isotropic and deviatoric parts. Thus this formulation can be used to exclude the isotropic part from the inversion and the deviatoric model vector \mathbf{m}_{dev} can be written as :

$$\mathbf{m}_{dev} = (m'_2, m'_3, m'_4, m'_5, m'_6)^T. \quad (2.41)$$

Since the data vector consists of spectral amplitudes for all seismic stations used, it has many more elements than the model vector containing only the five independent elements of the deviatoric moment tensor. Thus the inversion problem is overdetermined and can be inverted by:

$$\mathbf{m}_{dev} = \mathbf{V}_p \mathbf{\Lambda}_p^{-1} \mathbf{U}_p^T \mathbf{s} = \sum_{i=1}^5 \mathbf{v}_i \frac{\mathbf{u}_i \mathbf{s}'}{\lambda_i}; \quad \lambda_i \geq \lambda_{i+1}. \quad (2.42)$$

Model eigenvectors with small eigenvalues do not decrease the data misfit significantly and rather model inconsistent noise ([Forbriger, 2001](#)). Thus it is worthwhile to consider a moment tensor solution only composed by the l model eigenvectors with the largest eigenvalues:

$$\mathbf{m}_{cut,l} = \sum_{i=1}^l \mathbf{v}_i \frac{\mathbf{u}_i \mathbf{s}'}{\lambda_i}. \quad (2.43)$$

In section [5.4](#) the consequences of reducing the model vector by one model eigenvector will be discussed. It will be shown that in some cases the double couple percentage p (eqn. [2.34](#)) can be increased for $l = 4$ while the included double couple pattern is conserved.

Chapter 3

Frequency sensitive moment tensor inversion

3.1 Seismic data

Recordings of broadband and long-period seismometers in regional to teleseismic distances are used to investigate source mechanisms of earthquakes $M_W \leq 5.0$ in eastern Africa. Generally, the seismometer distribution is sparse and source-receiver distances are up to 3300 km. Therefore, the analysis had to be restricted to times for that sufficient data is available.

The first permanent digital long-period seismic sensors in Africa were already installed 1975–1985 (SUR, RER, ATD and others not maintained any longer), but since 1993 the number of stations increased to the today’s amount (Table 3.1). Thus moment tensor inversion of light to moderate sized earthquakes in eastern Africa is restricted to time periods, sufficient data are available for. In this work only earthquakes that occurred later than 1994 are considered, when five permanent recording seismometers were operating in eastern Africa and neighbouring regions. Until 1999 the number of permanent stations increased to 13, thus a good azimuthal distribution with respect to eastern Africa is provided, with only two minor gaps in the west and south-southeast (Fig. 3.1).

The locations of seismometers in eastern Africa and neighbouring regions that are used in this study are listed in Table 3.1. Waveform data of all stations are available online in *SEED*-format via the *IRIS*-datacenter Washington (<http://www.iris.edu/SeismiQuery/>) or using the *BREQ_FAST* e-mail client.

To gather the set of earthquakes that shall be studied, events are taken from the Engdahl catalogue of relocated earthquakes (Engdahl et al., 1998). Events must have occurred in the time period from 1994 to 2002 and the study region is limited in latitude from 24°S to 10°N and in longitude from 20°E to 51°E. Only events are considered for that no Harvard *CMT*-solution was determined previously (e.g. Ekström et al., 2005) and that have a magnitude

Table 3.1: Permanent seismic stations in eastern Africa and neighbouring regions used for the moment tensor inversion.

| name | network | lat | lon | rec. since yr-mo-day | altitude [m] |
|-------------------|---------|--------|-------|-------------------------|-----------------|
| ATD ¹ | G | 11.53 | 42.85 | 1985-03-09 | 610 |
| BGCA | GT | 5.18 | 18.42 | 1994-07-21 | 676 |
| BOSA | GT | -28.61 | 25.26 | 1993-02-26 | 1280 |
| FURI ² | IU | 8.90 | 38.69 | 1994-12-12 | 2545 |
| KMBO ³ | GE,IU | -1.13 | 37.25 | 1995-01-05 | 1960 |
| LBTB | GT | -25.02 | 25.60 | 1993-04-17 | 1128 |
| LSZ | IU | -15.28 | 28.19 | 1994-08-05 | 1184 |
| MBAR | II | -0.60 | 30.74 | 1999-09-22 | 1390 |
| MSEY | II | -4.67 | 55.48 | 1995-05-15 | 475 |
| MSKU | IU | -1.66 | 13.61 | 1999-02-27 | 312 |
| NAI ³ | GE,IU | -1.27 | 36.80 | 1995-01-05 | 1692 |
| RER ⁴ | G | -21.16 | 55.75 | 1982-07-25 | 834 |
| SUR | II | -32.38 | 20.81 | 1975-12-12 | 1770 |
| TSUM | IU | -19.20 | 17.58 | 1994-08-19 | 1240 |

Network codes as follows: G: GEOSCOPE, GE: GEOFON, GT: GTSN/GSN (USAF/USGS), II: GSN (IRIS/IDA), IU: GSN (IRIS/USGS).

of $m_b \geq 4.5$ or $M_S \geq 4.5$. By these restrictions 61 events are extracted from the catalogue with magnitudes ranging from $m_b = 3.5$ to 5.5 (Table A.3). The events are distributed over the East African Rift System and adjacent areas (Fig. 3.1). The routine Harvard-*CMT* source mechanism determination is complete down to $M_W \approx 5.5$ on a global scale (Arvidsson and Ekström, 1998) and down to $M_W \approx 5.3$ for eastern Africa (see section 5.5). Thus the extracted dataset includes 12 events reported to have magnitudes $m_b \geq 5.0$ for that no *CMT*-solution was calculated. All events have standard errors in position less than 18 km (9.3 km on average), except one event (2001-01-31, event 30) for which no location error is given for (Engdahl, personal communication). A location error of 18 km would result in a traveltimes residual of 6 s assuming a low Rayleigh-wave group-velocity of 3 km/s. Nevertheless, uncertainties of this size are not critical for moment tensor inversion, since traveltimes residuals are compensated up to a quarter of the minimal inverted period (see section 3.2).

¹AGD replaced by ATD 1990-12-08

²AAE replaced by FURI 1997-09-01

³NAI replaced by KMBO 1995-09-17

⁴PCR replaced by RER 1986-02-10

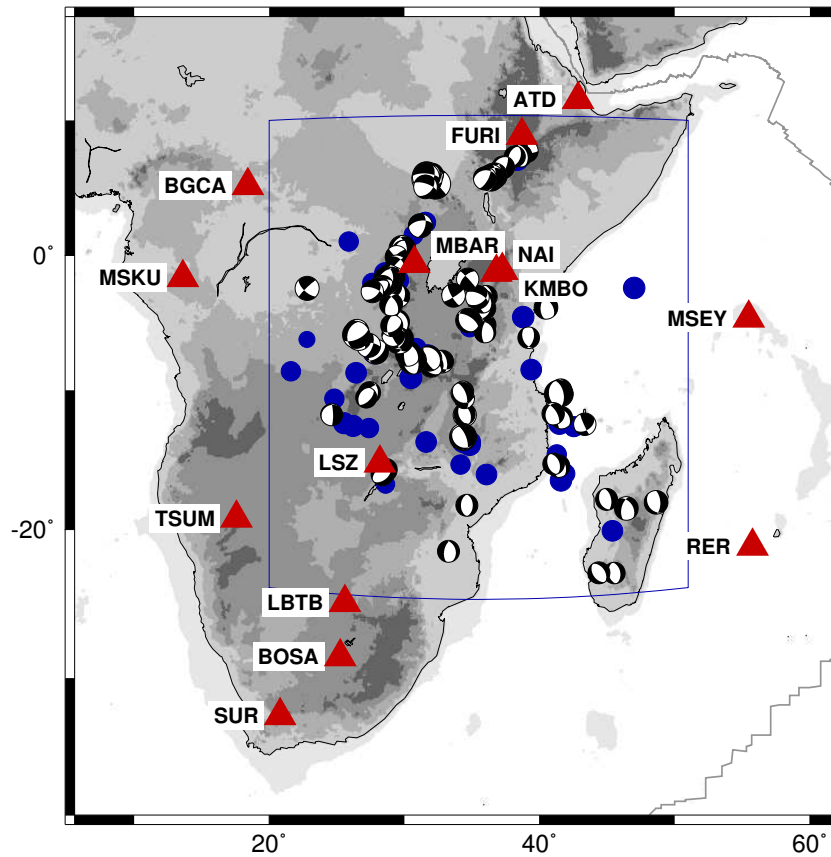


Figure 3.1: Seismic station distribution (red triangles) in eastern Africa and neighbouring regions. The box defines the study region including seismicity from 1994 to 2002 with $m_b \geq 4.5$ (blue dots, Engdahl et al., 1998). Plotted focal mechanisms are taken from Harvard *CMT*-solutions (e.g. Dziewonski et al., 2003).

For general applicability the one-dimensional velocity model PREM (Dziewonski and Anderson, 1981) is used to calculate the synthetic waveforms for the moment tensor inversion. However, this restricts the inversion to long-period waves, that are less influenced by structural heterogeneities than short periods (Larson and Ekström, 2001). Šílený (2004) showed that periods $\mathcal{T} \geq 35$ s are sufficient for the determination of moment tensors for light to moderate sized events using a one-dimensional earth model. Beside this short-period limit, the usable waveform data are also limited for long-period waves. Low magnitude earthquakes provide amplitudes higher than the seismic noise level only at waves of rather short periods, when recorded at teleseismic distances. Thus for the moment tensor determination in regions of only intermediate seismicity and sparse seismometer coverage, source-relevant data of long-period waves ($\mathcal{T} > 100$ s) disappear within the seismic noise. These two limits restrict the data used in this study to periods $\mathcal{T} = 35\text{--}100$ s ($f = 10\text{--}29$ mHz).

Waveform quality differs with source-receiver distance, earthquake magnitude, local noise

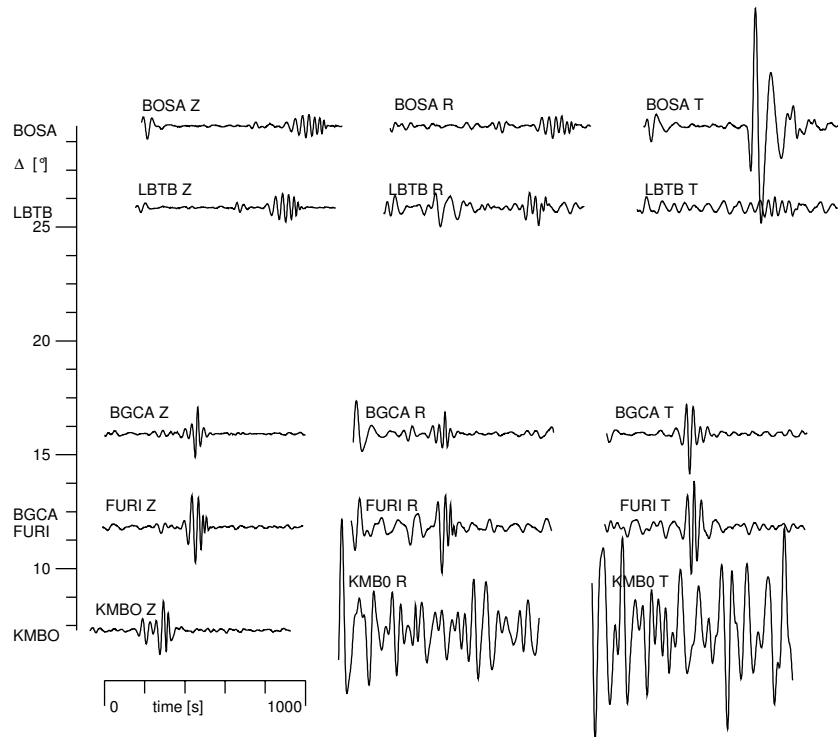


Figure 3.2: Seismograms of the seismic event on 31 January 2001 (event 30). Data are corrected for the instrument response and band-pass filtered between 10 mHz and 29 mHz. Station names on the vertical axis indicate source-receiver distance Δ . Seismometer components are plotted in columns: vertical component Z on the left, radial R and transverse T component in the middle and on the right, respectively. Displayed amplitudes are not scaled.

conditions and temporally effects as weather phenomena or human activity. Another effect in seismic source studies is that long-period amplitudes azimuthally depend on the radiation of the source mechanism (section 2.1). Thus regarding low magnitude earthquakes, signal amplitudes for similar source-receiver distance but different azimuthal direction either can be just below or just above the noise level.

To show the different restrictions of using waveform data for moment tensor inversion, Figure 3.2 displays the waveform components recorded for the earthquake on 31 January 2001 (event 30). Data are corrected for the instrument response and band-pass filtered from 10 mHz to 29 mHz (4th order butterworth filter, [Stammler, 1993](#)). Most prominent are the two very noisy horizontal components of station KMBO that are most reasonable due to local effects, since they often record noisy data and as a consequence are used for the calculation of two earthquake source mechanisms only. BOSA(T), that in general provides high quality data (section 5.3), obviously is biased by an instrumental effect, since the other two components, Z and R , show a transient earthquake signal. Thus BOSA(T) as

well as $KMBO(R, T)$ cannot be used for the moment tensor inversion. All other waveforms provide moderate to high signal-to-noise ratios. As mentioned above long-period waveform amplitudes can vary strongly in dependence of the source mechanism. Comparing $BGCA(R)$ and $BGCA(T)$, the Love-wave train recorded on the transverse component has a higher amplitude than the Rayleigh-wave on the radial component (Fig. 3.2). Also as a consequence of the source radiation pattern the highest amplitude of vertical components is given by FURI and not by KMBO which is the station nearest to the source.

Waveform data can be biased severely by local effects such as atmospheric phenomena, heterogeneities in velocity structure or just a general high noise level (section 5.3) and often different kinds of noise sources coincide. Thus, to perform a stable earthquake source study, first of all a reliable waveform dataset has to be compiled. In this work this is done automatically by inverting the source-relevant long-period part of each waveform trace at first solely to determine waveform traces with a high signal-to-noise ratio.

3.2 Frequency sensitive processing

A damped least squares moment tensor inversion in the frequency-domain is used to match the spectral amplitude pattern radiated by light to intermediate sized earthquakes that were recorded in regional and teleseismic source-receiver distances (Giardini, 1992; Bernardi et al., 2004). After correcting waveform traces for the station response, the original seismometer system of vertical component Z with the horizontal components North N and East E is rotated in the ZRT system. Hereby the horizontal radial component R is rotated in direction of theoretical backazimuth and the horizontal transverse component T perpendicular to it. The deconvolution of the instrument response, the rotation of the horizontal components and the band-pass filtering was realised using *SeismicHandler* (Stammler, 1993). Then a Fourier transform is applied for a time window of 900 s (15 min.) beginning 200 s before the theoretical P-wave arrival and thus containing body waves and the main part of the surface wave train for source-receiver distances of up to 3300 km. Re-alignment of individual waveform components Z , R and T in the time-domain is allowed to take account of traveltimes delays present at intermediate periods (Giardini, 1992; Arvidsson and Ekström, 1998). In this work identical time-shifts Δt for the radial and vertical component (Z, R) are applied to fit Rayleigh- and P-waves, as an individual time-adjustment is allowed for the transverse component T containing the horizontally polarised Love- and S-waves. So the moment tensor inversion is performed for different time-shifts to find the best waveform fit. The re-alignments are restricted to a quarter of the smallest inverted period \mathcal{T}^{min} to prevent polarity changing phase-shifts:

$$\Delta t \leq \frac{\mathcal{T}^{min}}{4} = \frac{1}{4f^{max}}. \quad (3.1)$$

Thus for the maximum frequency $f^{max} = 29$ mHz used in this work, the maximum time-shift allowed is $\Delta t = (4 \cdot 29 \text{ mHz})^{-1} = 8.8$ s. Time-shifts of this order does increase the

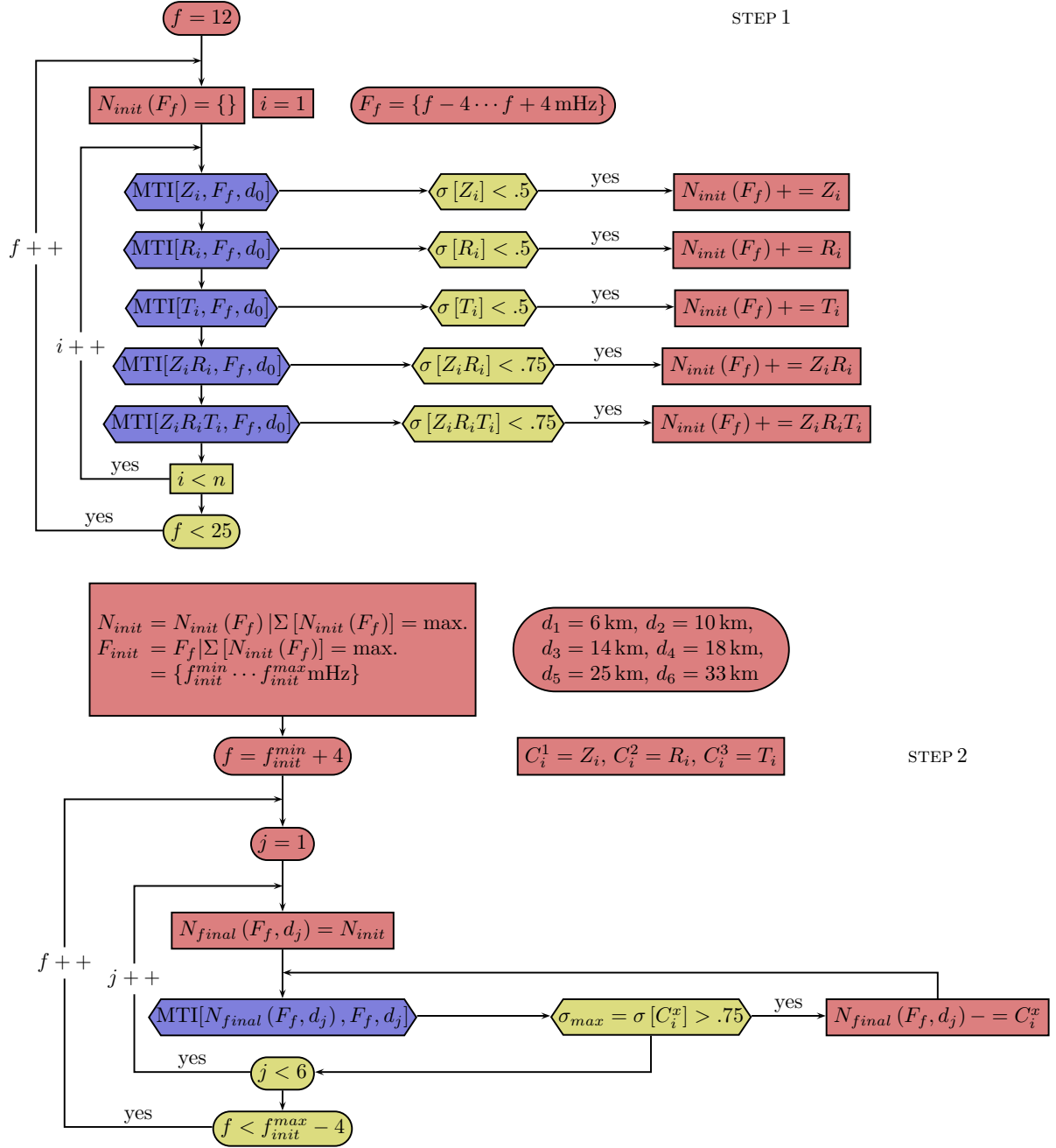


Figure 3.3: STEP 1 and STEP 2 of the processing scheme of the frequency sensitive moment tensor inversion applied for each earthquake. Details see text.

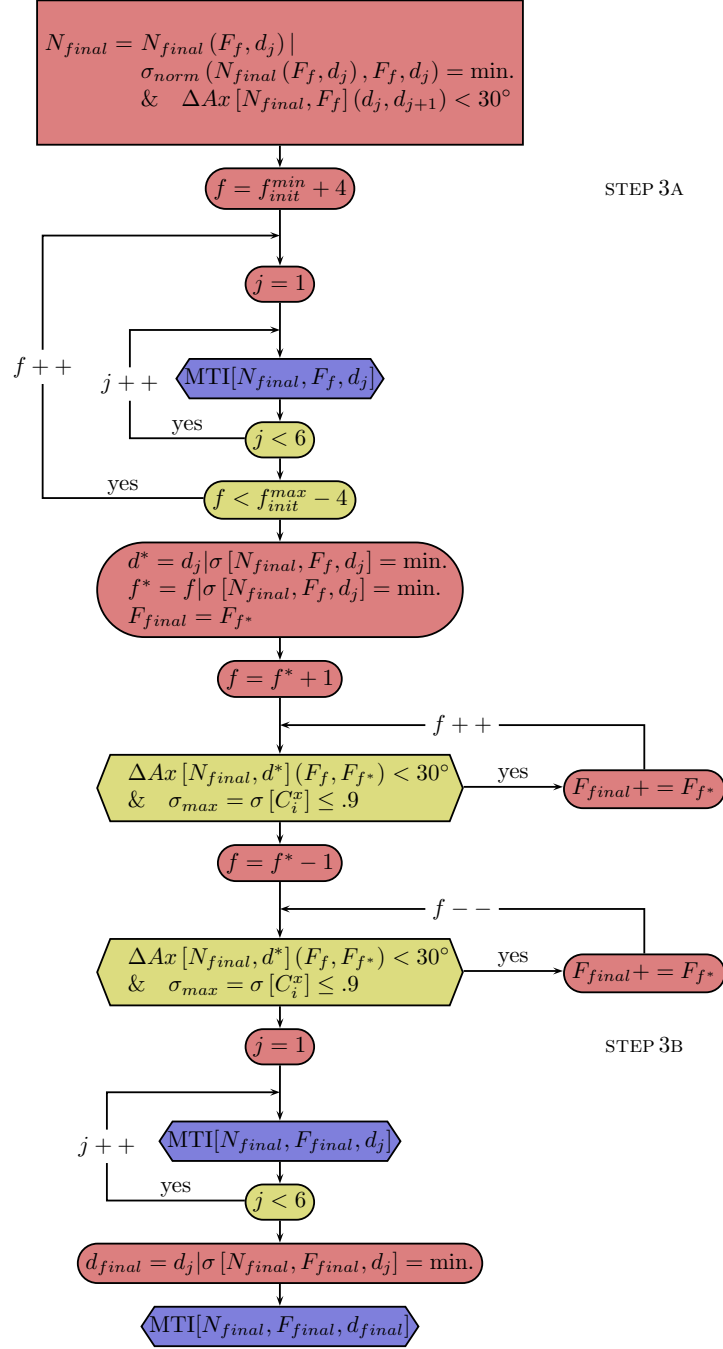


Figure 3.4: STEP 3 of the processing scheme of the frequency sensitive moment tensor inversion applied for each earthquake. Details see text.

waveform fit but do not significantly change the final focal mechanism (Arvidsson and Ekström, 1998).

The inversion has a limited depth resolution since long and intermediate period surface waves excitation functions do not vary much with source depth (Giardini, 1992). Hence discrete crustal hypocentral depths are used (6, 10, 14, 18, 25, 33 and for some events 42 km) (Bernardi et al., 2004). Synthetics are generated by normal mode summation (Woodhouse, 1988) for the one-dimensional PREM earth model (Dziewonski and Anderson, 1981), that makes the inversion routine easily transferable to regions worldwide.

In this study a frequency sensitive moment tensor inversion is performed to account for the difficulties of source mechanism analysis of light to intermediate sized earthquakes recorded in regional to teleseismic distances. The semi-automatic data processing follows a strict scheme and includes three steps: STEP 1) Determination of an initial dataset N_{init} (for an initial and representative frequency range F_{init}); STEP 2) Extraction of the final data set N_{final} in dependence on hypocentral depth and inverted frequency range; STEP 3) Frequency sensitive analysis for the final dataset to determine the final frequency range F_{final} and the optimum hypocentral depth d_{final} . Figures 3.3 and 3.4 illustrate the processing schematically: colour and shape of the boxes indicate their function and content. The resulting parameters and the moment tensor inversion itself (MTI, blue colour) are symbolised by hexagonal shape. Rectangular shapes mark waveform datasets N , as rounded boxes symbolise frequency or hypocentral depth. Red colour stands for definitions or changes of parameters, and yellow boxes indicate conditions. The available number of seismic stations for each event i is n , and in general six discrete hypocentral depths d_j are regarded (additionally $d_7 = 42$ km for special events).

(STEP 1) Because of large source-receiver distances, low earthquake magnitude, site dependent seismic noise and crustal heterogeneities along the travel paths of the recorded waves, some waveforms are not usable for the moment tensor inversion (section 3.1). Thus at first, each available single seismometer component is reviewed by moment tensor inversion whether its waveform could be explained by an arbitrary source mechanism and the one-dimensional earth model. The inversion is performed for a sliding 8 mHz wide frequency band F_f between 8 mHz and 29 mHz with a mid-frequency f and a constant hypocentral depth d_0 given by Engdahl et al. (1998). For each frequency band the variance σ (eqn. 2.38) between observed and synthetic waveforms is calculated in the frequency domain, to estimate whether the one-dimensional earth model is sufficient to explain the recorded seismic waves. The same initial inversion is performed for a combination of Z - and R -components that record the P- and the Rayleigh-waves and for the set of all components (Z, R, T) of a seismometer. Variance limits have been defined to separate explainable data and such biased by noise and effects of crustal complexity. For the single component inversion $\sigma \leq 0.5$ has to be fulfilled, whereas for the inversion of (Z, R) and (Z, R, T) $\sigma \leq 0.75$ must be valid. These variance limits are determined empirically to receive a robust initial dataset, including a high amount of source-relevant waveform information (compare section 5.3). Thus for each frequency range F_f an initial dataset $N_{init}(F_f)$ is determined that only includes waveforms that fulfil the variance criteria.

Finally, the frequency independent initial dataset N_{init} is taken for the frequency range F_f with the highest number of components $\Sigma [N_{init}(F_f)]$. The initial frequency range F_{init} then is assigned by extending F_f to frequencies with a similarly high amount of explainable data. To practically demonstrate the described processing steps, they will be discussed on the basis of an example in section 4.2.

(STEP 2) Next the subset $N_{final} = N_{init}$ is reduced to the set of waveforms that could be explained by a common moment tensor: One by one the waveform explained worst is excluded from the subset $N_{final}(F_f, d_j)$ and the inversion is performed again until the waveform components $C^x = \{Z, R, T\}$ for all stations i have an individual variance $\sigma [C_i^x] \leq 0.75$. This step is repeated for a sliding frequency band F_f within the frequency range F_{init} in combination with discrete crustal source depths d_j . The iterative procedure reduces $N_{final}(F_f, d_j)$ to an individual dataset for each depth-frequency combination.

To include a high number of waveforms $\Sigma [N_{final}(F_f, d_j)]$ with a low variance σ in the final dataset N_{final} , for this part of the procedure the normalised variance σ_{norm} is introduced. It is used for the determination of the optimum dataset $N_{final}(F_f, d_j)$:

$$\sigma_{norm} = 3\sigma / (\Sigma [N_{final}(F_f, d_j)] - 3) \rightarrow \min. \quad (3.2)$$

Hence variances for inversions of six waveforms remains unchanged, whereas $\sigma \geq \sigma_{norm}$ for more than six inverted waveforms. Equation 3.2 is derived empirically and proves to be a convenient criteria for automatically determining N_{final} with a high number of waveform traces and a sufficient variance level. To avoid the choice of a focal mechanism solution that varies strongly from the mechanisms of adjacent inverted frequencies, only solutions for depth-frequency combinations are chosen that are similar to the inversion results for frequency pass-bands shifted by 1 mHz in positive or negative direction. To define similarity of two focal mechanisms the average difference in orientation of the principal axes of two moment tensor $|\Delta Ax| < 30^\circ$ is used. After Bernardi et al. (2004) $|\Delta Ax|$ is defined by the sum of angular differences $\sphericalangle (\mathbf{e}^a - \mathbf{e}^b)$ between the principal axes of two focal mechanisms a and b expressed as $\mathbf{p} = \mathbf{e}_1$, $\mathbf{b} = \mathbf{e}_2$ and $\mathbf{t} = \mathbf{e}_3$ (eqn. 2.28):

$$|\Delta Ax| = \frac{1}{3} \sum_i \Delta x_i = \frac{1}{3} \sum_i \sphericalangle (\mathbf{e}_i^a - \mathbf{e}_i^b) \quad (3.3)$$

This step of the so far automatic procedure is controlled manually. If the algorithm proposes a depth-frequency pair that still is isolated in the depth-frequency space, a focal mechanism solution with a low variance σ_{norm} in a stable depth-frequency region is chosen instead.

(STEP 3) This last step of the procedure is divided in two parts. (A) At first the final frequency range F_{final} is determined and (B) thereafter the hypocentral depth d_{final} of the earthquake is estimated.

(A) As the previous steps are necessary to obtain the waveform dataset, now the frequency sensitive inversion is performed for the final dataset N_{final} . The inversion for the deviatoric

moment tensor is applied for the discrete source depths and the frequency range F_{init} by sliding frequency bands. The depth-frequency pair with the lowest variance σ is selected and the band-width extended to the widest range of similar focal mechanisms ($|\Delta Ax| < 30^\circ$) with individual variances $\sigma [C_i^x] \leq 0.9$. Hence the minimum variance frequency range F_{final} of stable source mechanisms is obtained.

(B) At last the inversion of the fixed dataset N_{final} and frequency band F_{final} for the discrete source depths determines the hypocentral depth d_{final} with the lowest variance σ (Fig. 4.5). Here p , the percentage of double couple (eqn. 2.34), is considered as a controlling parameter for the estimation of hypocentral depth, since very low values of p are a hint of unstable inversion results (section 5.1). So if the minimum variance solution has $p \leq 30\%$, the hypocentral depth d_{final} is chosen for which the inversion results in both, low variance σ and rather high p . This is not the general case, so this manual adaption is only necessary for events number 16, 23 and 26 (see Appendix B for details).

Chapter 4

Moment tensor solutions

4.1 Inversion results

Using the frequency sensitive moment tensor inversion described in the previous section, 38 reliable moment tensors are calculated out of 61 events investigated (Table A.3). For the remaining earthquakes no focal mechanism is given in this study, since for these events N_{final} is determined to contain less than six consistent waveform components and thus the quantity of data is not sufficient for an inversion (processing STEP 2, see section 3.2). The obtained 38 source mechanisms are determined for earthquakes with moment magnitudes that range from M_W 4.4 to M_W 5.5 (median $M_W = 4.8$). Although earthquakes since 1994 are considered, the earliest event for that a focal mechanism is determined took place on 1995-04-27. The two events that occurred in 1994 were recorded by two, respectively three seismometers only and thus not enough data are provided for the inversion. The individual focal mechanism solutions are shown in mapview in Figure 4.1, and quantitative inversion results of all events are given in Table A.1. As expected the majority of analysed events concentrates along the East African Rift System, but 13 moment tensors are determined for earthquakes in neighbouring regions. Individual earthquakes will be discussed in the context of the regional tectonics in section 5.2. In Appendix B detailed results for each inversion are presented. For each event three figures are shown: the frequency sensitive inversion of N_{final} (STEP 3A of the processing), the depth-variance analysis for N_{final} and F_{final} (STEP 3B) and the final inversion with synthetics displayed for each waveform component included in the final dataset N_{final} (compare Fig. 3.3, 3.4). Figures are listed chronologically as in Table A.1 and geographical earthquake locations are given following the seismo-tectonic *Flinn-Engdahl*-regionalisation scheme (Flinn et al., 1974).

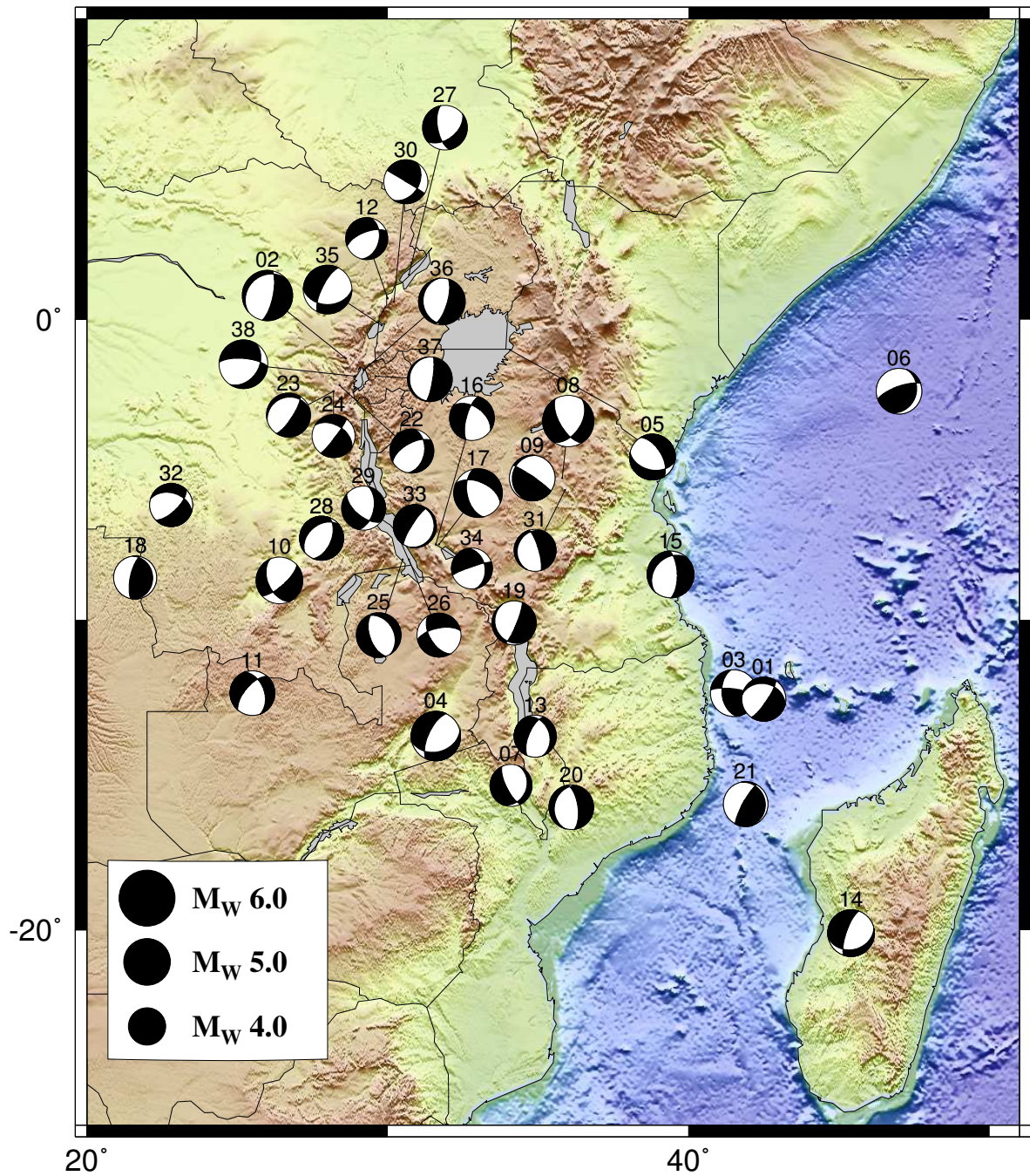


Figure 4.1: Result of the frequency sensitive moment tensor inversion showing the 38 determined focal mechanisms (double couple part). Beach balls are scaled by moment magnitude M_W . Numbering see Table A.1.

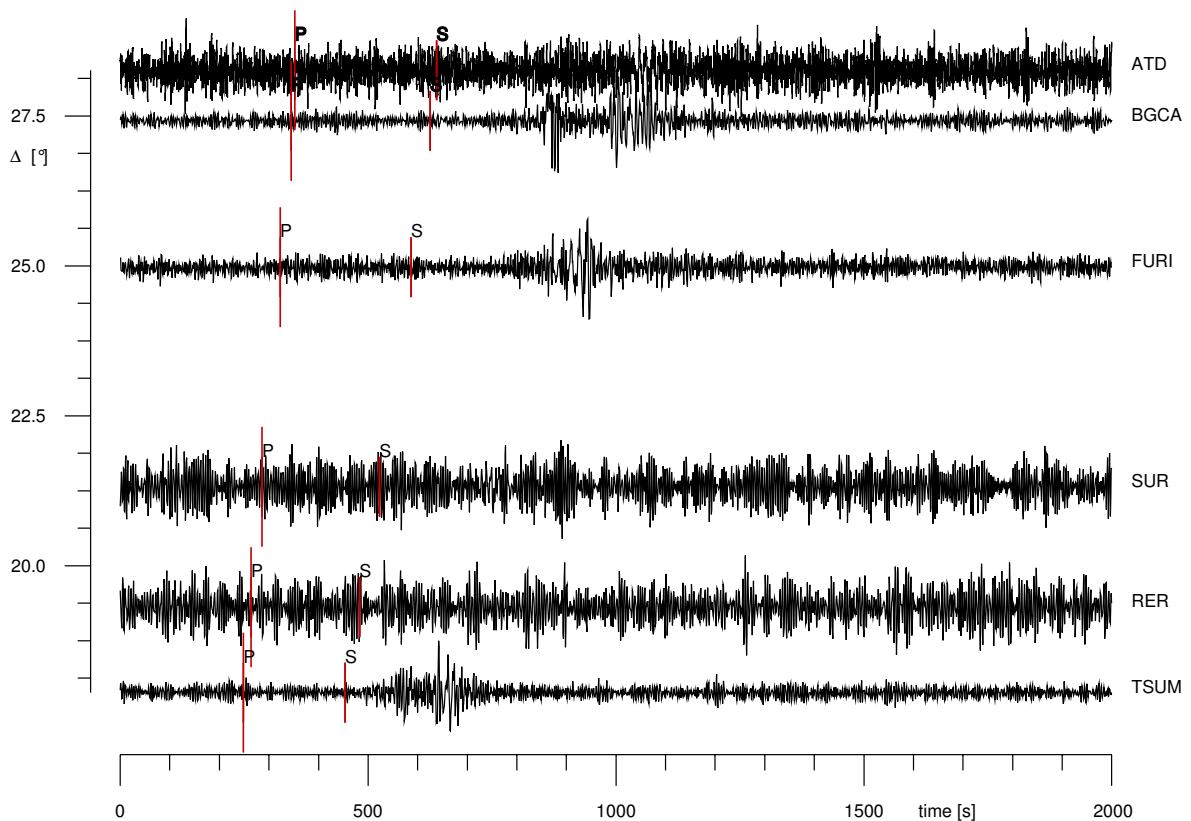


Figure 4.2: Vertical waveform components recorded of the 2000-01-04 earthquake (event 20). Data are corrected for the instrument response and sorted by source-receiver distance Δ . Theoretical P- and S-wave onsets are marked by vertical lines.

4.2 The 4 January 2000 M_W 4.8 earthquake

A representative earthquake to explain the inversion result plots and to demonstrate the three steps of the processing scheme is event number 20 that occurred on 4 January 2000 on the southernmost part of the East African Rift in Mozambique.

The event has been recorded by six of the 13 seismometers in and around eastern Africa with source-receiver distances between 2000–3100 km (section 3.1). Waveforms of the vertical seismometer components are shown in Figure 4.2. During STEP 1 of the processing scheme the individual waveform components are inverted solely to analyse whether they are explainable by an arbitrary source mechanism at all. Whereas stations SUR, TSUM and BGCA provide a good signal-to-noise ratio for all seismometer components and thus the inversion results in variances below the limits defined in section 3.2 ($\sigma \leq 0.5$ for single waveform components and $\sigma \leq 0.75$ for inversions of (Z,R) and (Z,R,T) , respectively), the horizontal components of station FURI show high variances when inverted for an individual moment tensor. Station ATD, is located in the Afar region that is $28^\circ = 3100$ km north

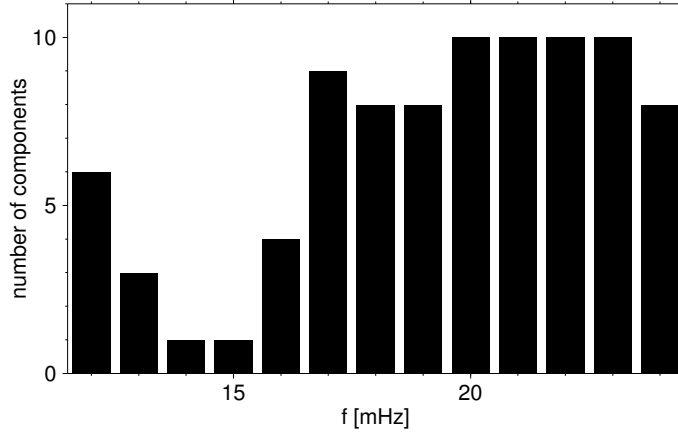


Figure 4.3: Histogram of the individual moment tensor inversion for single waveform components of event 20 (STEP 1 of processing scheme). Heights of bars indicate the number of waveform components $\Sigma [N_{init}(F_f)]$ that fulfil the variance criteria. Displayed frequencies correspond to the mid-frequencies of inverted 8 mHz wide frequency bands.

of the earthquake source and provides only a low signal-to-noise ratio due to the large source-receiver distance. In spite of its relative vicinity, station RER also shows a high noise level that is observed for other events as well (see section 5.3).

Figure 4.3 displays the statistics of STEP 1 of the processing. For the studied frequency range from 8 mHz to 29 mHz, the number of waveforms $\Sigma [N_{init}(F_f)]$ that can be well explained by an arbitrary moment tensor is highest for the 8 mHz wide frequency bands with mid-frequencies $f = 20\text{--}24$ mHz. Equally to higher and to lower frequencies the number of well explained waveforms decreases. Hence within STEP 1 of the processing N_{init} is determined to the dataset including the maximum number of ten waveform components: SUR(Z, R, T), TSUM(Z, R, T), BGCA(Z, R, T) and FURI(Z). The frequency range for which $\Sigma [N_{init}(F_f)]$ is maximum ($f = 20\text{--}24$ mHz), is extended to pass-bands for that the number of waveforms is still high. Thus the initial frequency range that is used for STEP 2 is $F_{init} = 12\text{--}29$ mHz ($f = 16\text{--}25$ mHz).

Figure 4.4a shows the beginning status of processing STEP 2 by inverting the automatically chosen waveforms N_{init} for a common moment tensor. The inversion for sliding frequency pass-bands and discrete source depths results in a broad depth-frequency region of similar normal faulting mechanisms. The obviously high variance level, however, is caused by traces that cannot be explained by a common source process. When inverted solely they are explained by an individual moment tensor. But since these data do not agree with the data of other traces, large variances are produced when all waveform components are inverted together for a common moment tensor. Hence, during processing STEP 1 non-source effects, such as crustal heterogeneities, are mapped into the moment tensor when these traces are inverted. Excluding these waveforms from the inversion in STEP 2 reduces the dataset to a consistent waveform data base. Since for each depth-frequency pair this

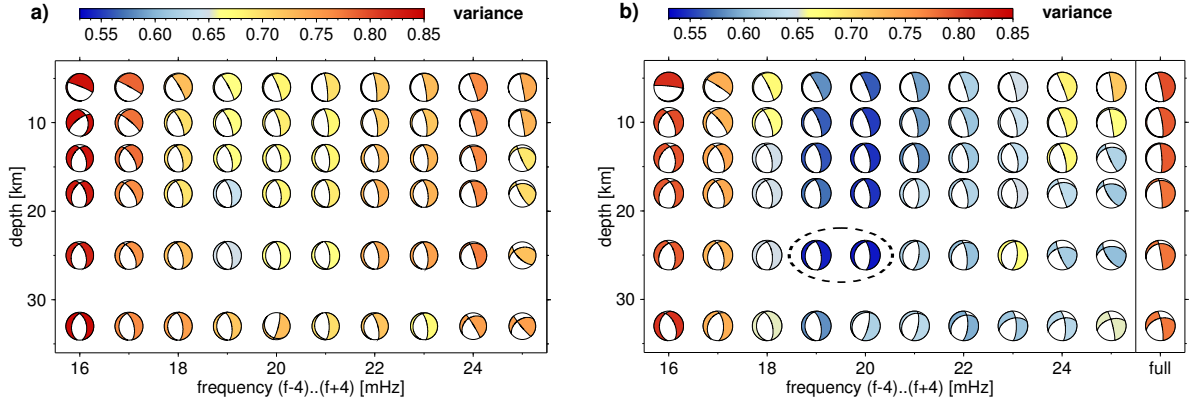


Figure 4.4: Frequency sensitive moment tensor inversion for 8 mHz wide pass-bands and discrete hypocentral depths for event 20. a) Inversion of the initial dataset N_{init} (STEP 2). b) Inversion of the final dataset N_{final} (STEP 3A) with d^* and F_{final} framed by the dashed line; the right column gives the inversion results for N_{final} and the full frequency range from 10–29 mHz.

dataset reduction is performed separately, the number of included waveform components differs. In this example the minimum value for the normalised variance σ_{norm} is given for the frequency pass-band $f = 16\text{--}24$ mHz and the final dataset N_{final} contains eight waveform traces: SUR(Z, R, T), TSUM(Z, R), BGCA(R, T) and FURI(Z).

The frequency sensitive inversion of N_{final} for discrete source depths (STEP 3A) is given in Figure 4.4b. Like for STEP 2 the inversion is performed for the frequency range $F_{init} = 12\text{--}29$ mHz and shows similar focal mechanisms compared to the inversion of the initial dataset N_{init} (Fig. 4.4a) but at a lower variance level. The depth-frequency combination with lowest variance is found at $f^* = 20$ mHz for a source depth $d^* = 25$ km with a variance $\sigma = 0.60$. Though the focal mechanism remains stable for a wide range of frequency, the variance σ decreases to both sides of the evaluated frequency range. Since $|\Delta Ax| < 30^\circ$ for f^* and $f = 19$ mHz and variances of all waveforms included are below 0.9, the final frequency band is extended to $F_{final} = 15\text{--}24$ mHz.

To analyse the frequency dependence of the inversion, for each event the dataset N_{final} is inverted for the full frequency band from 10 mHz to 29 mHz (Fig. 4.4b, right column) to see whether a frequency sensitive inversion is necessary. Compared to the stable, low variance depth-frequency region inverted for the narrow frequency bands, variances σ are high and focal mechanisms are partly rotated (section 5.3).

To estimate the optimum hypocentral depth, finally the moment tensor inversion for the frequency range F_{final} is performed for varying source depths (STEP 3B). The minimum variance σ results for a hypocentral depth at 25 km with similarly low variances for shallower depths, while deeper origins can be excluded (Fig. 4.5). Hence the mechanism is stable over varying source depths, but the hypocentral depths are constraint only little. The double couple percentage is above 70% for all source depths and gives a further indi-

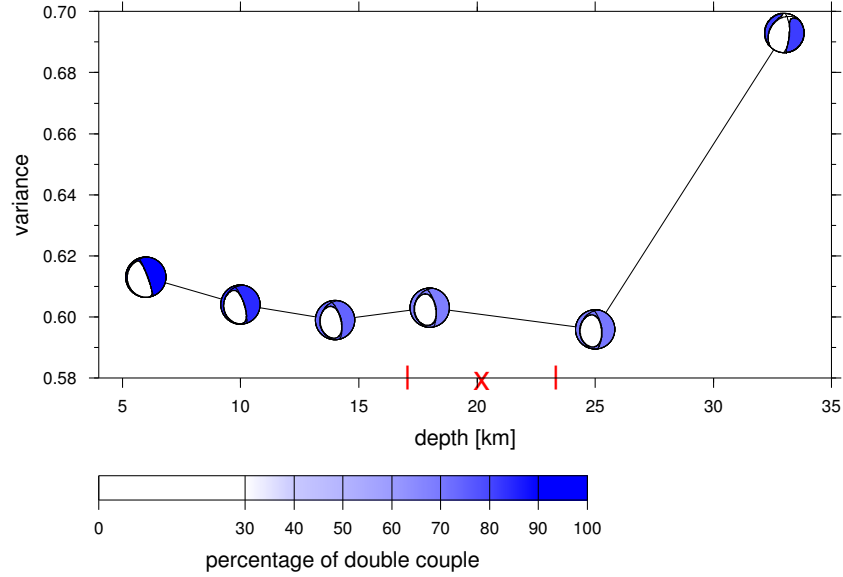


Figure 4.5: Variance σ of focal mechanism solutions in dependence on hypocentral depth for event 20. Inverted frequency range is $F_{final} = 15\text{--}24$ mHz for the dataset N_{final} . Blue colour indicates the percentage of double couple p . The red cross marks the depth determination of the Engdahl catalogue with standard deviation (red lines, Engdahl et al., 1998).

cation for a reliable solution (see sections 5.1 and 5.4). In Figure 4.6 the detailed inversion result for the optimum source depth of 25 km is presented. Finally, eight waveform traces of four seismic stations with source-receiver distances between 2000 km and 3000 km are used to determine the moment tensor. The solution shows a normal faulting mechanism, striking in north/south orientation. The nodal planes dip with 26° and 65° , respectively. The mechanism agrees with Harvard *CMT*-solutions determined previously for Mozambique (compare Fig. 3.1). The seismic moment is determined to $1.67 \cdot 10^{16}$ Nm that corresponds to $M_W = 4.8$. Surface wave-trains on both radial and transverse components are fitted very well in phase in amplitude. The summarised results of event 20 are shown in Appendix B.

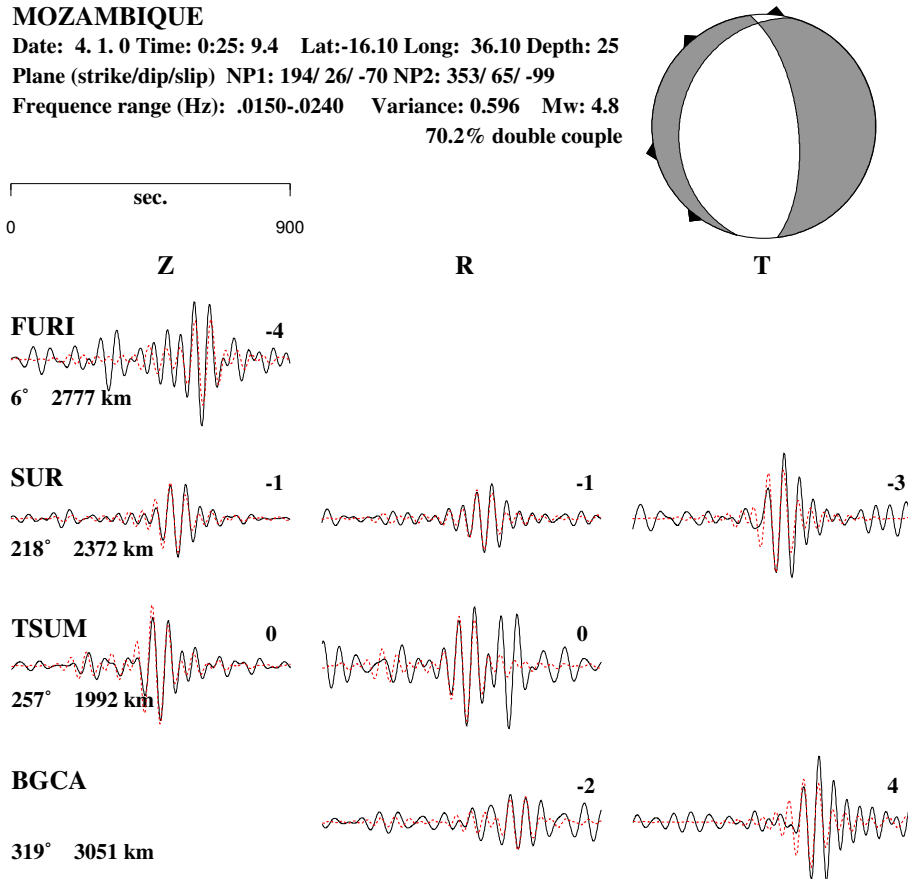


Figure 4.6: Final solution of the moment tensor inversion of event 20 calculated for the frequency range F_{final} . Triangles around the focal mechanism indicate station azimuth. The inverted waveform traces N_{final} on the vertical, radial and transversal component (Z, R, T) are plotted as black solid lines, synthetics as red dashed lines (including a 5% cosine taper on both sides). Station name and time-shift Δt is given above each trace, azimuth and epicentral distance below. Amplitudes are plotted normalised to the maximum of each station.

Chapter 5

Discussion

5.1 Statistical overview

Different parameters can give insights into the individual moment tensors inversions. Beside fixed input parameters as earthquake location and time, the inversion results depend on variable parameters studied in this work. These are determined by the semi-automatic procedure described in section 3.2: the waveform dataset, frequency pass-band and hypocentral depth. By studying their relation to output parameters as earthquake magnitude, data variance σ (eqn. 2.38) and percentage of double couple p (eqn. 2.34), reliability and quality of the moment tensor inversion results can be estimated. In the first section of this chapter dependencies on these variables will be studied and afterwards special features will be discussed.

The misfit between observed and calculated data in the frequency domain is given by the variance σ (eqn. 2.38), that is the parameter the moment tensor inversion minimises for. The average variance for the 38 moment tensor inversions is $\bar{\sigma} = 0.41 \pm .12$ with $0.17 < \sigma < 0.71$ normalised to the observed frequency amplitudes. Thus the determined solutions provide a good fit between observed and synthetic seismograms (Bernardi et al., 2004, compare Figures in Appendix B). For the main part of the results variance σ increases with decreasing earthquake magnitude (Fig. 5.1a), since for weak events the amplitude of the seismic signals can be as low as the seismic noise level, hence biasing the transient wave signal. Comparison of the variance-magnitude relation with the study of Bernardi et al. (2004), who used the same basic inversion code from Giardini (1992) but a different data processing, shows a very similar trade-off. Since they focused on the Mediterranean area using European permanent seismometers, for their study source-receiver distances were mostly around 1500 km. In this study source-receiver distances are on average 2000 km with maximum distances up to 3300 km. Although source-receiver distances are larger and seismic station coverage is less dense in Africa than in Europe, the variances in this study are as low as those obtained by Bernardi et al. (2004). The generally low level of σ resulting

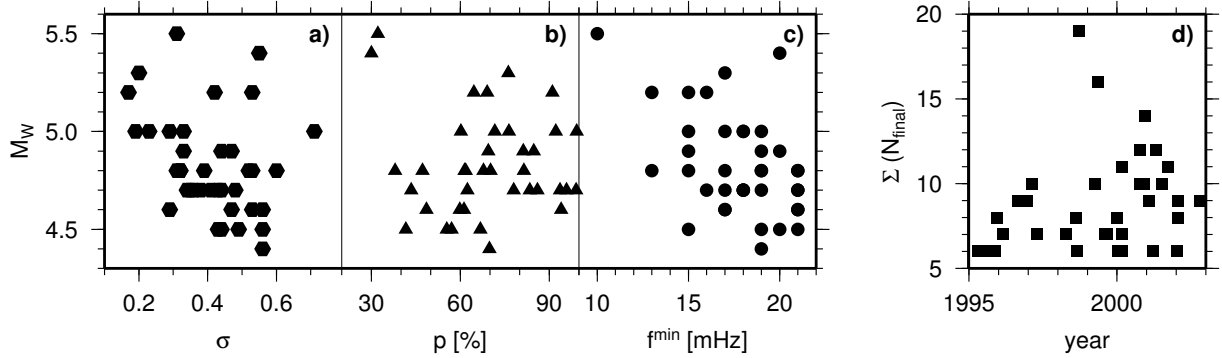


Figure 5.1: Statistical summary of the 38 moment tensor inversions showing the dependencies of the different parameters. Moment magnitude M_W vs. a) variance σ , b) double couple percentage p , c) high-pass frequency $f_{\text{final}}^{\text{min}}$ and d) number of waveforms $\Sigma(N_{\text{final}})$ vs. date of occurrence.

from the presented frequency sensitive inversion is obtained by systematically excluding waveform components with variances higher than 0.75 by STEP 2 of the semi-automatic processing (Fig. 3.3). In combination with the frequency sensitive analysis this allows the determination of source mechanisms for magnitudes as low as M_W 4.4 and thereby the decrement of the magnitude threshold of moment tensor inversion for eastern Africa, previously defined by Harvard *CMT*-solutions (section 5.5).

Non-double couple parts of a moment tensor can be caused by various effects (Frohlich, 1994). Beside physical reasons such as complex source geometries consisting of two or more subevents on non-parallel faults (Frohlich, 1995), non-*DC*-components can be due to mismodelled seismic noise and crustal heterogeneities (Kuge and Lay, 1994; Henry et al., 2002). Source mechanisms of low magnitude earthquakes are generally thought to have rather simple source geometries, that can be described by a pure double couple mechanism. However, complex rupture mechanisms of low magnitude events are reported as well (Ide, 2001). Thus one must be aware of large non-*DC*-parts, that can be a hint for mismodelled random noise or crustal heterogeneities mapped systematically into the source process, when inverting low magnitude events for the moment tensor, using little data and a one-dimensional velocity model. Since in this work and most other inversion routines p is not a parameter that is optimised during inversion, it has not a high value per se.

In this study the *DC*-percentage p (eqn. 2.34) of inverted moment tensors shows a general increasing trend for increasing magnitude M_W (Fig. 5.1b). Especially inversions of earthquakes $M_W \leq 4.6$ have small *DC*-parts with average $\bar{p}(M_W \leq 4.6) = 61\%$ compared to the over-all average of $\bar{p} = 69\%$. In contrary, higher magnitude events $M_W \geq 4.9$ show higher *DC*-parts, except of two events with rather low p but high magnitudes (events 2 and 8), discussed in section 5.4. Obviously the low magnitude moment tensors constrained by little or noisy data tend to have relatively low *DC*-percentages, supporting the results published by Kuge and Lay (1994). However, Jost and Hermann (1989) showed by synthetic tests

that increasing the level of random noise decreases the percentage of double-couple p of a moment tensor, but that the DC -part (and hence the shape of the focal mechanism) is affected only little. In this work waveform traces with low signal-to-noise ratio as well as traces inconsistent with other waveform data are excluded by the automatic choice of the final dataset N_{final} . So most of the traces affected by high random seismic noise, are excluded during STEP 1, while STEP 2 reduces the dataset to traces not affected by structural heterogeneities.

In section 5.4 will be shown by singular value decomposition that both, random seismic noise and inconsistent data resulting from crustal heterogeneities may be present in the data, but that the double couple parts are hardly affected.

Figure 5.1c shows the relation between inverted frequency band and moment magnitude M_W . It shows that the high-pass frequency f_{final}^{min} of F_{final} is lower for higher magnitudes. Similar to the relation obtained by Šílený (2004), moment tensors for M_W 5.2 events can be inverted from frequencies as low as 13 mHz ($\mathcal{T} \leq 77$ s), while for low magnitude earthquakes $M_W \leq 4.5$ only higher frequencies $f_{final}^{min} \geq 18$ mHz ($\mathcal{T} \leq 56$ s) are usable. As described by previous works, there is a clear trade-off between earthquake magnitude and the frequency range providing a sufficient signal-to-noise ratio (Braunmiller et al., 2002). However, some earthquakes do not follow this trend, probably since the combination of low signal-to-noise ratio and unexplained crustal heterogeneities overlay the theoretical frequency dependence (Kafka and Weidner, 1979).

The average number of inverted waveform traces per earthquake $\bar{\Sigma}(N_{final})$ is nine and ranges from the predefined minimum of six to a maximum of 19 waveforms for event number 15 (M_W 5.0). Since 1995 data availability has been improved, and thus moment tensors of events recorded at later times are generally determined by more waveforms than earlier ones (Fig. 5.1d). Thus, for events that occurred in the first years of the study period often only six to eight waveform components provide consistent data.

Inverting less than six waveforms, the small amount of data can be fitted by various mechanisms, for structural heterogeneities could wrongly be mapped into the source process (Kim and Kraeva, 1999; Rao et al., 2002). This can lead to rotated beach balls when the frequency band is varied little, with small depth-frequency regions of stable focal mechanisms. Thus only earthquakes that provide a good signal-to-noise ratio for a sufficient amount of data are analysed. Since inversions for only six to eight waveforms do not result systematically in high variances the limit of $\Sigma(N_{final}) \geq 6$ is an adequate restriction.

5.2 Individual moment tensor solutions

5.2.1 The 2 October 2000 M_W 6.4 earthquake

During the period of investigation one strong M_W 6.4 earthquake occurred on the western branch of the East African Rift at the southern end of Lake Tanganyika (8.0°S/30.8°E)

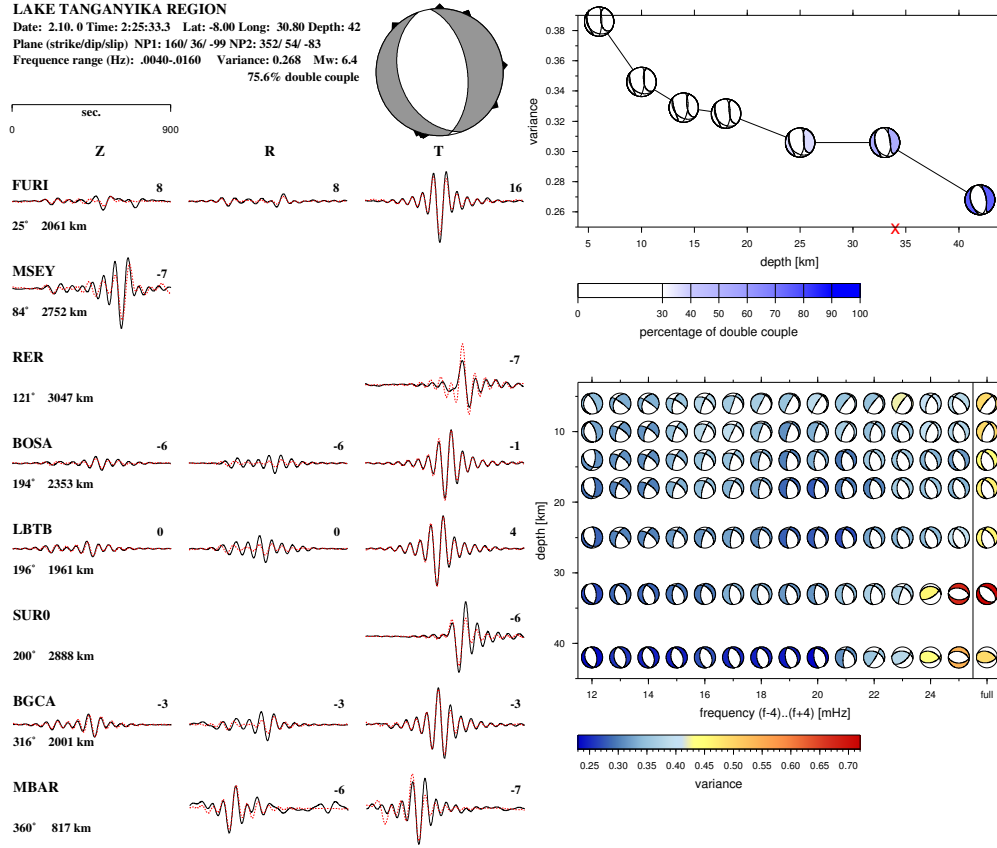


Figure 5.2: Moment tensor inversion for the 2000-10-02 earthquake. On the lower right: frequency sensitive inversion of the final dataset N_{final} (STEP 3A). Upper right: depth-variance analysis for N_{final} and the final frequency band F_{final} (STEP 3B). Left side: final result of the moment tensor inversion. Detailed description see Figures 4.4–4.6.

on 2 October 2000, 02:25:33.3 UTC (Engdahl catalogue of relocated earthquakes, Engdahl et al., 1998). Routinely, the moment tensor of the event was determined by Harvard-CMT (Dziewonski et al., 2003) and the United States Geological Survey (USGS, available online via <http://neic.usgs.gov/neis/sopar>). As a test of the frequency sensitive procedure, the moment tensor for this event is calculated to compare the inversion result to published focal mechanisms. The event is determined to have a normal faulting mechanism, striking north-northwest/south-southeast (Fig. 5.2). 17 waveform components are chosen automatically to invert for the moment tensor (N_{final} , STEP 2). The depth-frequency dependencies calculated in STEP 3A of the inversion procedure (section 3.2) show a clear picture of stable focal mechanism results over almost the whole range of frequencies (Fig. 5.2). Only on the high-frequency edge for hypocentral depths of 33 km and 42 km, low variance mechanisms are calculated that are rotated relative to the lower frequency inversions. This effect is observed for other events as well and will be discussed in section 5.3. The final inversion

Table 5.1: Focal mechanism solutions for the 2000-10-02 Lake Tanganyika event.

| Ref | hr:min:s | Lat | Lon | D | M_W | Str | Dip | Ra | Σ_S | Σ_b | p |
|-------------------------|------------|------|------|----|-------|-----|-----|------|------------|------------|------|
| <i>CMT</i> | 02:25:38.4 | -7.8 | 30.6 | 40 | 6.4 | 346 | 58 | -93 | 59 | 144 | 93.4 |
| <i>USGS</i> | 02:25:31.3 | -8.0 | 30.7 | 36 | 6.4 | 342 | 57 | -112 | 26 | - | 97.0 |
| this study ¹ | 02:25:33.3 | -8.0 | 30.8 | 42 | 6.4 | 352 | 54 | -83 | 8 | 17 | 75.6 |

Columns as follows: reference, rupture time, latitude, longitude, depth [km], moment magnitude, strike, dip, rake, number of stations Σ_S , number of waveform traces inverted Σ_b , percentage of double couple p .

results in a focal mechanism that has one nodal plane striking 352° , dipping 54° with a slip of -83° . The minimum variance source depth is 42 km, that is also the depth with maximum double couple percentage $p = 75.6\%$. To shallower depths variance increases and p decreases.

The obtained moment tensor differs only slightly from the solutions given by Harvard-*CMT* (Dziewonski et al., 2003, see Table 5.1 and Fig. 5.3) and the determination of the *USGS* (Sipkin et al., 2002). The centroid time given by the *CMT*-solution is 5 s later and the calculated centroid location is approximately 30 km northeast of the hypocentre relocated by Engdahl. This relatively large deviation must be seen in the context of the fault dimensions of an M_W 6.4 event that are e.g. 40 cm slip on a 10 km wide and 40 km long rupture area. In contrary a M_W 4.4 event, two scales of magnitude lower, has an energy release smaller by a factor of about one thousand and thus the fault dimensions are e.g. 4 cm slip on a fault 1 km \times 4 km (accordingly 13 cm \times 3 km \times 13 km for M_W 5.4).

Hence, the possible difference between centroid location and hypocentre is restricted to the fault dimensions and be compensated by time-shifts Δt (compare section 3.2). Long wave periods for a M_W 6.4 earthquake are above the seismic noise level even at teleseismic distances. So for the 2000-10-02 earthquake the finally inverted frequency band $F_{final} = 4\text{--}16$ mHz is very low and the allowed time-shift $\Delta t \leq 16$ s is relatively high.

For light and intermediate magnitude events studied in this work frequencies are higher and maximum time-shifts Δt are clearly shorter. But since the position of the centroid is restricted to a rupture area of only a few kilometres length, the deviation to the source location determined by body-waves can be compensated as well.

It can be summarised that the limitation of Δt defined in equation 3.1 accounts for differences of centroid location and hypocentre and at the same time prevent from large, phase changing time-shifts. Moreover the presented procedure is able to reproduce known focal mechanism solutions of strong earthquakes, and it is appropriate to apply the method to low and intermediate magnitude events.

¹Rupture time and epicentre coordinates are taken from the Engdahl catalogue (Engdahl et al., 1998).

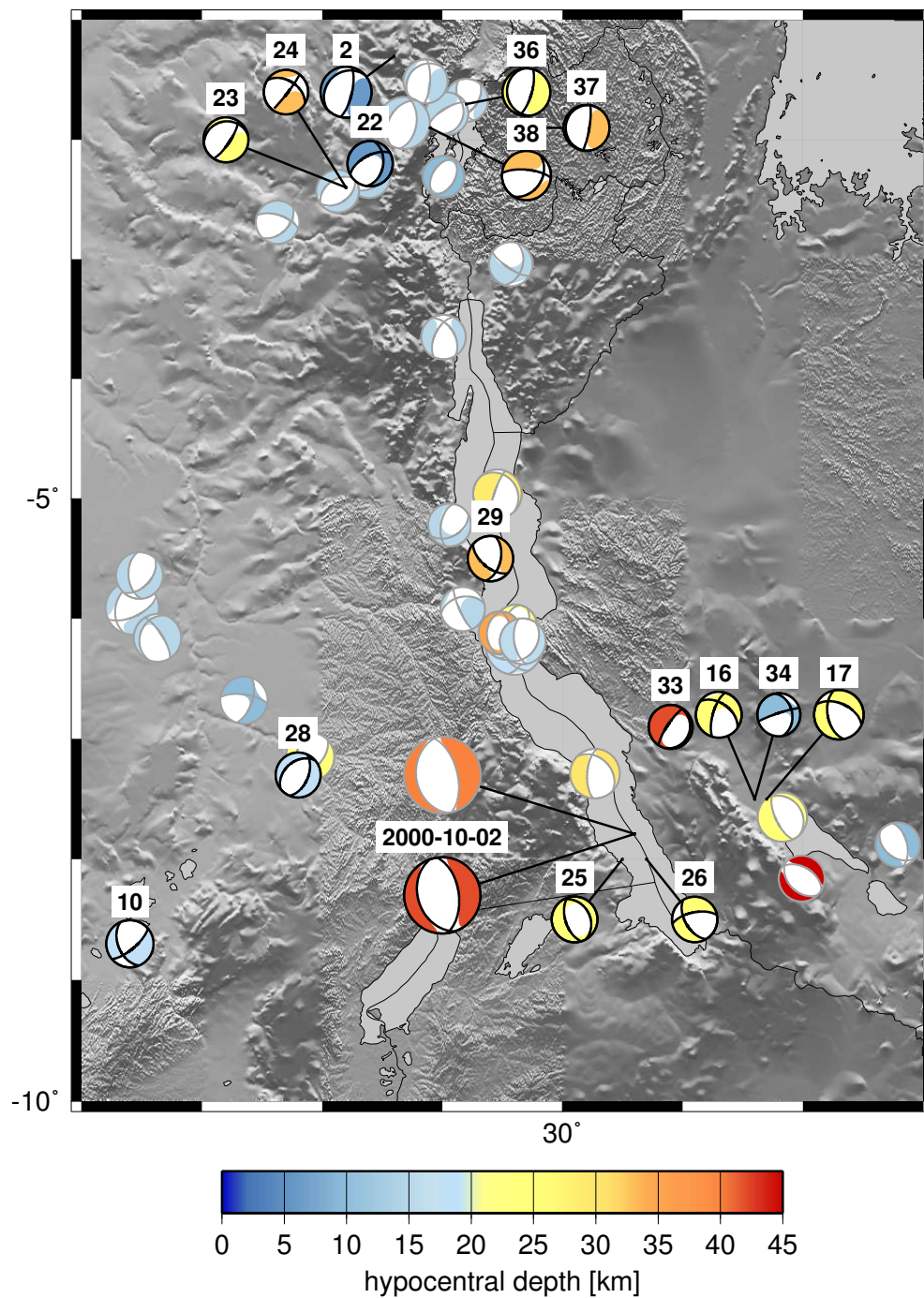


Figure 5.3: Hypocentral depths of focal mechanism solutions in the Lake Tanganyika region. Colour indicates source depth and diameter scales with magnitude. The numbered focal mechanisms with black lined nodal planes are determined in this work (1994–2002); Harvard *CMT*-solutions have grey lined nodal planes (1977–2005). The two focal mechanisms of the M_W 6.4 event on 2000-10-02 calculated in this work and by Harvard-*CMT* are displayed enlarged.

5.2.2 Seismicity beneath the upper crust

The relatively great hypocentral depth of the 2000-10-02 earthquake ($d_{final} = 42$ km) estimated in this work agrees with the centroid-depths provided by *CMT* (40 km) and *USGS* (36 km). This is also supported by body-waveform modelling using frequencies $\mathcal{T} \approx 5\text{--}10$ s (41 km depth, Ruff, 2004). Since the seismogenic zone of continental settings is discussed to be between 15 km and 25 km depth (e.g. Stein and Wysession, 2003), the 2 October 2000 event violates the hypothesis that non-subduction seismicity is restricted to the upper crust. Previous works already observed seismic activity beneath the upper crust for various eastern African earthquakes (e.g. Foster and Jackson, 1998; Fairhead and Girdler, 1971; Shudofsky, 1985), indicating that in eastern Africa the seismic active zone reaches into the lower crust (Nyblade and Langston, 1995). In this work for ten events hypocentres are estimated to be as deep as 33 km or even 42 km (event number 33). Figure 5.3 shows focal mechanism solutions for the Lake Tanganyika region determined in this work and by Harvard-*CMT* in dependence of their source depths. All along the Lake Tanganyika deep sources are observed and especially on the southern Lake Tanganyika three events sources deeper than 40 km: the 2000-10-02 M_W 6.4 event discussed in the previous paragraph, event number 33 calculated in this work and an additional *CMT*-solution at 8.2°S/32.0°E (2002-02-20, M_W 5.5, Table A.2). Ruff (2004) proposes three possible explanations for deep events in eastern Africa: 1) The temperature at 40 km depth is lower than expected by the normal crustal geotherm and the lower crust can still behave brittle. 2) The events take place just below the Moho, since the mantle material can break at much higher temperatures, or 3) earthquakes are possible at high crustal temperatures as well.

5.2.3 Aftershocks and earthquake sequences

During the study period of this work six earthquake sequences occurred. Two of them can be clearly identified as series of main- and aftershocks, while the events of the other four earthquake sequences do not show any dominant initial rupture. Location and date of these series are given in Table A.3 and started on 1996-12-20, 1999-05-07, 2000-03-02, 2000-10-02, 2002-01-17 and 2002-10-24, respectively.

The Lake Tanganyika M_W 6.4 earthquake on 2000-10-02 (paragraph 5.2.1) was followed by an aftershock series. Four aftershocks were reported by the International Seismological Centre (*ISC*) with two events m_b 4.3 and m_b 4.2 on the same day. Only the two later and stronger ones were reported in the Engdahl catalogue that occurred nearly four and five days after the mainshock with magnitudes of M_W 4.8 and M_W 4.7, respectively, and are analysed in this work (Fig. 5.3, events number 25 and 26). Their relative location is within 20 km to the centroid location and assuming an location error of some kilometres, principally both aftershocks can be located on the main rupture area (compare paragraph 5.2.1). Both aftershocks have source depths shallower than the mainshock location. Event 25 has a well defined variance minimum at 25 km depth that agrees with the Engdahl relocation. In contrary, depth resolution of the second aftershock is low, since variances for four

out of six solutions lie within a narrow corridor of $\Delta\sigma = 0.02$ (event #26, Appendix B, p. 124). Thus the finally chosen source depth is 25 km, because of the high double couple percentage and the vicinity to the hypocentral depth determined in the Engdahl catalogue. The three focal mechanism solutions have one nodal plane in common, striking within 23° roughly north-northwest/south-southeast. Since this approximately is the orientation of the East African Rift System (*EARS*) which coincides with the orientation of the Lake Tanganyika, it is likely that the common nodal plane of main- and aftershocks was the actual fault plane. The mainshock and the first aftershock, both show normal faulting on the assumed east-southeastern dipping fault plane. However, event 26 is a left lateral oblique slip mechanism and probably a consequence of reducing residual local stresses of the mainshock that released around 350 times the energy of the M_W 4.7 aftershock.

The other aftershock analysed occurred on 2002-10-24 (M_W 5.2, event 38) only one hour after the M_W 6.2 mainshock. Additionally, the Engdahl catalogue contains two more events for that the inversion procedure determined less than six usable waveforms (*ISC*: six aftershocks $m_b \geq 3.5$). The events are located north of Lake Tanganyika and the moment tensor of the mainshock was routinely determined by Harvard-*CMT* (Ekström et al., 2005, Fig. 5.3). If location and inversion uncertainties are neglected, both events have one nodal plane in common that coincides with the orientation of the main fault system and strikes north-northeast/south-southwest and dips with 40° – 50° . As the 2000-10-02 event, the mainshock is a normal faulting mechanism at 15 km depth, while the aftershock shows a right lateral strike-slip mechanism with a minor dip component at a low resolved depth at 33 km (event #38, Appendix B, p. 130).

The same region was the location of an earthquake sequence in January 2002 with no main shock present (*ISC*: 18 events $m_b \geq 3.8$, 2002-01-17 and 2002-01-22). Five events were strong enough to be inverted for the moment tensor. Focal mechanisms of the later three events were determined by Harvard-*CMT* (Ekström et al., 2005), the first two in this work (events 36 and 37). These two and the last event (*CMT*-solution) show similarly normal faulting mechanisms striking with north-northeastern orientation with a steep dipping nodal plane of 70° – 80° in common. The second and third event, however, show also normal faulting but nodal planes striking with rotated orientations. Nevertheless, the preferred orientation is north-northeast, parallel to the *EARS*.

A very similar combination of earthquakes occurred in March 2000 only 80 km southwest beneath the western rift shoulder. Three events were reported by both *ISC* and Engdahl catalogue and none was calculated by Harvard-*CMT*. Events number 22–24 occurred within two days and while the last two events had one steep nodal plane in common (M_W 4.7, M_W 4.6) striking northeast, the first event is a normal faulting mechanism oriented north-east/southwest but without a similar nodal plane.

Events number 16 and 17 occurred 12 hours after each other on 1999-05-07 and were localised beneath the eastern shoulder of the southern Lake Tanganyika. They show a very similar normal faulting mechanism with a dipping component. Strike of the nearly identical fault planes is 305° and 294° , dipping 48° and 52° , respectively. The magnitude of

the first event is M_W 4.8, while the larger one occurred thereafter with M_W 5.2. Since the fault planes are particularly similar a triggering of rupture events seems to be probable.

The only earthquake series that was recorded between 1994–2002 on the eastern rift branch started on 1996-12-20. Four events were reported by *ISC*, two of which are also contained in the Engdahl catalogue and for the smaller M_W 5.1 event a *CMT*-solution was calculated. The larger shock of M_W 5.5 that occurred 29 hours later, is determined in this work. Actually, both mechanisms show a similar mostly right lateral strike-slip mechanism with some dip-slip component with similarly striking nodal planes; however, the dipping angles differ strongly. Both solutions have been determined by nine waveforms and the automatic, frequency sensitive inversion procedure chooses a frequency band $F_{final} = 10\text{--}22$ mHz nearly identical to the *CMT* default value ($\mathcal{T} \geq 45$ s, $f \leq 22.2$ mHz). The very low double couple percentage $p_{\#8} = 32.2\%$ of event 8 and the moderate one of the *CMT*-solution $p_{cmt} = 66.2\%$ could be a hint for mismodelled portions in the focal mechanisms. However, in section 5.4 it will be shown that $p_{\#8}$ can be increased significantly by the *SVD*-cut-off inversion without changing the double couple part severely.

5.2.4 Thrust faulting events

The major part of the analysed earthquake sources are normal faulting mechanisms that are distributed over the whole study region and agree with the general extensional regime in eastern Africa (Coblentz and Sandiford, 1994). Beside this, oblique dip-slip ruptures are observed in the rift itself (e.g. event number 30). This supports the idea of rift-related pull-apart basin as proposed by Skobelev (2004). Coblentz and Sandiford (1994) showed by modelling gravitational potential energy that compressional areas originated in the mid-ocean ridges surround Africa. Hence the thrust faulting events in the Mozambique Channel (event number 21) and the Indian Ocean (event number 6) could be understood as an expression of the potential gravitational energy. In western Africa thrust mechanisms have been described by Ayele (2002) and Suleiman et al. (1993), thus event number 18 (Angola) could be interpreted as an indicator for transition from extensional tectonics in the east to a compressional regime in the west of Africa.

5.3 Potential and restrictions of the frequency sensitive moment tensor inversion

The frequency sensitive moment tensor inversion is performed to determine focal mechanism solutions in regions, where intermediate seismicity is present but only sparse seismic data are available. In this study the one-dimensional velocity model PREM (Dziewonski and Anderson, 1981) is used for normal mode summation, to analyse the global applicability of the developed procedure. Dziewonski and Anderson (1981) used around 1000 normal

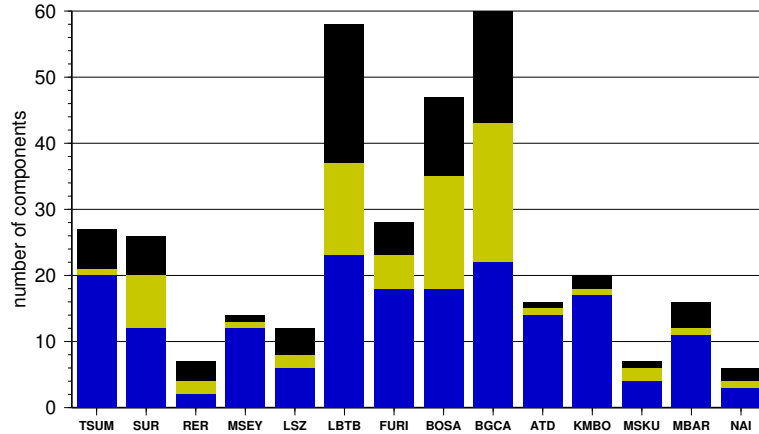


Figure 5.4: Cumulative number of waveform components used for moment tensor inversion. Bars represent seismic stations. Stations on the right side were not operating the whole study period from 1995–2002 (KMBO: 7 years, MSKU: 4 years, MBAR: 3 years, NAI: 1 year, others: 8 years). Blue colour indicates vertical Z component, yellow and black the horizontal components R and T , respectively.

mode periods and 500 summed travel time observations to calculate the one-dimensional PREM velocity model. These average velocities cannot account for regional features and thus some waveform information cannot be explained. However, Rayleigh- and Love-waves of periods $\mathcal{T} = 35$ s are sensitive down to depths of ~ 70 km and ~ 35 km, respectively (Dahlen and Tromp, 1998) and thus an individual one-dimensional velocity model for eastern Africa would probably explain shorter period waveform data slightly better. In this study $\mathcal{T} \geq 35$ s proved to be sufficient for determining stable moment tensor inversions, as shown before by Šílený (2004).

The restriction of seismic data to periods $\mathcal{T} = 35$ –100 s (compare section 3.1) limits the number of waveform components that was used for moment tensor inversion (Fig. 5.4). Larson and Ekström (2001) showed that both, Love- and Rayleigh-waves, are affected by crustal and lithospheric structure, depending on their period. Thus the velocity of surface waves depends on whether they travel through continental or oceanic lithosphere. For eastern Africa and the Indian Ocean, the Love-wave velocity difference is between 10–20% at periods of $\mathcal{T} = 40$ s ($f = 25$ mHz) in the uppermost 30 km of the earth. Thus if low frequency data are not sufficient for the inversion of very low magnitude events, surface-wave velocity models can be used as additional improvements to explain high frequency waves (Ekström et al., 1997). These ocean-land velocity perturbations are probably one reason why the oceanic island stations RER (located east of Madagascar on the island of Réunion) and MSEY (Seychelles) provide only few usable data, since the one-dimensional earth model does not consider velocity heterogeneities. The other reason is the relatively high seismic noise level that biases the data of oceanic stations (compare Fig. 4.2, Barruol and Ismail, 2001). Here the dominant noise factors are atmospheric perturbations, that

change the atmospheric pressure and thus induce seismic energy (Sorrells, 1971; Sorrells et al., 1971). The effects of oceanic storms, however, affect only short periods $\mathcal{T} < 10$ s. For these periods seismometers located within continents show a higher signal-to-noise ratio than those performed near the coastline or on oceanic islands. In contrast to continental stations far away from the oceans, here Rayleigh-waves excited by oceanic storms are hardly attenuated. So the coastal station ATD does provide long-period data with a high signal-to-noise ratio (vertical component), while the short-period waves are affected by oceanic disturbances. The very low signal quality of its horizontal components, however, was described previously and agrees with a generally higher noise level for horizontal components at periods $\mathcal{T} \geq 40$ s (Stutzmann et al., 2000). The stations that recorded the highest amount of data used in this work are LBTB, BOSA and BGCA. Especially their horizontal components provide excellent data, that can be included in the waveform datasets nearly as often as their vertical components.

To study the sensibility of the inversion result on hypocentral depth, data are inverted for the whole range of crustal source depths (STEP 3B). This reveals that some inversion results of this work have minor resolved hypocentral depths as reported before for long-period inversions (Giardini, 1992). Whereas some solutions show oscillating variance with varying depth (events numbers 3, 8, 23, 26), others have a clear variance minimum for a certain depth d_{final} , but with variances nearly as low as at neighbouring discrete depths (events numbers 5, 13, 15, 18, 19, 22, 27, 28, 29, 34). Both scenarios allow a depth estimation, however, but with decreased reliability. The remaining inversion results show rather clear variance minima for one source depth. Sometimes the source depth agrees very well with the hypocentre location given by the Engdahl catalogue (events 14, 15, 17, 18, 25, 27, 33, 35). For 27 of the inverted events an explicit hypocentral depth was calculated with an average error of 3.4 km, others are fixed at a depth of 15 km (Engdahl, personal communication, see Appendix B). These were calculated by the use of the depth phases pP, sP, PcP and pwP (reflection on the ocean's surface), that have a high sensitivity for the hypocentral depth (Engdahl et al., 1998). In paragraph 5.2.1 it has been shown that the hypocentral depth determined by body waves does not need to be identical with the centroid depth. Nevertheless it is an appropriate starting value for STEP 1 as initial depth d_{init} . Finally, most of the events could be clearly attached to the crust. Some unusual deep events, however, are discussed in paragraph 5.2.2.

Normal mechanisms with one nodal plane nearly vertically dipping are determined for a few events. The tectonics behind these mechanism are poorly understood, but similar focal mechanisms has been determined by Harvard-CMT (e.g. 2002-01-21, 2002-01-22, compare Fig. 5.3, 2°S/29°E). The inversion results of these events are stable and varying slightly depth or frequency does not change the double couple pattern significantly.

The depth-frequency plots of STEP 3A show rotated mechanisms or at least high variances for high frequencies compared to the region of stable focal mechanisms for lower frequencies. This occurs mostly for events that are calculated for relatively low frequency pass-bands (events 08, 15, 17, 20, 28, 31, 35, 37, see figures in Appendix B and 2000-10-02, Fig. 5.2). However, this is not the case for moment tensors inverted of these high frequency waves.

The reason for that behaviour is the restriction of Δt to a quarter of the minimum inverted period (eqn. 3.1). Thus inverting lower frequencies (longer periods), higher time-shifts are allowed that are necessary to compensate traveltime residuals especially for larger events (see paragraph 5.2.1). Beside low signal-to-noise ratios, this is an additional explanation why inversions of the full frequency band (including high frequencies up to 29 mHz) tend to have low variances. Here the low frequency part may be dominating the inversion result, while the allowed time-shift Δt is calculated by the maximum frequency used.

Generally the time-shift Δt is an important parameter, since it improves the capability of the inversion to compensate travel time residuals that cannot be explained by a one-dimensional earth model. It is demonstrated in paragraph 5.2.1 that the limitation of Δt (eqn. 3.1) is adequate to take account of deviations in source location on the one hand and does not allow phase changing time-shifts on the other hand.

Since only teleseismic waveform data can be used to determine low magnitude source mechanisms in eastern Africa, for several events only little data are available. At least three to five permanent recording seismometers in distances less than 3300 km around the study area are inverted for each seismic moment tensor. Inverting less than six waveform components does not result in stable mechanisms, but leads to strong dependencies of the actual dataset, since inversions with only little data do not constrain the moment tensor for the one-dimensional earth model given.

Beside the limitation of time-shift (eqn. 3.1) and the restriction for the number of waveform components $\Sigma [N_{init}(F_f)] \geq 6$, the variance limits are the main criteria when composing the final dataset N_{final} for the inversion. The choice of $\sigma \leq 0.5$ for single inverted waveform components and $\sigma \leq 0.75$ for (Z,R) and (Z,R,T) (see section 3.2) is an adequate setting for this work, since hereby only inversions are allowed that provide a stable focal mechanism for a minimum of data.

The variance criteria are defined by empirical means to obtain stable inversion results. Since the choice of seismic data depends on the distribution of seismometers and magnitude range studies, these parameters have to be adapted when the procedure is transferred to other regions of the earth.

5.4 Singular value decomposition

The singular value decomposition (*SVD*) separates the moment tensor into its model eigenvectors (section 2.3). Since biased input data are mapped on the eigenvector with the lowest eigenvalue (Forbriger, 2001), it is worthwhile to study the decomposition for the case of low magnitude earthquakes and low amount of data, where biased data are present due to seismic noise and mismodelled structural heterogeneities. This will give insights in the stability of the solutions and the meaning of the double-couple percentage.

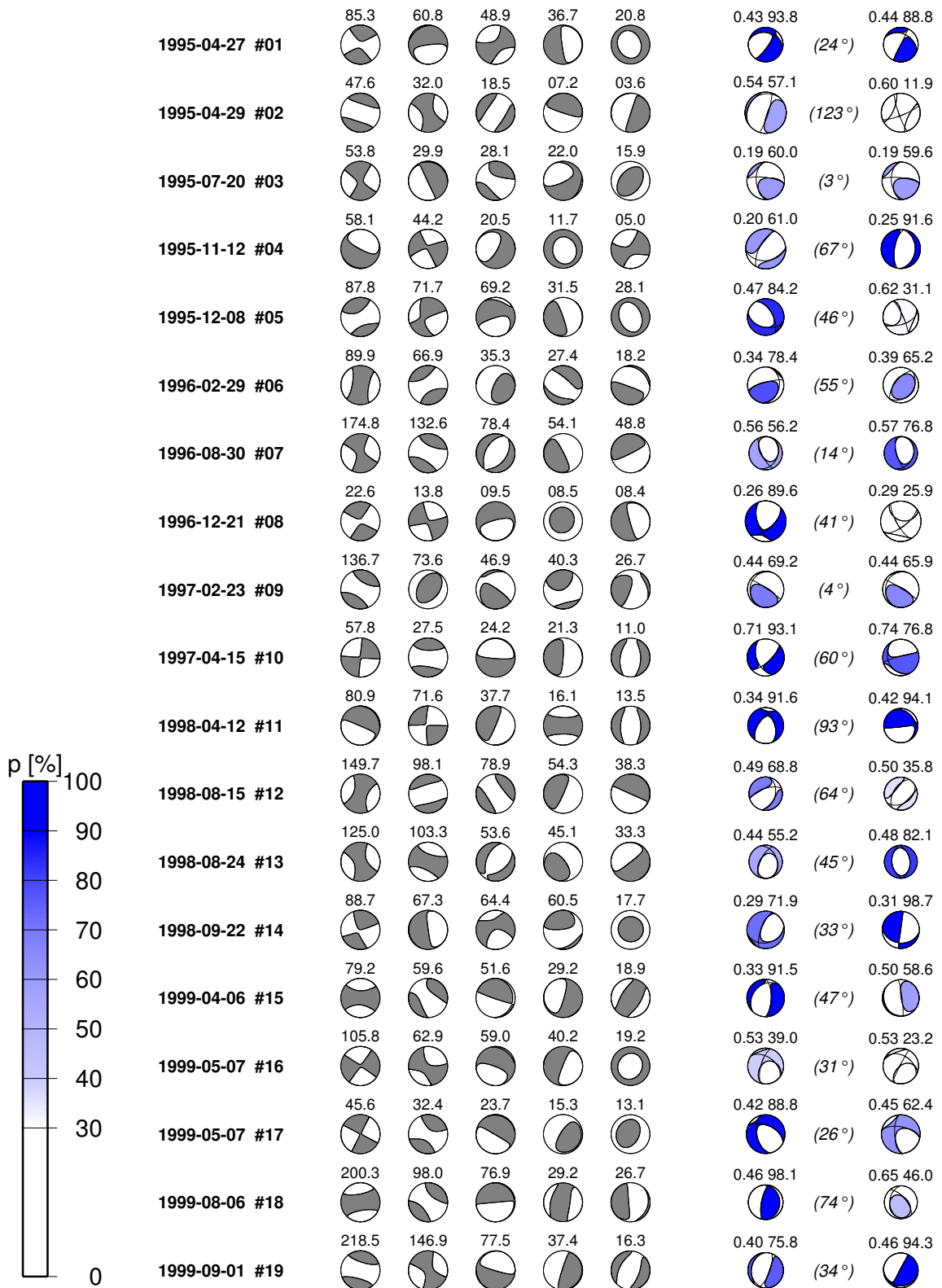
Figure 5.5 shows the *SVD* for the deviatoric moment tensors analysed in this work. Beside the five single eigenvectors and according eigenvalues, the result of the *SVD*-inversion is

shown—composed of all five eigenvectors (\mathbf{m}_{dev}) and the cut-off solution composed of only the four eigenvectors with largest eigenvalues ($\mathbf{m}_{cut,4}$), respectively (eqs. 2.42, 2.43). To study the pure consequences of reducing the inversion result by one eigenvector, the *SVD*-inversion is performed without any damping. Thus \mathbf{m}_{dev} is not exactly identical with the final solutions of the (damped) frequency sensitive moment tensor inversion presented in Appendix A and B.

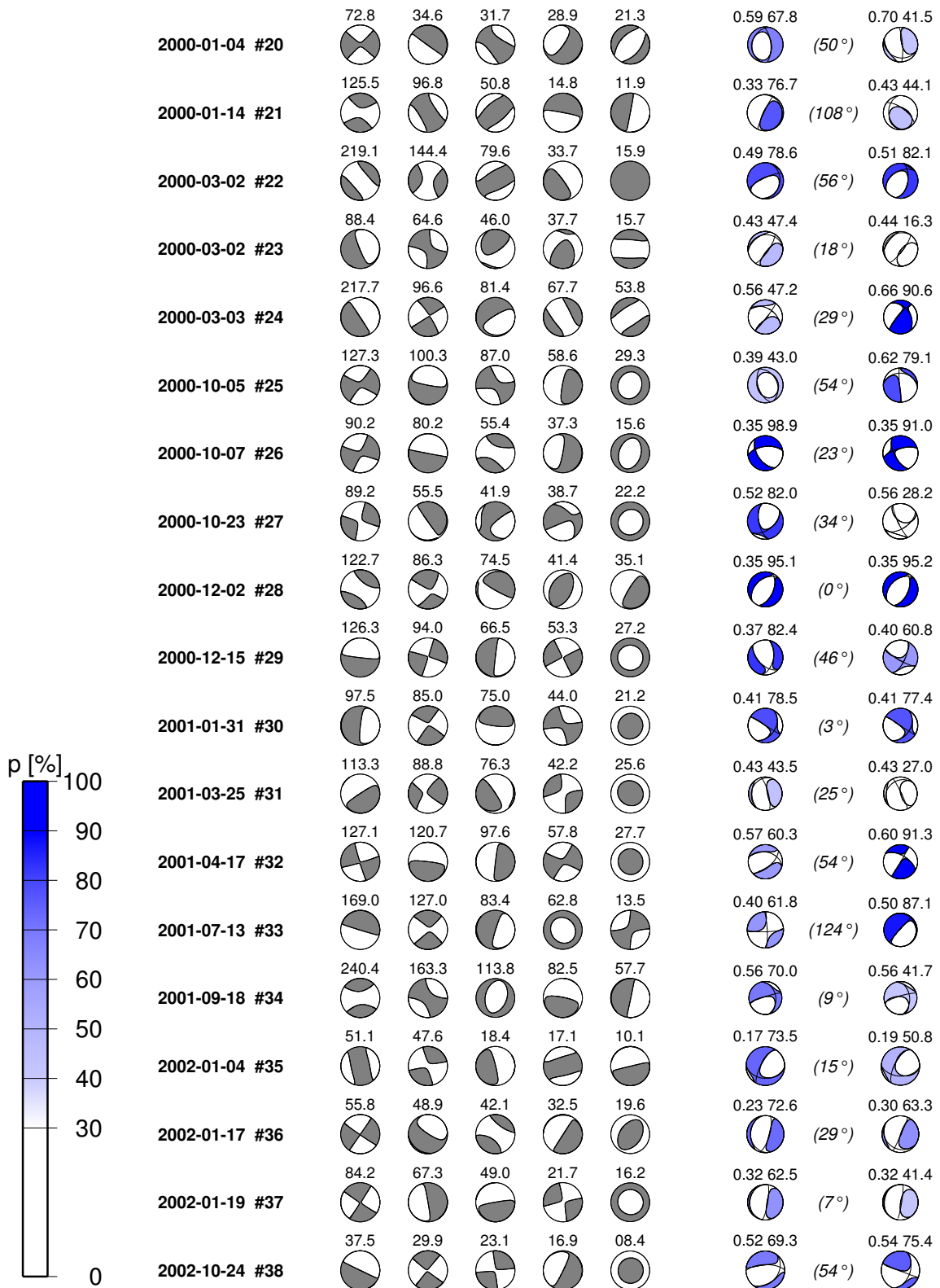
A good example, that a high variance does not consequently result in a high *DC*-percentage, is the moment tensor of event number 8 that occurred on 1996-12-21 and is inverted from nine waveforms. Although the variance is quite low and the low level of $f_{final}^{min} = 10$ mHz indicates rather well explainable waveforms ($\sigma = 0.31$) probably unbiased by crustal heterogeneities, the *DC*-percentage $p(\mathbf{m}_{dev}) = 32.2\%$ is quite low. When inverted by *SVD* and cut off by the highest order eigenvector, however, the double couple can be increased to $p(\mathbf{m}_{cut,4}) = 59.3\%$.

The moment tensors that are cut off by the highest order eigenvector often have a very similar shape of focal mechanism compared to the full solutions. So 19 of the 38 focal mechanisms show only minor changes in the double couple part ($|\Delta Ax| < 35^\circ$). This correlates with very low differences between the variances $\sigma(\mathbf{m}_{cut,4}) - \sigma(\mathbf{m}_{dev})$ that are 0.02 on average for these 19 solutions and 0.05 for all moment tensor inversions. This shows that the highest order eigenvector in most of the cases does not add relevant contributions to the moment tensor. On the other hand, these contributions can result from inconsistent data or random noise that both can result in decreased double couple percentages p (Kuge and Lay, 1994; Henry et al., 2002). Thus it could be concluded that the biased data mostly is of random nature, since the shape of the double couple mechanism is not changed by reducing noise when the highest order eigenvector is removed (Jost and Hermann, 1989). However, the expected increase of double couple percentage $p(\mathbf{m}_{cut,4})$ relative to $p(\mathbf{m}_{dev})$ occurs for 14 of 38 solutions. Additionally, inconsistencies may exist even in the lower order model-eigenvectors, that cannot be removed, since they contain a relevant amount of consistent data. So finally both sorts of biased data, random seismic noise and mismodelled structural heterogeneities, may be present to a minor degree in the used waveform data.

Figure 5.5: Singular value decomposition *SVD* of the 38 moment tensors calculated (next two pages). Waveform dataset, frequency pass-band and hypocentral depth are taken as described in Appendix A and B. First five columns show the model-eigenvectors of the *SVD* from low order to high order, according eigenvalues are written above. The next column gives the summation of all eigenvectors (\mathbf{m}_{dev}) and the very right column the cut-off solution composed of the four lowest order eigenvectors ($\mathbf{m}_{cut,4}$). Variance σ and double couple percentage p are written above the last two columns. Degrees in brackets are angular differences $|\Delta Ax|$ between \mathbf{m}_{dev} and $\mathbf{m}_{cut,4}$. Blue colour indicates the percentage of double couple p .



5.4 Singular value decomposition



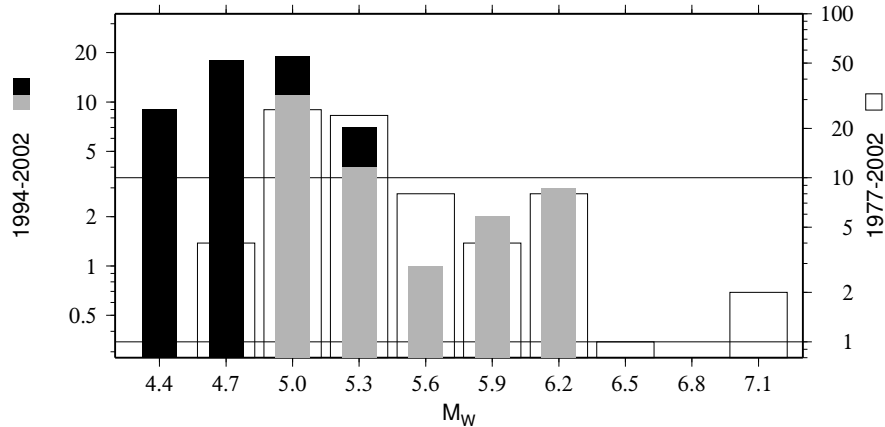


Figure 5.6: Number of determined moment tensors per magnitude. Bars represent number of events for magnitudes $x \leq M_W < x + 0.3$. Open bars symbolise *CMT*-solutions for 1977–2002 (26 years, right scale). Grey bars are *CMT*-solutions for the study period 1994–2002 (9 years) and black bars are the moment tensors obtained in this work (left scale). For comparability vertical axes are scaled by the length of the time period: $9/26 = 0.345$.

Still, by the empirical choice of the variance limits defined to exclude noisy and inconsistent waveforms (section 3.2), most of the biased data are removed from the final dataset and they are a good compromise between high signal-to-noise ratio and a sufficient amount of data that is necessary for moment tensor inversion. Finally, in particular the focal mechanisms with $p \leq 60\%$ show a stable mechanism against removing the highest order eigenvector. Only for events 2 and 25 the shape of the mechanism changes severely. Low double couple percentages are, however, also present on *CMT*-solutions and beyond this can be an effect of source complexity (Ide, 2001).

5.5 Magnitude threshold for eastern Africa

The presented frequency sensitive moment tensor inversion is able to determine source mechanisms for magnitudes as low as M_W 4.4 (event 34, 2001-09-18), while for eastern Africa the lowest magnitude for that a *CMT*-solution is provided is M_W 4.7 (Fig. 5.6). The level of completeness for *CMT*-solutions is approximately M_W 5.5 on a global scale (Arvidsson and Ekström, 1998). However, the magnitude for eastern Africa is lowered by this study and can be only estimated by statistical methods.

Following the Gutenberg-Richter relation there is an approximately tenfold increase in the number of earthquakes per magnitude (Gutenberg and Richter, 1954):

$$\log N = a - bM, \quad (5.1)$$

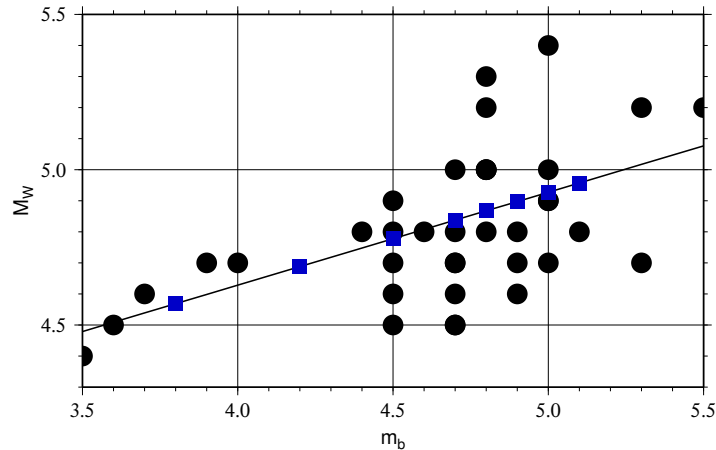


Figure 5.7: Moment magnitude M_W of the inversion results versus body-wave magnitude m_b given by the Engdahl catalogue of relocated earthquakes (Engdahl et al., 1998) (black dots). Blue squares indicate eastern African events during 1994–2002 for that no focal mechanism could be determined. For given m_b the corresponding M_W is calculated by the linear trend (black line) of the inverted events.

assuming $b = 1$. After Midzi et al. (1999) the b -value for eastern Africa is $b = 0.93$. Thus for an increase of $M_W = 0.3$ the number of events should increase by a factor of $10^{(0.3 \cdot 0.93)} = 1.9$. Figure 5.6 shows the magnitude statistics of determined moment tensors for eastern Africa from 1994–2002 studied in this work. Since equation 5.1 is only true for long time periods, the number of *CMT*-solutions from 1977–2002 is plotted in the background to illustrate the general trend. For this purpose the number of events is scaled by the number of years. However, for the regarded time periods the Gutenberg-Richter relation does not apply for the two major events that occurred in 1990, since in the last 100 years four events $M_W \geq 7.0$ took place (see chapter 1, Fig. 1.4). Especially with respect to the fact that the events both had a magnitude $M_W = 7.1$, the corresponding bar of $M_W = 7.1$ – 7.4 in the diagram is relatively high. The height of the $M_W = 6.2$ – 6.5 bar is also an statistical effect due to the short time period of *CMT*-determination, even though the corresponding eight events are neither temporally nor spatially correlated. Nevertheless, a linear trend can be seen from $M_W = 5.3$ – 6.2 for all *CMT*-solutions. Below this limit, routine moment tensor inversion is not complete. The combined solutions from *CMT* and this study, however, give a continuation of the trend to magnitudes $M_W \geq 5.0$. Thus the presented frequency sensitive moment tensor inversion is complete to approximately $M_W 5.0$ for eastern Africa.

This value is supported by the comparison of the moment magnitudes of the 38 events inverted and the remaining earthquakes out of the original dataset of 61 events (Fig. 5.7, Table A.3). Since magnitudes in the Engdahl catalogue are given as body-wave magnitudes m_b only, they must be correlated to moment magnitudes M_W to estimate the level of completeness of moment tensor inversion performed in this work. Generally there is a

scattered relation between m_b and M_W (Murphy and McLaughlin, 1998; Sipkin, 2003; Rezapour, 2003). Nevertheless, linear relations have been deviated that are valid only for magnitudes $M_W \geq 5.0$ (e.g. Giardini, 1988; Rezapour, 2003), since low moment magnitude information is hardly available as shown in this study. Murphy and McLaughlin (1998) provide a m_b - M_W relation connecting m_b 5.1 to M_W 5.4. Compared to this study their result cannot be verified. The linear trend plotted in Figure 5.7 rather connects m_b 5.1 to M_W 5.0. After 1996 for all events with $M_W \geq 4.9$ a moment tensor inversion is performed in this study. However, the m_b - M_W relation presented is highly scattered and thus it can be stated that a body-wave magnitude m_b 4.9 can be related to a range of $M_W = 4.7$ – 5.2 . So the level of completeness for moment tensor inversion is decreased to at least m_b 4.9 (moment magnitude $M_W \approx 5.0$ as discussed above).

Part II

Stress and strain

Chapter 6

Theory of the stress tensor

6.1 Properties of the stress tensor

The stress tensor $\boldsymbol{\sigma}$ was defined in section 2.1 as force per deformed area (eqn. 2.2). The tractions $\mathbf{t} = \hat{\mathbf{n}} \cdot \boldsymbol{\sigma}$, which result from stress on an arbitrary plane, can be separated in a component normal ($\boldsymbol{\nu}$) and tangential ($\boldsymbol{\tau}$) to the plane. The absolute scalar values of these vectors are the so-called normal stress $|\boldsymbol{\nu}|$ and shear stress $|\boldsymbol{\tau}|$, respectively and are calculated by (Ranalli, 1995):

$$|\boldsymbol{\nu}| = (\hat{\mathbf{n}}\boldsymbol{\sigma}) \hat{\mathbf{n}} \quad |\boldsymbol{\tau}| = (\hat{\mathbf{n}}\boldsymbol{\sigma}) \hat{\mathbf{t}}, \quad (6.1)$$

with \mathbf{t} lying in the plane defined by the orthogonal unit vectors $\hat{\mathbf{n}}$ and $\hat{\mathbf{t}}$.

An important property of the stress tensor is its symmetry. As shown in section 2.1 it is the reason for the symmetry of the moment tensor, which leads to the essential ambiguity of the moment tensor, that fault plane and auxiliary plane can not be discriminated. Hence the vital step of deriving the symmetry of the stress tensor will be discussed in detail.

One of the four conservation laws is the conservation of angular momentum. It states that the change of angular momentum must be equal to external body and surface forces. To evaluate the consequences of this law, the net torque of the external forces has to be calculated. When the earth is at a state of static equilibrium, the only relevant body force density is the gravitational body-force density \mathbf{g} and the surface force density is given by the traction vector \mathbf{t} . The calculation of the net torque \mathbf{N} for a continuous volume V applied by a lever arm \mathbf{x} mainly follows the formalism of Dahlen and Tromp (1998):

$$\begin{aligned} \mathbf{N} &= \int_V \mathbf{x} \times \mathbf{g} dV + \int_S \mathbf{x} \times \mathbf{t} dS \\ &= \int_V \mathbf{x} \times \mathbf{g} dV - \int_V \nabla \cdot (\boldsymbol{\sigma} \times \mathbf{x}) dV. \end{aligned} \quad (6.2)$$

Since the external forces must be equal to the angular momentum, it must be valid:

$$\int_V [\rho_0 (\mathbf{x} \times \partial_t^2 \mathbf{s})] dV = \int_V [\mathbf{x} \times \mathbf{g} - \nabla \cdot (\boldsymbol{\sigma} \times \mathbf{x})] dV. \quad (6.3)$$

And the integrand terms has to vanish:

$$\rho_0 (\mathbf{x} \times \partial_t^2 \mathbf{s}) - \mathbf{x} \times \mathbf{g} + \nabla \cdot (\boldsymbol{\sigma} \times \mathbf{x}) = \mathbf{0}. \quad (6.4)$$

To solve equation 6.4, the lever arm \mathbf{x} is separated. This is easily done for the first two terms and shown in appendix C for the third term (eqn. C.6). It follows:

$$\mathbf{x} \times (\rho_0 \partial_t^2 \mathbf{s} - \nabla \boldsymbol{\sigma} - \mathbf{g}) - \wedge \boldsymbol{\sigma} = \mathbf{0}. \quad (6.5)$$

The term within the parentheses is the momentum equation that is a zero-vector because of the conservation of momentum. Thus, the wedge operator (\wedge) applied on the stress field must be a zero-vector as well and the stress tensor $\boldsymbol{\sigma}$ must be symmetric (eqn. C.9):

$$\wedge \boldsymbol{\sigma} = \varepsilon_{ijk} \boldsymbol{\sigma}_{jk} = \mathbf{0} \quad \iff \quad (\boldsymbol{\sigma})^T = \boldsymbol{\sigma}. \quad (6.6)$$

Like any tensor, the stress tensor can be separated in an isotropic and a deviatoric part (compare **M** in equations 2.31, 2.32):

$$\boldsymbol{\sigma}_{dev} = \boldsymbol{\sigma} - \underbrace{\frac{1}{3} \text{tr}(\boldsymbol{\sigma}) \cdot \mathbf{I}}_{\boldsymbol{\sigma}_{iso}}. \quad (6.7)$$

This allows to discriminate between the isotropic state of stress with equal normal stresses acting on each surface defined by the coordinate system, and the remaining deviatoric stresses. Below a depths of a few kilometres it is often assumed that all normal stresses are equal to the pressure of the overburden (lithostatic state of stress, **Stein and Wysession, 2003**) and the deviatoric stresses vanish. Thus, tectonic forces, which e.g. cause fracture of material, change only the deviatoric stress.

Another important transformation is the rotation of a tensor in its system of principal axes. Applying the eigenvalue equation (eqn. 2.26) the eigenvalues of the stress tensor $\sigma_1, \sigma_2, \sigma_3$ called principal stresses and the according eigenvectors $\hat{\mathbf{e}}^i$ can be calculated. Since within the earth most stresses are compressive, in geosciences sign-convention links compression to positive stress, the eigenvalues are mostly ordered as $\sigma_1 \geq \sigma_2 \geq \sigma_3$. By the three principal axes a coordinate system is defined for which no shear stresses act on the normal planes of the coordinate axes:

$$\boldsymbol{\sigma} = \begin{pmatrix} \sigma_1 & 0 & 0 \\ 0 & \sigma_2 & 0 \\ 0 & 0 & \sigma_3 \end{pmatrix}. \quad (6.8)$$

To understand how stress can be derived form moment tensors, the relation between maximum shear stress and focal mechanisms as the geometrical representations of moment

tensors will be discussed. For this purpose the plane with normal $\hat{\mathbf{n}}$ on that the maximum shear stress occurs is calculated, since this would be the plane a newly generated fracture would occur. By rotating the coordinate system in the system of the principle axes (eqn. 6.8), using Cauchy's formula (eqn. 2.3) and the definition of shear and normal stress (eqn. 6.1), the squared magnitude of the shear stress $\boldsymbol{\tau}^2$ is (Stein and Wysession, 2003):

$$\begin{aligned}\boldsymbol{\tau}^2 &= \mathbf{t}^2 - \boldsymbol{\nu}^2 \\ &= (\sigma_1 n_1)^2 + (\sigma_2 n_2)^2 + (\sigma_3 n_3)^2 - (\sigma_1 n_1^2 + \sigma_2 n_2^2 + \sigma_3 n_3^2)^2.\end{aligned}\quad (6.9)$$

Since $\hat{\mathbf{n}}^2 = n_1^2 + n_2^2 + n_3^2 = 1$, the shear stress is only a function of two independent principle axes. To find the maximum shear stress, the derivatives of $|\boldsymbol{\tau}|(n_1, n_2)$ with respect to n_1 and n_2 must be zero. Some elementary algebra results in the trivial solutions for the three basic vectors, that obviously are the minima solutions with $|\boldsymbol{\tau}| = 0$ —no shear stress on the normal planes. Beside this six relative maxima solutions for $\boldsymbol{\tau}^2$ and $\hat{\mathbf{n}}$ exist:

$$\boldsymbol{\tau}_i^2 \cdot \varepsilon_{ijk} = \frac{1}{4} (\pm(\sigma_j - \sigma_k))^2; \quad n_j^2 = n_k^2 = \frac{1}{2}; \quad n_i^2 = 0.\quad (6.10)$$

Because of $\sigma_1 \geq \sigma_2 \geq \sigma_3$, the absolute maximum shear stress is (Stein and Wysession, 2003):

$$|\boldsymbol{\tau}| = \frac{1}{2} (\sigma_1 - \sigma_3); \quad \hat{\mathbf{n}} = \frac{1}{\sqrt{2}} (\pm 1, 0, 1)^T.\quad (6.11)$$

These two planes include the intermediate principal stress axis σ_2 and bisect the direction of maximum and minimum principal stress σ_1 and σ_3 , respectively. Thus, for a homogeneous medium newly generated fractures should occur on these axes of maximum shear stress. If that was true, the seismic moment tensor per volume would represent the stress tensor, since both would have the same system of principle axes with respect to the possible fault planes (eqn. 2.28). However, laboratory experiments show that fracture occurs preferably at 25° – 30° , rather than 45° , from the direction of the maximum principal stress direction. The reason for that behaviour is that equation 6.1 does not take account of internal friction. The more precise fracture criterion is the Coulomb-Mohr criterion:

$$|\boldsymbol{\tau}| = \tau_0 - \mu\nu; \quad \mu^{-1} = -\tan 2\theta.\quad (6.12)$$

It states for which shear stress $|\boldsymbol{\tau}|$ fracture on a newly built fault occurs relative to the normal stress $|\boldsymbol{\nu}|$ for a medium with cohesive strength τ_0 and the coefficient of internal friction μ . At this the shear and normal stress are given on a plane with normal vector at an angle θ to σ_1 . Since rocks typically have $\mu = 0.75$, it follows that $\theta = 63^\circ$ and thus fractures occurs on a plane 27° to the σ_1 - and σ_2 -plane, agreeing with rock deformation experiments (Stein and Wysession, 2003).

So far, only newly generated fractures have been regarded. McKenzie (1969) showed that for the case of re-activated faults the uncertainty of stress estimation from focal mechanisms is even higher. Thus, in dependence on internal friction and fault orientation, the direction

of maximum horizontal stress may be located anywhere in the dilatational quadrant of the focal mechanism.

From the rheological point of view, the generation of new fractures would occur at an angle $\theta = 45^\circ$ only in a source volume with no internal friction and only then the principle axes of stress tensor and moment tensor would be identical. The same conclusion was made in section 2.1: Only in case of an isotropic physical stress $\boldsymbol{\sigma}_{true}$ (see eqn. 2.12) within the source volume, the stress glut $\boldsymbol{\Gamma}$ would reduce to the modelled stress $\boldsymbol{\sigma}_{model}$ calculated by Hook's law.

Nevertheless, single focal mechanisms can be used as stress indicators within certain error bounds, dependent on the difference between θ and 45° . However, a better estimation of the predominating stress field can be achieved when a set of mechanisms is available for a region with a homogeneous first order stress field. The necessary procedure of stress inversion will be discussed in the next chapter.

6.2 Formal stress inversion

Even though earthquakes are a result of present shear stress (eqn. 6.12), stress orientations deduced from single focal mechanisms are a poor proxy for the existing stress field (section 6.1). Thus without further assumptions, principal stress and moment tensor axes are not interchangeable. Nevertheless, if several focal mechanism solutions are available, the inversion of the stress field is possible (Gephart and Forsyth, 1984).

Different algorithms of stress inversion from focal mechanisms have been developed by various authors (e.g. Angelier, 1979; Gephart and Forsyth, 1984; Michael, 1984; Reches, 1987; Rivera and Cisternas, 1990; Angelier, 2002) that all are based on following assumptions for the study region:

- (a) The stress field is uniform and spatially and temporary invariant.
- (b) The direction of earthquake slip $\hat{\mathbf{d}}$ occur in direction of maximum shear stress $\hat{\boldsymbol{\tau}}$ (Wallace-Bott hypothesis, Bott, 1959).

While the first point is respected by binning seismic events in distinct tectonic regions (section 7.2) the second is expressed by:

$$\hat{\boldsymbol{\tau}} = \frac{\boldsymbol{\tau}}{|\boldsymbol{\tau}|} = \hat{\mathbf{d}}, \quad (6.13)$$

while $\boldsymbol{\tau}$ can be written using equations 2.3, 6.1:

$$\boldsymbol{\tau} = \boldsymbol{\sigma}\hat{\mathbf{n}} - [(\boldsymbol{\sigma}\hat{\mathbf{n}})\hat{\mathbf{n}}]\hat{\mathbf{n}}. \quad (6.14)$$

However, some authors negate stress estimation from focal mechanism data (Twiss and Unruh, 1998). They argue that during fracture, the strain release violates the assumption of parallel slip and maximum shear stress direction, so stress inversion would not be possible for earthquake data.

Nevertheless, stress inversion is an established and widely used method to extract stress informations implied in earthquake source mechanisms. A major difference between stress inversion techniques is the handling of the focal mechanism ambiguity concerning the fault plane. Since stress inversion was at first used for slickenside field data, some algorithms need the fault plane to be determined a priori. In most cases this is not possible, since further information would be needed to determine which nodal plane was the fault plane. Angelier (2002) provided a method, that automatically chooses which auxiliary plane is the true fault plane by maximising the sum of the scalar product of slip vector and shear stress vector ($\boldsymbol{\tau} \cdot \hat{\mathbf{d}}$, that is the orthogonal projection of shear stress on the slip vector).

Another method to decide for one of the nodal planes is to perform the inversion as if all nodal planes were independent data, primary and to remove the worse fitted auxiliary planes in a second step. The final inversion then includes the planes that are best fitted by a uniform stress field (Gephart and Forsyth, 1984). This approach is applied in this work and as long as no further information is available, it is a good estimation of fault planes for a set of earthquakes. For this dataset the deviation between data slip vectors and calculated ones is obtained using the stress inversion routine developed by Michael (1984). Thus the average angle between the calculated shear stress $\hat{\boldsymbol{\tau}}$ and the slip vector $\hat{\mathbf{d}}$ of the best fitted nodal plane is denoted by $\bar{\beta}$. To take account of the focal plane ambiguity a statistical approach is applied, that inverts different combinations of fault planes, to see which stress tensor is most likely. The composition of each dataset is twofold. At first a bootstrap routine is performed that pick n mechanisms at random from the original n events. Each dataset than will have some mechanisms repeated 2 or more times (Michael, 1987b). Thereafter the fault plane is chosen randomly from the two auxiliary planes (Michael, 1987a). Since this strategy does not decide for one fault plane and dependence on individual focal mechanism solutions is decreased, this method seems appropriate. Additionally, confidence limits of the principle stress axes can be displayed by plotting the inversion results of all bootstrapped datasets on a stereonet (see section 7.2).

The difference of the inversion routine provided by Michael (1984) with respect to other methods is the linearisation of the inversion problem, that massively reduces the computing time and does not need any starting model, that is necessary for non-linear inversions. Thus the time-consuming bootstrap-resampling is performable in short times.

Because of equation 6.14, $\boldsymbol{\tau}$ is linear with respect to the stress tensor $\boldsymbol{\sigma}$; thus $|\boldsymbol{\tau}|$ is not. To linearise the inversion, it is assumed that similar magnitudes of shear stress are present on each inverted fault. If only relative shear stresses magnitudes are regarded, the optimum shear stress magnitude can be set a priori to one, so the inversion additionally minimises

for:

$$(|\boldsymbol{\tau}| - 1)^2 \rightarrow \min. \quad (6.15)$$

Hence, the inversion minimises for both, difference between slip direction and direction of maximum shear stress on one hand and difference between the shear stress magnitudes on the other. Combining equations 6.13 and 6.14 with the magnitude constraint (eqn. 6.15), a transformation matrix \mathbf{A} can be achieved. As in moment tensor inversion (eqn. 2.41) only the deviatoric part of the stress tensor, expressed by the vector \mathbf{p}_{dev} , is calculated with $\sigma_{33} = -\sigma_{11} - \sigma_{22}$. The equation to be inverted than is:

$$\hat{\mathbf{d}} = \mathbf{A}\mathbf{p}_{dev}; \quad \mathbf{p}_{dev} = (\sigma_{11}, \sigma_{12}, \sigma_{13}, \sigma_{22}, \sigma_{23})^T. \quad (6.16)$$

Here the data vector $\hat{\mathbf{d}}$ has a length of $3m$, when m slip vectors are included in the dataset and accordingly \mathbf{A} is a $3m \times 5$ matrix. If however, slip vectors are too similar, data are not independent and the inversion is under-determined and cannot be solved uniquely (Michael, 1984).

Chapter 7

Stress and strain calculation

7.1 Focal mechanism solutions of eastern Africa

The source mechanisms determined in the first part of this work are used to invert for the regional stress field in eastern Africa. These 38 calculated focal mechanisms for the years 1994–2002 (Table A.1) are combined with other mechanisms determined by moment tensor inversion. Obviously, the greatest number is taken from the Harvard-*CMT* catalogue that provides 90 focal mechanisms from 1977 until 2005 within the study region (24°S–10°N, 20°W–51°W, Table A.4). Beside the source mechanisms of the presented study, for no additional earthquake $M_W \geq 3.5$ a moment tensor inversion was determined since 1977. Only Ferdinand and Arvidsson (2002) calculated moment tensors for three small events M_W 2.0–3.3. However, 17 additional mechanisms of strong events are given by four publications from 1964–1977 (Table A.4). First, Shudofsky (1985) presented the focal mechanism solutions of these 17 events in eastern Africa, inverting globally recorded Rayleigh-waveforms for the seismic moment tensor. Later studies re-evaluated seven of these events using body-waveform inversion of frequencies $\mathcal{T} \approx 10$ s and layered crustal models: Foster and Jackson (1998) determined focal mechanisms for several large African earthquakes, five of which are included in the stress inversion of this work. Two additional focal mechanisms are taken from the studies of Grimison and Chen (1988) and Nyblade and Langston (1995).

Figure 7.1 shows the 145 focal mechanisms within the region of interest. Most seismicity is located on or near the East African Rift System (*EARS*). Neighbouring areas with known source mechanisms are the Davie Ridge on the eastern continental margin and the region west of the *EARS*. Some events on Madagascar and one further north in the Indian Ocean complete the dataset. The dominating mechanism is normal faulting roughly oriented north/south, but several strike-slip mechanisms and single thrust mechanisms are observed as well (paragraph 5.2.4). Along the *EARS* fault orientation predominantly is parallel to the rift structure, suggesting that a majority of earthquakes occurred on re-activated faults.

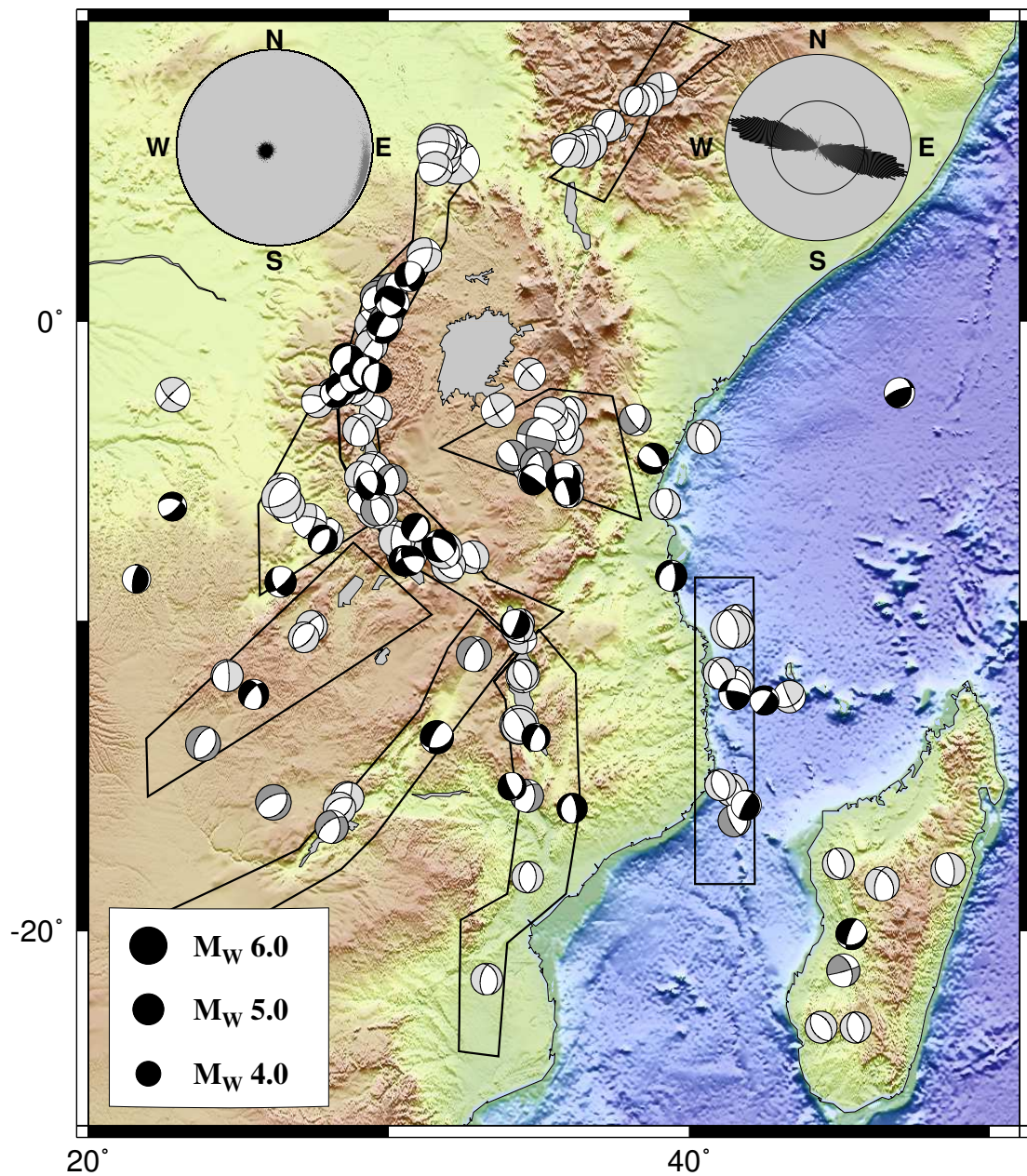


Figure 7.1: Stress inversion for all 145 events and *GSHAP*-zonation of eastern Africa. Light grey focal mechanisms indicate *CMT*-solutions (1977–2005), dark grey mechanisms are taken from literature (before 1977, references see text) and black beach balls are the solutions of this work (1994–2002). The upper left stereonet (a lower hemisphere stereographic projection as the beach ball) shows the directions of maximum principle stress σ_1 (black dots) and of minimum principle stress σ_3 (grey dots) for the bootstrap analysis. The upper right rose diagram shows the corresponding orientations of minimum horizontal stress S_h . Radius scales with number of bootstrapped inversions. Additionally shown are the eight areas defined by *GSHAP* (Midzi et al., 1999).

7.2 Zonation of eastern Africa and stress inversion

Stress inversion requires a uniform and invariant stress field within the study region (chapter 6.2). To estimate the first-order stress pattern for entire eastern Africa, primary the stress inversion is performed for all 145 events, including both nodal planes of all focal mechanisms. Thereafter the worse fitted plane (maximum $\bar{\beta}$) is excluded and the inversion performed again for the optimum set of nodal planes. Finally, confidence limits are estimated by a bootstrap analysis (Michael, 1987a).

Figure 7.1 shows the result of the stress inversion for whole eastern Africa. Since in eastern Africa predominantly extensional regimes are present, the orientation of minimum horizontal stress S_h is plotted, which in case of normal faulting regimes is parallel to the orientation of minimum principle stress σ_3 . The inversion results in a west-northwest/east-southeast oriented minimum horizontal stress for eastern Africa, for a pure extensional regime. Hence, the direction of maximum principle stress σ_1 is nearly vertical, while the eigenvector of minimum principle stress σ_3 is parallel to S_h . The bootstrap analysis reveals a very small region of confidence for the direction of σ_1 , indicating an extensional regime all over eastern Africa. However, the direction of σ_3 is little constrained and thus for the optimum set of nodal planes the misfit angle $\bar{\beta} = 26^\circ \pm 34^\circ$ is rather high.

Since for the inversion of entire Africa focal mechanism data are inconsistent and thus the misfit angle is rather high, the region is divided into sub-areas, to study regional changes in stress orientation. For this purpose the zonation of the Global Seismic Hazard Assessment Program (*GSHAP*) is applied as a first attempt. These worldwide zonations take into account the recent and historic seismicity and hence define areas with a common seismic risk (Giardini, 1999; Grünthal et al., 1999). Hereby, eastern Africa is divided into 21 areas from the Afar-region in the north to southern South Africa, eight of which are located in the study region (Midzi et al., 1999, Fig. 7.1). In an automatised procedure the focal mechanism solutions are then binned into the several areas by an point-in-polygon routine (Franklin, 2003). By this means, datasets of focal mechanism solutions are defined, for that the stress inversion can be performed.

The northern part of the western rift branch hence is covered by one single area. In terms of seismic hazard assessment the region is uniform (Midzi et al., 1999), but as it contains 54 events and thus more than a third of the data, it is worthwhile to study it in detail. To investigate stress variations along the western rift, separate stress inversions are performed for sub-areas defined by a shifted box of 3° in latitude. Seven steps result in areas that contain between 12 and 20 focal mechanisms. The inversion results are shown in Figure 7.2 and reveal a rotating direction of σ_3 along the rift from east-northeast/west-southwest in the southern part of Lake Tanganyika to west-northwest/east-southeast in the northern part of the western rift branch. Angles of misfit vary between $\bar{\beta} = 10^\circ$ and $\bar{\beta} = 20^\circ$, while confidence regions given by the bootstrap analysis are small to medium sized. Nevertheless, the estimation of the first-order stress reveals a rotating trend along the rift. Hence, for all seven sub-areas the axis of minimum principal stress is always approximately perpendicular

Table 7.1: Stress inversion results for eastern Africa. See Figure 7.3 and 7.4 for definition of boundaries of inverted areas.

| location | area | S_h [°] | nr | β [°] | $\Delta\beta$ [°] | $ \tau $ | $\Delta \tau $ |
|---------------------|------|-----------|----|-------------|-------------------|----------|----------------|
| Ethiopian Rift | 1 | 114 | 7 | 10.5 | 12.6 | 0.94 | 0.19 |
| Aswa fault-zone | 2 | 176 | 7 | 12.5 | 9.7 | 0.95 | 0.13 |
| Western branch (NW) | 3 | 113 | 15 | 12.9 | 13.9 | 0.90 | 0.25 |
| Western branch (W) | 4 | 117 | 17 | 10.6 | 13.3 | 0.90 | 0.25 |
| Lake Tanganyika | 5 | 87 | 22 | 18.4 | 21.5 | 0.89 | 0.19 |
| Lake Malawi | 6 | 69 | 14 | 16.9 | 26.6 | 0.86 | 0.22 |
| Western Kenya | 7a | 2 | 8 | 25.9 | 22.9 | 0.76 | 0.27 |
| Kenya Rift | 7b | 83 | 7 | 3.3 | 3.3 | 0.98 | 0.16 |
| 7a+b | 7 | - | 15 | 40.7 | 30.9 | 0.63 | 0.28 |
| Zambia | 8a | 118 | 12 | 7.9 | 5.3 | 0.96 | 0.16 |
| Southern Congo | 8b | 124 | 6 | 6.2 | 5.8 | 0.96 | 0.19 |
| 8a+b | 8 | 122 | 18 | 8.5 | 6.4 | 0.96 | 0.16 |
| Davie Ridge | 9a | 76 | 20 | 23.6 | 27.0 | 0.78 | 0.28 |
| Madagascar | 9b | 79 | 7 | 11.9 | 6.7 | 0.93 | 0.22 |
| 9a+b | 9 | 83 | 27 | 25.6 | 33.2 | 0.77 | 0.26 |

Columns as follows: location of area, number of area (see Fig. 7.3 and 7.4 for boundaries), direction of minimal horizontal compressional stress S_h clockwise from north, number of inverted focal mechanisms, average misfit angle β and standard deviation $\Delta\beta$, normalised shear stress amplitude $|\tau|$ and standard deviation $\Delta|\tau|$.

to the main fault and rift valley orientation.

For the other areas defined by the *GSHAP*-zonation it is obvious that some focal mechanisms are not binned into areas at all. Especially groups of events on Madagascar, the continental margin and the Main Ethiopian Rift lie outside the defined areas. As a consequence the *GSHAP*-classification is adapted to the dataset of 145 focal mechanisms. This re-organisation covers all focal mechanism solutions, except of the three separate events in the west (events 18 and 32 of this work plus a *CMT*-solution) and the event in the Indian ocean (event 6). These events are located several hundreds of kilometres away from the nearest mechanism and are probably indicators of a changing tectonic regime towards the mid oceanic ridges (paragraph 5.2.2).

Several zonations have been tested to study dependencies and reliability of the stress inversion. Two variants are shown that are based on the *GSHAP*-classification and improved for the purposes of this work. The presented divisions differ only for the region of Southern Congo and Zambia (area 8), the eastern rift itself (area 7) and the continental margin (area 9). For the first variant, areas 8 and 9 are split in two parts, whereas area 7 is united (Fig. 7.3). The second one is the final zonation for stress inversion in eastern Africa (areas 8,

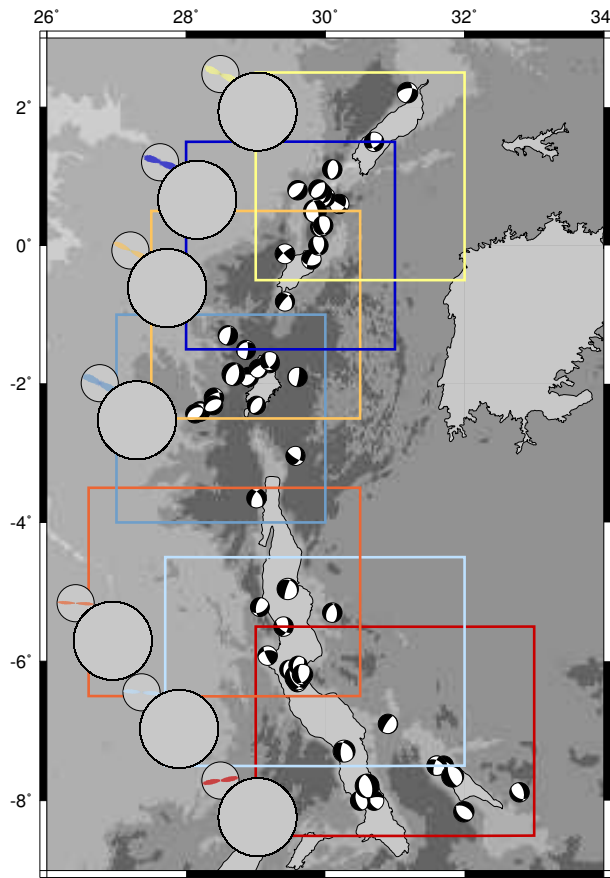


Figure 7.2: Stress inversion of focal mechanisms within sub-areas arranged along the western rift branch. Coloured boxes border sub-areas of inverted focal mechanisms. Great stereonet projections show directions of principal stresses (black: σ_1 , coloured: σ_3), small rose diagrams above show the minimum horizontal stress S_h . Colours correspond to inverted sets of focal mechanisms.

9 united; area 7 separated, Fig. 7.4). The quantitative results of the stress inversions for the distinct areas are summarised in Table 7.1.

Both zonal deviations have those areas in common that are located along the western rift branch and north of it. The two areas 1 and 2 only include seven focal mechanisms each. For this small amount of data the inversion consequently results in a low misfit angle $\bar{\beta} = 11^\circ \pm 13^\circ$ (area 1) and $\bar{\beta} = 13^\circ \pm 10^\circ$ (area 2, see Table 7.1) Additionally, both inversions show small confidence regions for the direction of minimum principle stress σ_3 and thus a stable orientation of minimum horizontal stress S_h (Fig. 7.4). However, σ_1 cannot be fixed for both of the areas that is caused by the appearance of both, normal and strike-slip mechanisms. Areas 1 and 2 have a minimum distance of 300 km and show a strong difference in S_h that is northwest/southeast for area 1 and roughly north/south for area 2. Area 2 is located on the Aswa fault-zone and covers the main- and aftershocks

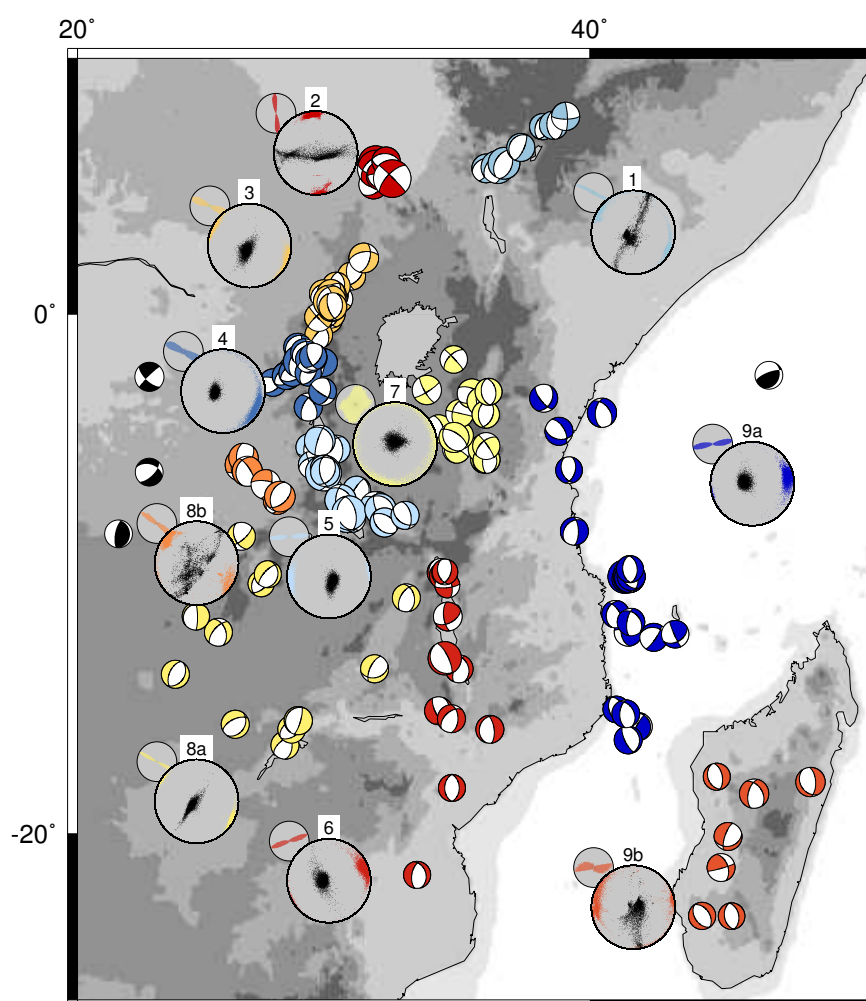


Figure 7.3: Stress inversion for first zonation variant. Colours correspond to inverted sets of focal mechanisms. See Figures 7.1 and 7.2 for details.

of the 1990 Sudan earthquake until 1991 (chapter 1). Area 1, however, covers the Main Ethiopian Rift with frequent seismicity. As for the western rift branch, here S_h is oriented perpendicular to the fault.

Further south the western branch of the *EARS* follows, that was already described above. Here three sub-areas are chosen to obtain an increased number of events per area and a uniform stress field at the same time. S_h is oriented roughly 90° to the rift valley and the direction of σ_1 is quite stable while direction of σ_3 varies little. The southern part of the western rift along Lake Malawi (area 6) is seismically less active than the northern segments. Thus 14 events with a north/south extent of ~ 1500 km on or near the main fault are inverted. Although related to the rift, the focal mechanisms do not result in a clear stress orientation ($\bar{\beta} = 17^\circ \pm 27^\circ$). However, mean S_h is oriented northeast/southwest

and is mainly governed by the focal mechanism solutions at Lake Malawi in the rift valley. Hence S_h is still perpendicular to the *EARs*, that here roughly runs north-northwest/south-southeast. The two southernmost focal mechanisms are located in Mozambique in an area of principally high seismic activity (Hartnady, 1990), where also the recent M_W 7.0 earthquake on 2006-02-22 took place (chapter 1). South of $\sim 22^\circ\text{S}$ seismicity decreases rapidly (Fairhead and Stuart, 1982).

The following areas are inverted for a separated and a united variant each. Area 7 is located along the Kenya Rift on the eastern branch and further west towards Lake Victoria. It shows a very scattered stress inversion result (Fig. 7.3, $\bar{\beta} = 41^\circ \pm 31^\circ$) with a vertical direction of σ_1 , but no constraint for the σ_3 -axis. Dividing the area along a north/south trending line west of the rift, results in a better constraint stress orientation but still large regions of confidence for western Kenya (area 7a, Fig. 7.4) with S_h roughly oriented north/south. In contrast, the Kenya Rift (area 7b) includes very consistent focal mechanisms that can be explained by an east/west oriented direction of σ_3 , perpendicular to the rift trend ($\bar{\beta} = 3^\circ \pm 3^\circ$). The maximum principle stress direction, however, shows no clear focus.

The two great areas neighbouring the *EARs* to the west and east are represented by areas 8 and 9. Because of their large extent but relatively low seismicity, it is worthwhile to study if within those areas regional stress variations exist. Figure 7.3 shows one possibility of division into two separate areas. The smaller areas 8b and 9b are spatially distinct regions including six and seven focal mechanisms, respectively and consequently result in a low $\bar{\beta}$ -value. Nevertheless, the bootstrap analysis shows very large confidence regions for directions of both, minimum and maximum principle stress. Thus for Madagascar and the area south of Lake Tanganyika no reliable stress inversion can be performed, either due to insufficient data or because of a non-uniform stress field. The larger areas 8a and 9a, however, show different results. The eastern continental margin, including the Davie-Ridge within the Mozambique channel (area 9a), contains 20 focal mechanisms. The inversion of these data results in S_h oriented east-northeast/west-southwest that is $\sim 90^\circ$ to the trend of the continental margin and the Davie-Ridge. The difference between direction of calculated shear stresses and the according slip vectors, however, is rather large with $\bar{\beta} = 24^\circ \pm 27^\circ$. The bootstrap analysis reveals an extensional regime with a slightly varying direction of σ_3 . The oppositional result is given for area 8a with a low $\bar{\beta} = 8^\circ \pm 5^\circ$, good constrained direction of σ_3 and relatively clear vertical direction of σ_1 . Thus for the high plateau of Zambia (area 8a) S_h orientation differs from S_h at the rift areas in the north and west (areas 5 and 6). Since both datasets 8b and 9b are too small for a reliable stress inversion and because of their similar trends with respect to areas 8a and 9a, 8a/8b and 9a/9b are joint together (Fig. 7.4). The stress inversion of focal mechanisms of both areas results in reliable deviatoric stress tensors with medium confidence regions for σ_1 and σ_3 . While area 9 has a high misfit angle, area 8 shows a very good fit in spite of the large area.

The final stress inversion reveals a clear trend of rotating stress pattern from northwest to southeast. While the northwestern segments of the *EARs* (areas 1, 3, 4) and the region south of it on the high plateau of Zambia and southern Congo (area 8) have extensional

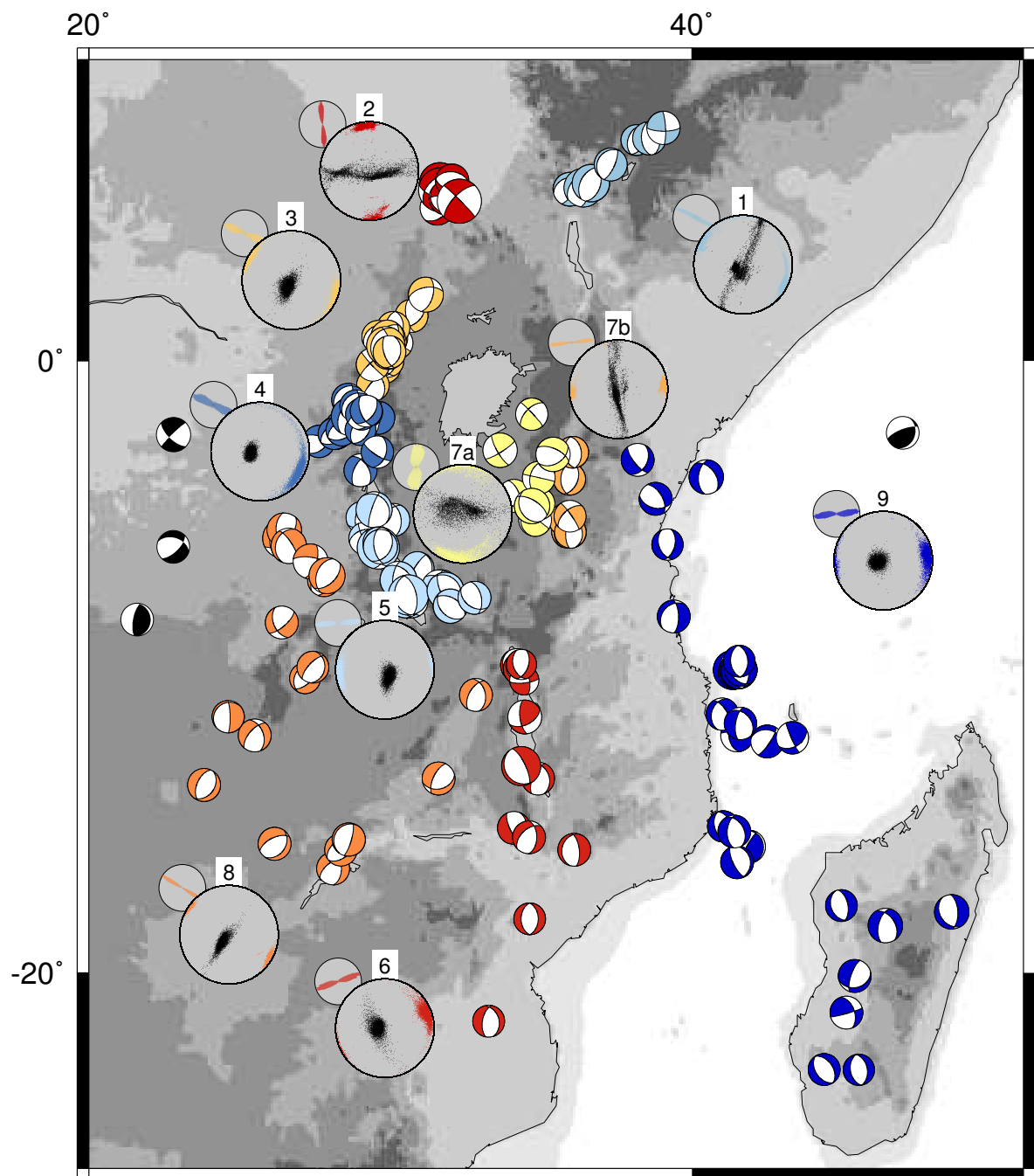


Figure 7.4: Stress inversion for final zonation. Colours correspond to inverted sets of focal mechanisms. See Figures 7.1 and 7.2 for details.

regimes with west-northwest/east-southeast direction of minimum horizontal stress S_h , the eastern rift branch (area 7b), the southernmost rift segment along Lake Malawi (area 6) and the continental margin including Madagascar (area 9) reveal a direction of S_h east-northeast/west-southwest. Only the distinct areas along the Aswa fault-zone (area 2) and area 7a between the eastern rift branch and Lake Victoria show a different stress orientation of S_h oriented north/south.

7.3 Strain rates

The knowledge of earthquake source mechanisms allows to calculate cumulative seismic strain rates for the studied time period. Therefore, the newly determined focal mechanisms of this study are combined with the *CMT*-solutions in eastern Africa, in order to calculate extension rates for the zonation defined in section 7.2.

Recent studies are based on data of the Global Positioning System (*GPS*) to estimate extension rates of the East African Rift System (*EARS*). Thus, the pole of rotation was determined between the Nubian and Somalian subplate to be south of Africa, near the Southwest Indian Ridge (Fernandes et al., 2004). Opening rates were calculated to be east/west oriented with 7 mm/a for the Ethiopian Rift and 2 mm/a in southeastern Africa. Marine geophysical data was used by Chu and Gordon (1999) who put the pole of rotation offshore near the coast of southern Mozambique. They proposed a zone of convergence (2 mm/a) for the aseismic region south of that pole and up to 6 mm/a extension on the *EARS*. Compared to the oceanic spreading centres, the continental *EARS* is a diffuse zone of extension. Hence Kreemer et al. (2003) referred an extension rate of 1.6 mm/a to all eastern Africa by compiling different datasets within the scope of the Global Strain Rate Map Project. However, Calais et al. (2006) combined *GPS*- and *CMT*-data to separate the opening of the two branches. With a total rate of 5–6 mm/a they obtained the major part of opening for the western rift branch (2–5 mm/a) and the minor part for the eastern rift branch (1–3.5 mm/a).

Kostrov (1974) showed that if all deformation is seismic, the average seismic strain rate tensor $\dot{\epsilon}$ can be calculated by summing all moment tensors \mathbf{M}^k that occurred in a volume V within a time period t :

$$\dot{\epsilon}_{ij} = \frac{\sum_k M_{ij}^k}{2\mu V t}. \quad (7.1)$$

After Jackson and McKenzie (1988) the eigenvalue λ_T , corresponding to the tension-axis $\hat{\mathbf{e}}^T$ of $\sum_k \mathbf{M}^k$, is taken to calculate the strain rate $\dot{\epsilon}_T$ perpendicular to an extending rift:

$$\dot{\epsilon}_T = \frac{\lambda_T}{2\mu V t}. \quad (7.2)$$

Table 7.2: Average extension rates for the rift segments of the East African Rift System (1985–2005).

| location | area | L [km] | λ_T [10^{18} Nm] | v_T [mm/a] | |
|---------------------|------|----------|-----------------------------|--------------|---|
| | | | | this study | references |
| Ethiopian Rift | 1 | 420 | 4.1 | 0.26 | }0.34 2–5 ¹ |
| Western branch (NW) | 3 | 420 | 2.6 | 0.17 | |
| Western branch (W) | 4 | 330 | 2.6 | 0.21 | |
| Lake Tanganyika | 5 | 540 | 24.7 | 1.2 | |
| Lake Malawi | 6 | 1300 | 3.8 | 0.08 | |
| Kenya Rift | 7b | 300 | 0.5 | 0.04 | |
| Davie Ridge | 9a | 1500 | 5.3 | 0.09 | }0.08 1–3.5 ¹ |
| total | | 4810 | 43.6 | 0.24 | 1.6 ² , 2–7 ³ , ≤ 6 ⁴ |

Columns as follows: location of rift segment, number of area (see Fig. 7.3 and 7.4 for boundaries), length of rift-segment L , eigenvalue λ_T of the tension-axis of the summed moment tensor $\sum_k \mathbf{M}^k$ and average extension rate v_T in direction of opening. Reference values are taken from: ¹Calais et al. (2006), ²Kreemer et al. (2003), ³Fernandes et al. (2004), ⁴Chu and Gordon (1999).

Thus the extension rate v_T can then be determined by:

$$v_T = \dot{\epsilon}_T \cdot w = \frac{\lambda_T}{2\mu L dt}, \quad (7.3)$$

for the volume $V = Lwd$ with the width w , the length of the rift segment L and the seismogenic depth d .

Opening rates are calculated by equation 7.3 for those areas defined in section 7.2 that are directly located on the rift branches. A shear modulus of $\mu = 3 \cdot 10^{10} \frac{N}{m^2}$ is used (Stein and Wyssession, 2003) and an average seismogenic depth of $d = 30$ km is assumed. Included data are *CMT*-solutions and focal mechanisms determined in this work as used in chapter 7 for a time period of $t = 21$ a (1985–2005, Table A.1 and A.4). Additional mechanisms before 1985 as used for stress inversion were not included, since they only cover single events that cannot provide a complete dataset for this time period.

Table 7.2 summarises the results of the calculations. Averaged for the western rift branch (areas 3-6) the rate is $v_T = 0.34$ mm/a and for the eastern branch including Kenya Rift and Davie Ridge $v_T = 0.08$ mm/a (areas 7b and 9a). This agrees with the trend calculated by Calais et al. (2006), that also shows smaller rates v_T on the eastern than on the western rift branch but with higher absolute values. All but one extension rate are below 1 mm/a and thus clearly lower than determined by other methods. Only the Lake Tanganyika area produced a higher rate of $v_T = 1.2$ mm/a. This is mainly due the 2005-12-05 M_W 6.8 earthquake (Table A.4) with a seismic moment of $m_0 = 20 \cdot 10^{18}$ Nm, that is 81% of the cumulative amount for area 5 and illustrates the influence of large events on the estimation of extension rates.

Hence, one reason for the low extension rates is the short time period that does not represent one seismic cycle. For a more reliable determination of homogeneous deformation, the seismicity over at least one seismic cycle must be averaged including major events $M_W \geq 7.0$, that in eastern Africa occur on average twice or three times per one hundred years (compare Fig. 5.6). Actually, such an earthquake occurred on 2006-02-22 in Mozambique on the southern end of the active *EARS* with a magnitude of M_W 7.0 ($m_0 = 42 \cdot 10^{18}$ Nm). Included in the estimation of the total seismic strain for eastern Africa, this would result in a nearly doubled extension rate of $v_T = 0.46$ mm/a (compare Table 7.2). This value is a little overestimated, since only 21 years are considered, but nevertheless it gives an idea of the total amount of seismic extension. A negligible reason for low extension rates is the incompleteness of the focal mechanism dataset for small magnitudes, since the seismic moment m_0 decreases by a factor of $10^{1.5}$ per magnitude (eqn. 2.22), while the number of events increases only with a factor of 10 (eqn. 5.1).

Beside the incompleteness of the seismic cycle, the principal explanation for the underestimated extension rates is most likely aseismic deformation in terms of silent earthquakes or fault creeping, that cannot be detected by the global seismic network directly. Especially for the characteristic continental rifting of the eastern branch, aseismic deformation dominates the extension, due to a thinned crust and increased high flow of 100–150 mW/m² that is accompanied by recent volcanics (Sobolev and Rundquist, 1999).

Chapter 8

Discussion of the eastern African stress field

The final stress inversion is performed in ten separate areas (section 7.2, Fig. 7.4) and reveals a general trend of east/west extension. Moreover, from northwest to southeast a smooth rotation from west-northwest/east-southeast to east-northeast/west-southwest extension is visible.

The quality of the moment tensor inversion depends mainly on the number of independent data. However, some areas defined for the stress analysis contain only a low number of earthquake source mechanisms because of their distinct location (areas 1 and 2) or because of the subdivision of a larger area that shows systematically changing stress orientations (area 7b). These small datasets are consistent and stress inversions consequently result in very low misfit angles $\bar{\beta}$ between calculated direction of maximum shear stress and data slip vector (see Table 7.1). Nevertheless, the inversion results can give a rough estimation of the local first-order stress pattern. Especially the obtained stress orientation for area 2 (located at the Aswa fault-zone) is an interesting piece of information, since the area is distinct from others and clearly shows a north-south oriented S_h . Since all included mechanisms result from the Sudan 1990-05-20 M_W 7.1 earthquake and its aftershocks, the local stress pattern of this area differs from the general east/west trend of S_h . Whereas the mainshock was a pure left-lateral strike-slip mechanism striking northwest/southeast (Gaulon et al., 1992), all additional events included in area 2 show normal faulting with nodal planes roughly striking east/west. The orientation of T-axes does not differ between main- and aftershocks and thus no indication for a change of stress orientation is observed. However, the changing mechanism may be an indicator for pull-apart structures aside of the main Aswa fault-zone. The area in western Kenya between the eastern rift branch and Lake Victoria (area 7a) is worst resolved by stress inversion. Even though the amount of data is small (eight focal mechanisms), $\bar{\beta}$ is very high and hence the reliability of the inverted stress field of area 7a is rather low.

A higher amount of data and a good fit of slip vectors are given for the inversions of areas

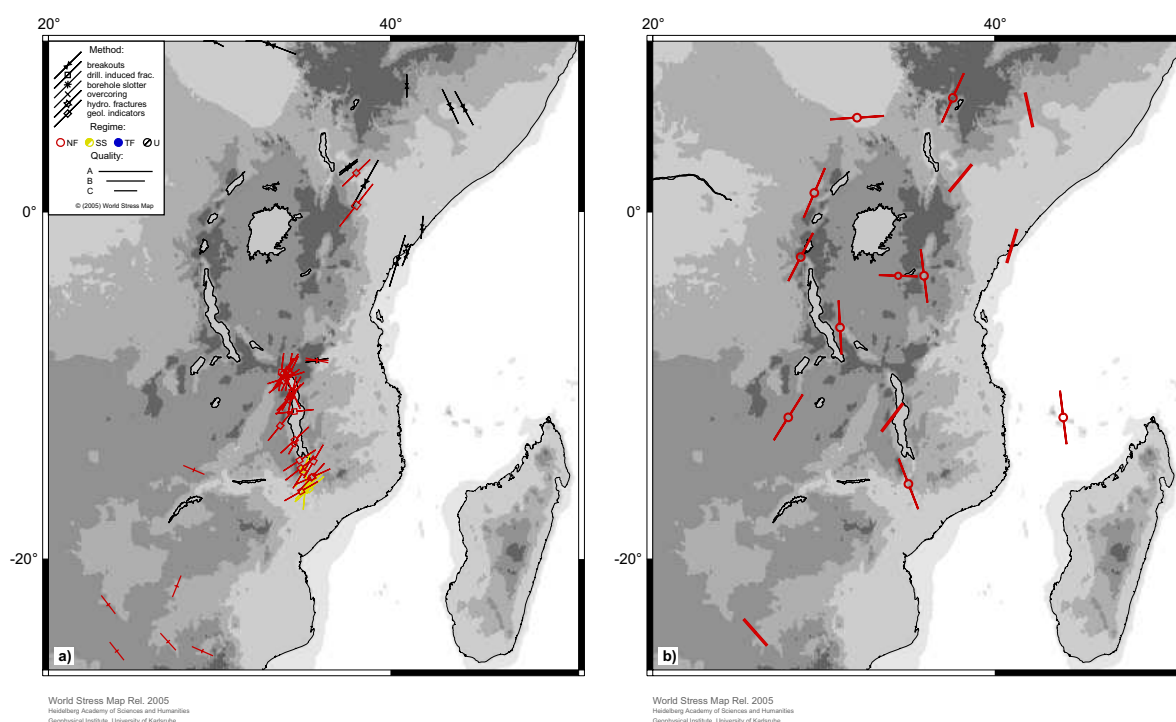


Figure 8.1: a) Orientation of maximum horizontal stress S_H of the *WSM*-database for stress indicators other than focal mechanism solutions (Reinecker et al., 2005). Coloured symbols are related to stress regimes. Details about regime, quality and type of data see legend. b) Orientation of maximum horizontal stress S_H from stress inversion in this work (Fig. 7.4) and averaged *WSM*-data. Results of the stress inversions are plotted in the centre of the inverted areas (lines with circle). Only other information than focal mechanism data of the *WSM*-database are averaged for selected locations with at least three data points inside a radius of 350 km (lines without circle).

3–6 and 8, that result in a reliable state of stress all along the western rift branch and the region west of it. As shown in the section 7.2, S_h is oriented mostly 90° to the main fault and thus supports the assumption of a perpendicularly opening rift with no or only a small portion of oblique opening (Tiercelin et al., 1988). The inversion of the 18 widespread focal mechanisms in Zambia and southern Congo (area 8) shows a very low misfit angle and thus reveals a uniform stress field without the presence of dominant rift structures.

Area 9 (eastern continental margin) contains 27 focal mechanisms distributed over an area of around 2000 km length and thus a high $\bar{\beta}$ -value is the consequence of the stress inversion. However, the combination of areas 9a and 9b (Davie Ridge and Madagascar) is justified by the only slightly increased misfit angle $\bar{\beta}$ compared to the inversion of area 9a solely (Table 7.1). Hence the combined inversion shows a clear extensional regime. The Davie Ridge, which is located north of the Mozambique channel (Fig. 1.3) has an asymmetric shape with a steep flank in the west and a shallow side to the east and acts as a separation

between a thick sedimentary layer towards Mozambique and thinner sediments to the east (Lort et al., 1979). It developed during the Mesozoic opening of the Mozambique Channel as a transform fault (Schandelmeier et al., 2004), and even though it shows no morphological expression of a rift today, the dominating normal regime can be seen as a diffuse southward extension of the eastern rift branch (Mougenot et al., 1986; Grimison and Chen, 1988; Chu and Gordon, 1999).

The East African Rift System (*EARS*) divides the Nubian and Somalian subplate and can be seen as a plate boundary. After McKenzie (1969) pre-existing fault planes, which are present at plate boundaries, are planes of weakness that can be re-activated by various stress orientations (section 6.1). Thus, the derivation of stress can be erroneous, if one single earthquake source mechanism is used, since the pure deformation signal would be treated as stress. However, the stress inversion of several sources with different mechanisms is affected only to a minor degree by deformation and can be used to study stress orientations on plate boundaries (Hardebeck and Hauksson, 1999).

First-order stress pattern are a consequence of sub-lithospheric processes and plate boundary forces, that can partly be explained by gravitational potential energy as discussed by several authors for the African continent (Bott, 1982; Pavoni, 1992; Zoback, 1992b; Coblenz and Sandiford, 1994; Bird et al., 2006). Coblenz and Sandiford (1994) showed by two-dimensional finite element modelling of vertical columns with varying densities ($2^\circ \times 2^\circ$) that the large-scale extensional stress field can be explained by gravitational potential energy. Beside this, they modelled compressional stresses towards the oceanic ridges that surround Africa. One event analysed in this study (event 6) is located in the Indian ocean off-shore Somalia and shows a thrusting mechanism (paragraph 5.2.4) that supports the assumption of a change in regime. But in general, seismicity is very low in this area and thus a prevailing compressional state of stress can not be verified. The stress orientations computed in the study of Coblenz and Sandiford (1994) match the orientations of the presented stress inversions well in the western high plateau region (area 8) and roughly along the rift. However, their two-dimensional model cannot resolve a stress rotation as determined in this work, probably because the regional tectonics are mainly influenced by three-dimensional structures.

Figure 8.1a shows the stress data contained in the World Stress Map (*WSM*) database (Reinecker et al., 2005). Since in the presented work all focal mechanism solutions included in the *WSM*-dataset are analysed by formal stress inversion, individually deduced stress orientations from focal mechanisms are not plotted. Thus, only a few stress indicators remain for the comparison with the results of this study. Beside some overcoring data south of 20°S , where no focal mechanisms are known, borehole breakouts and data from geological field observations are available.

The set of geological data along Lake Malawi results from one single field study and does not agree with the stress inversion results of area 6 (Lake Malawi, Fig. 8.1a,b). The data originates to Chorowicz and Sorlien (1992) who performed a fault-slip analysis, that was mainly done by striation and groove measurements on Precambrian (older than 540 Ma)

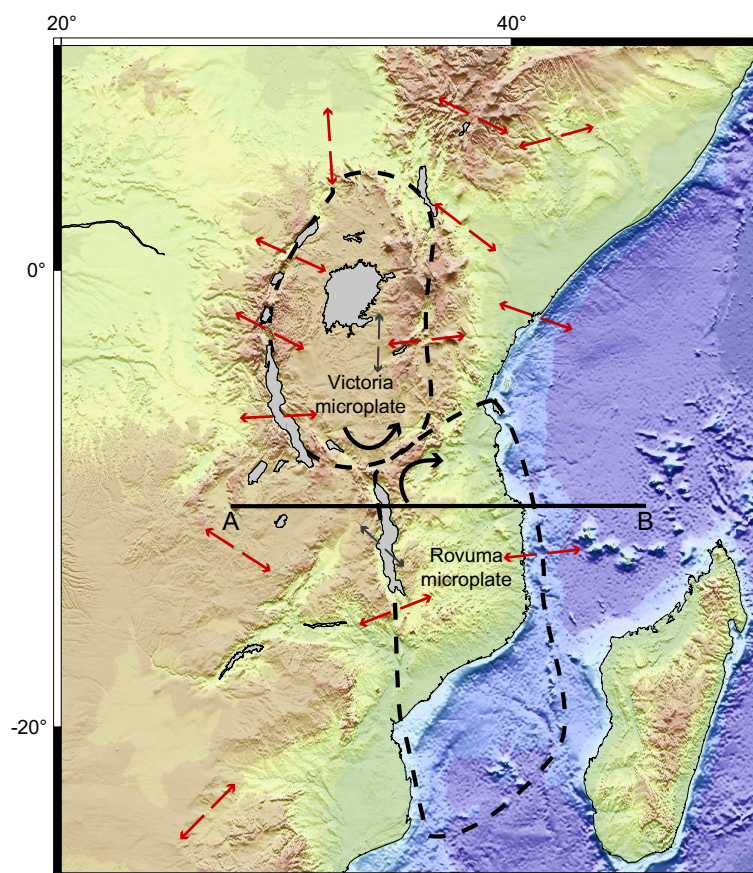


Figure 8.2: Proposed tectonic setting of eastern Africa including the Victoria and Rovuma microplate (dashed lines) with direction of rotation (black arrows, Calais et al., 2006). Pairs of arrows show orientations of extensions (this study and WSM). Red arrows indicate reliable data, grey coloured arrows less reliable data (details see chapter 8). The solid line gives the location of cross-section in Figure 8.3.

and Karroo rocks (160–300 Ma). These slip indicators can be caused by seismicity of recent times, but also ancient tectonic processes could have imprinted these marks (e.g. Meschede, 1994). Chorowicz and Sorlien (1992) associated the measurements with recent tectonics and derived a northeast/southwest oriented maximum horizontal stress S_H . They described the disagreement with slip directions of *CMT*-solutions—that are part of the inversion in this work (e.g. 1989-03-10, M_W 6.2, see Table A.4)—but provided no explanation for the contradiction to their own data. In this work 14 focal mechanisms constrain the orientation of maximum horizontal stress S_H along Lake Malawi to north-northwest/south-southeast. Even though $\bar{\beta} = 17^\circ \pm 27^\circ$ and hence the misfit is of medium size, the majority of the individual focal mechanisms agree with the computed orientations of S_H , but contradicts the fault-slip analysis of Chorowicz and Sorlien (1992) in orientation and slip direction. Finally, it cannot be clarified whether the striations provide information on young slip orientations

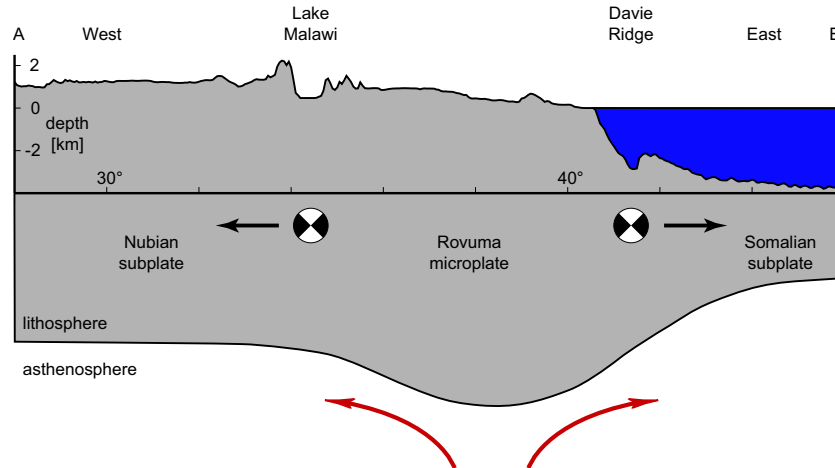


Figure 8.3: Schematic east-west profile across the southern *EARS* at 10.5°S (see Fig. 8.2). The topography (inflated) shows the Malawi Rift in the southern part of the western rift branch and the re-activated Davie Ridge. Stereotype beachballs are displayed in sectional view and indicate normal faulting. Mantle flow (red arrows) could trigger the rifting process around the proposed Rovuma microplate (Calais et al., 2006).

or if they originate from much older processes. However, the source mechanisms provide consistent data that directly express the first-order tectonics of a large area along the rift with rupture planes of several tens of kilometres length.

Compared to the other stress data of the *WSM*, the orientations resulting from stress inversion agree as far as they are in neighbouring regions. The averaging of individual stress indicators (Müller et al., 2003) provides a valuable tool for comparing *WSM* stress data with inversion results (Fig. 8.1b). Only in the northeastern part of the study area three averaged stress orientations are adjacent to inversion areas of this work. These stress orientations from borehole breakouts and two geological indicators partly support the counter-clockwise stress rotation of S_h from northwest to southeast.

North of the study region the Afar triple junction is located, where the *EARS* meets the spreading centres of the Red Sea and the Gulf of Aden. The Afar region showed seismic and volcanic activity in 2005 with 163 earthquakes $M_W \geq 3.9$ and volcanic eruptions with up to 8 m of opening (Wright et al., 2006). Hagos (2006) performed stress inversions of focal mechanisms and distinguishes two different extensional regimes. In the eastern Afar region S_h is parallel to the opening of the Gulf of Aden (north-northeast/south-southwest). In the western part however, S_h is oriented in east-northeast/west-southwest direction, that is between the orientations in the Red Sea in the north (S_h north-northeast/south-southwest, Hagos, 2006) and the Main Ethiopian Rift in the south (S_h east-southeast/west-northwest, this study). Hence, the Afar triple junction is dominated by local tectonics and the discussed large-scale stress rotation is present only south of it.

This systematic change in stress orientation is possibly connected to existing microplates. Calais et al. (2006) observed deviations in the direction of motion of microplates in eastern Africa. By *GPS*- and earthquake slip-data from *CMT*-solutions they concluded that the *EARS* rather consists of at least two distinct microplates named Victoria and Rovuma, instead of representing a diffuse zone of rifting (Hartnady, 2002). The Victoria block is located around Lake Victoria south of the Aswa fault-zone between the eastern and western rift branch. The Rovuma block between the Lake Malawi and the Davie Ridge borders in the north on the Victoria block but shows no clear seismic margin, possibly due to aseismic deformation (Fig. 8.2, compare section 7.3). An opposite rotation of these two microplates (Victoria counter-clockwise, Rovuma clockwise), as proposed by Calais et al. (2006), agrees with the results of the stress inversion of this work. Since both studies use among others *CMT*-data, variations in their results coincide locally. Nevertheless, the existence of the two microplates would explain the spatially changing stress field.

So the rifting of the African plate between the Nubian and Somalian subplate possibly has been initialised by an up-welling mantle plume that caused a general uplift of eastern Africa (Green et al., 1991; Nyblade et al., 2000). As a consequence of the gravitational potential energy of the created high plateaus, the continent has broken up around pre-existing cratonic blocks (Victoria and Rovuma microplate). This process is probably still triggered by mantle up-wellings that could cause the specific rotation of the Victoria microplate and the re-activation of the Davie-Ridge as a spreading centre on the eastern boundary of the Rovuma microplate (Fig. 8.3).

Part III

Conclusions

Chapter 9

Summary

The determination of earthquake focal mechanisms in regions of intermediate seismicity provides valuable data for the derivation of regional stress and thus the understanding of recent tectonics. The aim of this study was to analyse the applicability of focal mechanism determination to light and intermediate magnitude earthquakes in intraplate regions of intermediate seismicity by moment tensor inversion (Giardini, 1992). For the case study of eastern Africa I determined 38 focal mechanisms with $M_W = 4.4$ – 5.5 for source-receiver distances up to 3300 km.

The investigation of focal mechanisms of light and intermediate magnitude earthquakes calculated from sparse teleseismic waveform data reveals a strong dependence on the inverted frequency pass-band. To take into account this dependence, I developed an iterative and frequency sensitive processing to perform the moment tensor inversion. This semi-automatic procedure determines a dataset of high quality waveform data, the maximum width frequency pass-band of similar and low variance moment tensors and the hypocentral depth. Thus, all determined moment tensors have low variances and are stable within the finally inverted frequency band.

I inverted only waveforms with periods longer than 35 s that are less affected by structural heterogeneities than short period waves, since a one-dimensional velocity model (PREM, Dziewonski and Anderson, 1981) is used for calculating the synthetic waveforms. To determine the waveform dataset for the inversion, I defined variance limits to exclude waveforms that have a low signal-to-noise ratio or that are inconsistent with other data. In general six waveform traces proved to be sufficient to perform a stable moment tensor inversion. I applied a singular value decomposition *SVD* to study the reliability of the inversion results. It revealed, that for focal mechanism solutions with a low percentage of double couple—which can be due to mismodelled data—cutting off the highest order eigenvector does not change the double couple part of the moment tensor severely. Thus inconsistent data do hardly affect the determined double couple focal mechanism.

By using the frequency sensitive moment tensor inversion in eastern Africa I was able to lower the level of completeness of moment tensors from $M_W \approx 5.3$ to $M_W \approx 5.0$. Further-

more, I gained moment tensors for 27 events with $M_W = 4.4\text{--}5.0$, but for some reported events $m_b < 5.0$ I could not determine the source mechanism, since sufficient waveform data are not available. Including a regional velocity model would extend the inversion method to higher frequencies and hence could lower the magnitude threshold for moment tensor determination.

The formal stress inversion of groups of focal mechanism solutions (Michael, 1984) allows to derive the stress pattern of eastern Africa. Hence I determined the tectonic regimes and the orientations of minimum horizontal stress S_h . The separate inversion for ten distinct areas results in a prevailing extensional stress regime in eastern Africa with predominantly east/west oriented S_h . Beyond this, the orientation of S_h rotates from west-northwest/east-southeast in the northwest to east-northeast/west-southwest in the southwest of the study region.

This systematic change of stress orientation can be explained by the microplates Victoria and Rovuma, that are located between the Nubian and Somalian subplate. Hence, the influence of local mantle up-wellings could be the reason for the spatial changes in the stress field around these microplates and their opposite rotation, as constrained by *GPS*-data (Calais et al., 2006). Beyond this, persistent mantle flow could be responsible for the re-activation of the Davie Ridge as a spreading centre at the eastern bound of the Rovuma microplate.

I analysed the cumulative strain on the western and eastern rift branch of the *EARS*, released by seismic activity and found only low rates of horizontal extension. The total amount of seismic extension is ~ 0.4 mm/a, that is lower than calculations based on *GPS*-data. This a hint for the presence of aseismic deformation and possibly the reason for low seismicity on the boundaries of the proposed microplates. Since recent two-dimensional finite element models (Coblentz and Sandiford, 1994; Bird et al., 2006) cannot take account of the discussed regional features, three-dimensional modelling approaches are necessary to explain the change of stress, while additional *GPS*-measurements are necessary to verify the existence of the Victoria and Rovuma microplate.

I have shown that even with a sparse teleseismic station distribution moment tensor inversion of earthquakes with $M_W \leq 5.0$ is possible. By using a one-dimensional earth model and waveform data of the permanent global seismometer network, the described processing is easily transferable to other regions of intermediate seismicity. Thus frequency sensitive moment tensor inversion has a high potential of enlarging the number of calculated focal mechanism solutions worldwide to improve the understanding of regional tectonics.

Bibliography

- Ambraseys, N. N. and Adams, R. D. (1992). Reappraisal of major African earthquakes, south of 20-degrees-N, 1900-1930. *Tectonophysics*, 209(1-4):293–296.
- Anderson, D. L. and Hart, R. S. (1978). Attenuation models of the earth. *Phys. Earth Planet. Int.*, 16(4):289–306.
- Angelier, J. (1979). Determination of the mean principal directions of stresses for a given fault population. *Tectonophysics*, 56(3-4):T17–T26.
- Angelier, J. (2002). Inversion of earthquake focal mechanisms to obtain the seismotectonic stress IV - a new method free of choice among the nodal planes. *Geophys. J. Int.*, 150(3):588–609.
- Arvidsson, R. and Ekström, G. (1998). Global CMT analysis of moderate earthquakes, $M_w \geq 4.5$, using intermediate-period surface waves. *Bull. Seism. Soc. Am.*, 88(4):1003–1013.
- Atkinson, G. M. and Boore, D. M. (1998). Evaluation of models for earthquake source spectra in eastern North America. *Bull. Seism. Soc. Am.*, 88(4):917–934.
- Ayele, A. (2002). Active compressional tectonics in central Africa and implications for plate tectonic models: Evidence from fault mechanism studies of the 1998 earthquakes in the Congo Basin. *J. Afr. Earth Sci.*, 35:45–50.
- Backus, G. E. (1977). Interpreting seismic glut moments of total degree 2 or less. *Geophys. J. Roy. Astr. Soc.*, 51(1):1–25.
- Barruol, G. and Ismail, W. B. (2001). Upper mantle anisotropy beneath the African IRIS and Geoscope stations. *Geophys. J. Int.*, 146(2):549–561.
- Bernardi, F., Braunmiller, J., Kradolfer, U., and Giardini, D. (2004). Automatic regional moment tensor inversion in the European-Mediterranean region. *Geophys. J. Int.*, 157:703–716.
- Bird, P. (2003). An updated digital model of plate boundaries. *Geochem. Geophys. Geosy.*, 4:1027.

- Bird, P., Ben-Avraham, Z., Schubert, G., Andreoli, M., and Viola, G. (2006). Patterns of stress and strain rate in southern Africa. *J. Geophys. Res.*, 111(B8):B08402.
- Bott, M. H. P. (1959). The mechanics of oblique slip faulting. *Geol. Mag.*, 96(2):109–117.
- Bott, M. H. P. (1982). The mechanism of continental splitting. *Tectonophysics*, 81(3–4):301–309.
- Braunmiller, J., Kradolfer, U., Baer, M., and Giardini, D. (2002). Regional moment tensor determination in the European-Mediterranean area - initial results. *Tectonophysics*, 356:5–22.
- Brazier, R. A., Nyblade, A. A., and Florentin, J. (2005). Focal mechanisms and the stress regime in NE and SW Tanzania, East Africa. *Geophys. Res. Lett.*, 32:L14315.
- Calais, E., Hartnady, C., Ebinger, C., and Nocquet, J. M. (2006). Kinematics of the East African Rift from GPS and earthquake slip vector data. In Yirgu, G., Ebinger, C. J., and Maguire, P. K. H., editors, *Structure and Evolution of the Rift Systems within the Afar volcanic province, Northeast Africa*, volume 259, pages 9–22. Geol. Soc. Lond. Spec. Publ.
- Chorowicz, J. and Sorlien, C. (1992). Oblique extensional tectonics in the Malawi Rift, Africa. *Geol. Soc. Am. Bull.*, 104(8):1015–1023.
- Chu, D. and Gordon, R. G. (1999). Evidence for motion between Nubia and Somalia along the Southwest Indian ridge. *Nature*, 398(6722):64–67.
- Coblentz, D. D. and Sandiford, M. (1994). Tectonic stresses in the African plate: Constraints on the ambient lithospheric stress state. *Geology*, 22:831–834.
- Dahlen, F. A. and Tromp, J. (1998). *Theoretical Global Seismology*. Princeton, NJ, USA. Princeton University Press, Princeton, New Jersey.
- Dziewonski, A. M. and Anderson, D. L. (1981). Preliminary reference earth model. *Phys. Earth Planet. Int.*, 25(4):297–356.
- Dziewonski, A. M., Chou, T. A., and Woodhouse, J. H. (1981). Determination of earthquake source parameters from waveform data for studies of global and regional seismicity. *J. Geophys. Res.*, 86(NB4):2825–2852.
- Dziewonski, A. M., Ekström, G., Franzen, J. E., and Woodhouse, J. H. (1987a). Centroid-moment tensor solutions for January–March 1986. *Phys. Earth Planet. Int.*, 45(1):1–10.
- Dziewonski, A. M., Ekström, G., Franzen, J. E., and Woodhouse, J. H. (1987b). Global seismicity of 1977: Centroid-moment tensor solutions for 471 earthquakes. *Phys. Earth Planet. Int.*, 45(1):11–36.

- Dziewonski, A. M., Ekstrom, G., and Maternovskaya, N. N. (2003). Centroid-moment tensor solutions for October-December 2000. *Phys. Earth Planet. Int.*, 136(3-4):145–163.
- Ekström, G., Dziewonski, A. M., Maternovskaya, N. N., and Nettles, M. (2005). Global seismicity of 2002: Centroid-moment-tensor solutions for 1034 earthquakes. *Phys. Earth Planet. Int.*, 148(2-4):303–326.
- Ekström, G., Tromp, J., and Larson, E. W. F. (1997). Measurements and global models of surface wave propagation. *J. Geophys. Res.*, 102(B4):8137–8157.
- Engdahl, E. R., van der Hilst, R., and Buland, R. (1998). Global teleseismic earthquake relocation with improved travel times and procedures for depth determination. *Bull. Seism. Soc. Am.*, 88(3):722–743.
- Fairhead, J. and Stuart, G. (1982). The seismicity of the East African Rift system and comparison with other continental rifts. In Palmason, G., editor, *Continental and Oceanic Rifts, Geodynamics Series Vol. 8*, pages 41–61. AGU/GSA, Washington DC, USA.
- Fairhead, J. D. and Girdler, R. W. (1971). Seismicity of Africa. *Geophys. J. Roy. Astr. Soc.*, 24(3):271–301.
- Fan, G. and Wallace, T. (1991). The determination of source parameters for small earthquakes from a single, very broadband seismic station. *Geophys. Res. Lett.*, 18(8):1385–1388.
- Ferdinand, R. W. and Arvidsson, R. (2002). The determination of source mechanisms of small earthquakes and revised models of local crustal structure by moment tensor inversion. *Geophys. J. Int.*, 151:221–234.
- Fernandes, R. M. S., Ambrosius, B. A. C., Noomen, R., Bastos, L., Combrinck, L., Miranda, J. M., and Spakman, W. (2004). Angular velocities of Nubia and Somalia from continuous GPS data: Implications on present-day relative kinematics. *Earth Planet. Sci. Lett.*, 222(1):197–208.
- Flinn, E. A., Engdahl, E. R., and Hill, A. R. (1974). Seismic and geographical regionalization. *Bull. Seism. Soc. Am.*, 64(3-2):771–992.
- Forbriger, T. (2001). Notizen zur Vorlesung „Inversionstheorie“. Skriptum.
- Foster, A. N. and Jackson, J. A. (1998). Source parameters of large African earthquakes: Implications for crustal rheology and regional kinematics. *Geophys. J. Int.*, 134:422–448.
- Franklin, W. R. (2003). PNPOLY - point inclusion in polygon test. Web page. http://www.ecse.rpi.edu/Homepages/wrf/Research/Short_Notes/pnpoly.html.
- Frohlich, C. (1994). Earthquakes with non-double-couple mechanisms. *Science*, 264(5160):804–809.

- Frohlich, C. (1995). Characteristics of well-determined non-double-couple earthquakes in the Harvard CMT catalog. *Phys. Earth Planet. Int.*, 91(4):213–228.
- Gaulon, R., Chorowicz, J., Vidal, G., Romanowicz, B., and Rault, G. (1992). Regional geodynamic implications of the May July 1990 earthquake sequence in southern Sudan. *Tectonophysics*, 209(1-4):87–103.
- Gephart, J. W. and Forsyth, D. W. (1984). An improved method for determining the regional stress tensor using earthquake focal mechanism data: Application to the San Fernando earthquake sequence. *J. Geophys. Res.*, 89(B11):9305–9320.
- Giardini, D. (1984). Systematic analysis of deep seismicity - 200 centroid-moment tensor solutions for earthquakes between 1977 and 1980. *Geophys. J. Roy. Astr. Soc.*, 77(3):883–914.
- Giardini, D. (1988). Frequency-distribution and quantification of deep earthquakes. *J. Geophys. Res.*, 93(B3):2095–2105.
- Giardini, D. (1992). Moment tensor inversion from mednet data - large worldwide earthquakes of 1990. *Geophys. Res. Lett.*, 19(7):713–716.
- Giardini, D. (1999). The global seismic hazard assessment program (GSHAP)1992/1999. *Ann. Geofis.*, 42(6):957–974.
- Giardini, D., Boschi, E., and Palombo, B. (1993). Moment tensor inversion from mednet data - regional earthquakes of the mediterranean. *Geophys. Res. Lett.*, 20(4):273–276.
- Green, W., Achauer, U., and Meyer, R. P. (1991). A three-dimensional seismic image of the crust and upper mantle beneath. *Nature*, 354(6350):199–203.
- Grimison, N. L. and Chen, W. P. (1988). Earthquakes in the Davie Ridge Madagascar region and the southern Nubian Somalian plate boundary. *J. Geophys. Res.*, 93(B9):10439–10450.
- Grünthal, G., Bosse, C., Sellami, S., Mayer-Rosa, D., and Giardini, D. (1999). Compilation of the GSHAP regional seismic hazard for Europe, Africa and the Middle East. *Ann. Geofis.*, 42(6):1215–1223.
- Gutenberg, B. and Richter, C. F. (1954). *Seismicity of the earth and associated phenomena*. Princeton Univ. Press, Princeton, NJ, USA.
- Hagos, L. Z. (2006). *Earthquake Sources, the Stress Field and Seismic Hazard: A Study in Eritrea and its Surrounding*. PhD thesis, Uppsala University.
- Hanks, T. C. and Kanamori, H. (1979). Moment magnitude scale. *J. Geophys. Res.*, 84(NB5):2348–2350.

- Hardebeck, J. L. and Hauksson, E. (1999). Role of fluids in faulting inferred from stress field signatures. *Science*, 285(5425):236–239.
- Hartnady, C. J. H. (1990). Seismicity and plate boundary evolution in southeastern Africa. *S. Afr. J. Sci.*, 93(3):473–484.
- Hartnady, C. J. H. (2002). Earthquake hazard in Africa: Werspectives on the Nubia-Somalia boundary. *S. Afr. J. Sci.*, 98:425–428.
- Heidbach, O., Barth, A., Connolly, P., Fuchs, K., Müller, B., Tingay, M., Reinecker, J., Sperner, B., and Wenzel, F. (2004). Stress maps in a minute: The 2004 World Stress Map release. *Eos, Trans. AGU*, 85(49):521.
- Heidbach, O., Barth, A., Müller, B., Reinecker, J., Sperner, B., and Tingay, M. (2005). World Stress Map release 2005 - stress orientations from single focal mechanisms at plate boundaries. *Eos Trans. AGU*, 86(52). Fall Meet. Suppl., Abstract T21C-0500.
- Henry, C., Woodhouse, J. H., and Das, S. (2002). Stability of earthquake moment tensor inversions: Effect of the double-couple constraint. *Tectonophysics*, 356(1-3):115–124.
- Horner-Johnson, B. C., Gordon, R. G., Cowles, S. M., and Argus, D. F. (2005). The angular velocity of Nubia relative to Somalia and the location of the Nubia-Somalia-Antarctica triple junction. *Geophys. J. Int.*, 162:221–238.
- Ide, S. (2001). Complex source processes and the interaction of moderate earthquakes during the earthquake swarm in the Hida-Mountains, Japan, 1998. *Tectonophysics*, 334(1):35–54.
- Jackson, J. and McKenzie, D. (1988). The relationship between plate motions and seismic moment tensors, and the rates of active deformation in the Mediterranean and Middle-East. *Geophys. J. Roy. Astr. Soc.*, 93(1):45–73.
- Jost, M. L. and Hermann, R. B. (1989). A student’s guide to and review of moment tensors. *Seism. Res. Lett.*, 60(2):37–57.
- Kafka, A. L. and Weidner, D. J. (1979). The focal mechanisms and depths of small earthquakes as determined from Rayleigh-wave radiation patterns. *Bull. Seism. Soc. Am.*, 69(5):1379–1390.
- Kawakatsu, H. (1996). Observability of the isotropic component of a moment tensor. *Geophys. J. Int.*, 126(2):525–544.
- Kennett, B. L. N. (1976). The inversion of surface wave data. *Pure Appl. Geophys.*, 114(5):747–751.
- Kim, S. G. and Kraeva, N. (1999). Source parameter determination of local earthquakes in Korea using moment tensor inversion of single station data. *Bull. Seism. Soc. Am.*, 89(4):1077–1082.

- Kostrov, V. V. (1974). Seismic moment and energy of earthquakes, and seismic flow of rocks. *Izv. Acad. Sci. USSR Phys. Solid Earth*, 1:23–44. Eng. Transl.
- Kreemer, C., Holt, W. E., and Haines, A. J. (2003). An integrated global model of present-day plate motions and plate boundary deformation. *Geophys. J. Int.*, 154(1):8–34.
- Kuge, K. and Lay, T. (1994). Data-dependent non-double-couple components of shallow earthquake source mechanisms: Effects of wave-form inversion instability. *Geophys. Res. Lett.*, 21(1):9–12.
- Larson, E. W. F. and Ekström, G. (2001). Global models of surface wave group velocity. *Pure Appl. Geophys.*, V158(8):1377–1399.
- Lemaux, J. I., Gordon, R. G., and Royer, J.-Y. (2002). Location of the Nubia-Somalia boundary along the Southwest Indian Ridge. *Geology*, 30(4):339–342.
- Lort, J. M., Limond, W. Q., Segoufin, J., Patriat, P., Delteil, J. R., and Damotte, B. (1979). New seismic data in the Mozambique Channel. *Mar. Geophys. Res.*, 4(1):71–89.
- McKenzie, D. P. (1969). The relation between fault plane solutions for earthquakes and the directions of the principal stress. *Bull. Seism. Soc. Am.*, 59(2):591–601.
- Meschede, M. (1994). *Methoden der Strukturgeologie*. Ferdinand Enke Verlag, Stuttgart.
- Michael, A. J. (1984). Determination of stress from slip data: Faults and folds. *J. Geophys. Res.*, 89(B13):11,517–11,526.
- Michael, A. J. (1987a). Stress rotation during the coalinga aftershock sequence. *J. Geophys. Res.*, 92(B8):7963–7979.
- Michael, A. J. (1987b). Use of focal mechanisms to determine stress: A control study. *J. Geophys. Res.*, 92(B1):357–368.
- Midzi, V., Hlatywayo, D. J. and Chapola, L. S., Kebede, F., Atakan, K., Lombe, D. K., Turyomurugyendo, G., and Tugume, F. A. (1999). Seismic hazard assessment in eastern and southern Africa. *Ann. Geofis.*, 42:1067–1083.
- Mougenot, D., Recq, M., Virlogeux, P., and Lepvrier, C. (1986). Seaward extension of the East-African rift. *Nature*, 321(6070):599–603.
- Müller, B., Wehrle, V., Hettel, S., Sperner, B., and Fuchs, K. (2003). A new method for smoothing oriented data and its application to stress data. In Ameen, M., editor, *Fracture and in-situ stress characterisation of hydrocarbon reservoirs*, volume 209, pages 107–126. Geol. Soc. Lond. Spec. Publ.

- Murphy, J. R. and McLaughlin, K. L. (1998). Comment on "Empirical determination of depth-distance corrections for m(b) and M-w from Global Seismograph Network stations" by Guust Nolet, Steve Krueger and Robert M. Clouser. *Geophys. Res. Lett.*, 25(23):4269–4270.
- Nyblade, A. A. and Langston, C. A. (1995). East-African earthquakes below 20-km depth and their implications for crustal structure. *Geophys. J. Int.*, 121(1):49–62.
- Nyblade, A. A., Owens, T. J., Gurrola, H., Ritsema, J., and Langston, C. A. (2000). Seismic evidence for a deep upper mantle thermal anomaly beneath east Africa. *Geology*, 28(7):599–602.
- Parker, R. L. (1994). *Geophysical inverse theory*. Princeton Univ. Press, Princeton, NJ, USA.
- Pavoni, N. (1992). Rifting of Africa and pattern of mantle convection beneath the African plate. *Tectonophysics*, 215(1-2):35–53.
- Pinar, A., Kuge, K., and Honkura, Y. (2003). Moment tensor inversion of recent small to moderate sized earthquakes: Implications for seismic hazard and active tectonics beneath the Sea of Marmara. *Geophys. J. Int.*, 153:133–145.
- Ranalli, G. (1995). *Rheology of the earth*. Chapman & Hall, 2. ed. edition.
- Rao, N. P., Tsukuda, T., Kosuga, M., Bhatia, S. C., and Suresh, G. (2002). Deep lower crustal earthquakes in central India: Inferences from analysis of regional broadband data of the 1997 May 21, Jabalpur earthquake. *Geophys. J. Int.*, 148:132–138.
- Reches, Z. (1987). Determination of the tectonic stress tensor from slip along faults that obey the coulomb yield condition. *Tectonics*, 6(6):849–861.
- Reinecker, J., Heidbach, O., Tingay, M., Sperner, B., and Müller, B. (2005). The release 2005 of the World Stress Map (available online at <http://www.world-stress-map.org>).
- Rezapour, M. (2003). Empirical global depth-distance correction terms for mb determination based on seismic moment. *Bull. Seism. Soc. Am.*, 93(1):172–189.
- Rivera, L. and Cisternas, A. (1990). Stress tensor and fault plane solutions for a population of earthquakes. *Bull. Seism. Soc. Am.*, 80(3):600–614.
- Ruff, L. J. (2004). Limits of the seismogenic zone. In Karner, G., Taylor, B., Driscoll, N. W., and Kohlstedt, D. L., editors, *Rheology and Deformation of the Lithosphere at Continental Margins*, MARGINS Theoretical and Experimental Earth Science Series, pages 138–165. Columbia University Press, New York.
- Schandelmeier, H., Bremer, F., and Holl, H.-G. (2004). Kinematic evolution of the Morondava rift basin of SW Madagascar - from wrench tectonics to normal extension. *J. Afr. Earth Sci.*, 38:321–330.

- Shudofsky, G. N. (1985). Source mechanisms and focal depths of East African earthquakes using Rayleigh-wave inversion and body-wave modelling. *Geophys. J. Roy. Astr. Soc.*, 83:563–614.
- Sipkin, S. A. (2003). A correction to body-wave magnitude mb based on moment magnitude Mw. *Seism. Res. Lett.*, 74:739–742.
- Sipkin, S. A., Bufe, C. G., and Zirbes, M. D. (2002). Moment-tensor solutions estimated using optimal filter theory: Global seismicity, 2000. *Phys. Earth Planet. Int.*, 130(1-2):129–142.
- Skobelev, S. e. a. (2004). Active faults in Africa: A review. *Tectonophysics*, 380:131–137.
- Sobolev, P. O. and Rundquist, D. V. (1999). Seismicity of oceanic and continental rifts: a geodynamic approach. *Phys. Earth Planet. Int.*, 111(3-4):253–266.
- Sorrells, G. G. (1971). Preliminary investigation into relationship between long-period seismic noise and local fluctuations in atmospheric-pressure field. *Geophys. J. Roy. Astr. Soc.*, 26(1-4):71–82.
- Sorrells, G. G., McDonald, J. A., Herrin, E., and Der, Z. A. (1971). Earth motion caused by local atmospheric-pressure changes. *Geophys. J. Roy. Astr. Soc.*, 26(1-4):83–98.
- Stammler, K. (1993). SeismicHandler: Programmable multichannel data handler for interactive and automatic processing of seismological analyses. *Comp. Geosci.*, 19:135–140.
- Stein, S. and Wysession, M. (2003). *An introduction to seismology, earthquakes, and earth structure*. Blackwell Publishing, Malden, MA, USA.
- Stich, D., Ammon, C., and Morales, J. (2003). Moment tensor solutions for small and moderate earthquakes in the Ibero-Magrebh region. *J. Geophys. Res.*, 108(B3):1–20.
- Stutzmann, E., Roult, G., and Astiz, L. (2000). GEOSCOPE station noise levels. *Bull. Seism. Soc. Am.*, 90(3):690–701.
- Suleiman, A. S., Doser, D. I., and Yarwood, D. R. (1993). Source parameters of earthquakes along the coastal margin of West Africa and comparisons with earthquakes in other coastal margin settings. *Tectonophysics*, 222(1):79–91.
- Šílený, J. (2004). Regional moment tensor uncertainty due to mismodeling of the crust. *Tectonophysics*, 383:133–147.
- Tiercelin, J. J., Chorowicz, J., Bellon, H., Richert, J. P., Mwanbene, J. T., and Walgenwitz, F. (1988). East-African Rift System: Offset, age and tectonic significance of the Tanganyika-Rukwa-Malawi intracontinental transcurrent fault zone. *Tectonophysics*, 148(3-4):241–252.

- Twiss, R. J. and Unruh, J. R. (1998). Analysis of fault slip inversions: Do they constrain stress or strain rate? *J. Geophys. Res.*, 103(B6):12205–12222.
- Wessel, P. and Smith, W. H. F. (1998). New, improved version of Generic Mapping Tools released. *Eos, Trans. AGU*, 79:579pp.
- Woodhouse, J. H. (1988). The calculation of eigenfrequencies and eigenfunctions of the free oscillations of the earth and the sun. In Doornbos, D. J., editor, *Seismological Algorithms*, pages 321–370. Academic Press, London.
- Wright, T. J., Ebinger, C., Biggs, J., Ayele, A., Yirgu, G., Keir, D., and Stork, A. (2006). Magma-maintained rift segmentation at continental rupture in the 2005 Afar dyking episode. *Nature*, 442(7100):291–294.
- Zhang, J. and Lay, T. (1990). Effects of centroid location on determination of earthquake mechanisms using long-period surface waves. *Bull. Seism. Soc. Am.*, 80(5):1205–1231.
- Zoback, M. L. (1992a). First- and second-order patterns of stress in the lithosphere: The World Stress Map project. *J. Geophys. Res.*, 97(B8):11,703–11,728.
- Zoback, M. L. (1992b). Stress field constraints on intraplate seismicity in eastern North America. *J. Geophys. Res.*, 97:11761–11782.

List of Figures

| | | |
|-----|---|----|
| 1.1 | World Stress Map release 2005. | 2 |
| 1.2 | a) Number of <i>CMT</i> -solutions per year versus moment magnitude M_W since 1976. b) Global seismicity $M_W \geq 4.5$ since 1996, overlaid by plate-boundaries and <i>WSM</i> -data locations. c) Magnitude classes. | 4 |
| 1.3 | Topographic map of eastern Africa. | 5 |
| 1.4 | Seismicity of eastern Africa. | 6 |
| 2.1 | The nine force couples of the seismic moment tensor. | 16 |
| 2.2 | Definition of strike ϕ , dip δ and slip λ | 17 |
| 2.3 | Standard moment tensors and their beachball representation. | 19 |
| 3.1 | Seismic station distribution (red triangles) in eastern Africa and neighbouring regions. | 25 |
| 3.2 | Seismograms of the seismic event on 31 January 2001 (event 30). | 26 |
| 3.3 | STEP 1 and STEP 2 of the processing scheme of the frequency sensitive moment tensor inversion. | 28 |
| 3.4 | STEP 3 of the processing scheme of the frequency sensitive moment tensor inversion. | 29 |
| 4.1 | Result of the frequency sensitive moment tensor inversion showing the 38 determined focal mechanisms. | 34 |
| 4.2 | Vertical waveform components recorded of the 2000-01-04 earthquake. | 35 |
| 4.3 | Histogram of the individual moment tensor inversion for single waveform components of event 20. | 36 |
| 4.4 | Frequency sensitive moment tensor inversion for 8 mHz wide pass-bands and discrete hypocentral depths for event 20. a) Inversion of the initial dataset N_{init} (STEP 2). b) Inversion of the final dataset N_{final} (STEP 3A). | 37 |

List of Figures

| | | |
|-----|--|-----|
| 4.5 | Variance σ of focal mechanism solutions in dependence on hypocentral depth for event 20. | 38 |
| 4.6 | Final solution of the moment tensor inversion of event 20. | 39 |
| 5.1 | Statistical summary of the 38 moment tensor inversions showing the dependencies of the different parameters. | 42 |
| 5.2 | Moment tensor inversion for the 2000-10-02 earthquake. | 44 |
| 5.3 | Hypocentral depths of focal mechanism solutions in the Lake Tanganyika region. | 46 |
| 5.4 | Cumulative number of waveform components used for moment tensor inversion. | 50 |
| 5.5 | Singular value decomposition <i>SVD</i> of the 38 moment tensors calculated. . . | 53 |
| 5.6 | Number of determined moment tensors per magnitude. | 56 |
| 5.7 | Moment magnitude M_W of the inversion results versus body-wave magnitude m_b given by the Engdahl catalogue of relocated earthquakes. | 57 |
| 7.1 | Stress inversion for all 145 events and <i>GSHAP</i> -zonation of eastern Africa. . | 68 |
| 7.2 | Stress inversion of focal mechanisms within sub-areas arranged along the western rift branch. | 71 |
| 7.3 | Stress inversion for first zonation variant. | 72 |
| 7.4 | Stress inversion for final zonation. | 74 |
| 8.1 | a) Orientation of maximum horizontal stress S_H of the <i>WSM</i> -database. b) Orientation of maximum horizontal stress S_H from stress inversion in this work and averaged <i>WSM</i> -data. | 80 |
| 8.2 | Proposed tectonic setting of eastern Africa. | 82 |
| 8.3 | Schematic east-west profile across the southern <i>EARS</i> at 10.5°S. | 83 |
| C.1 | Schematic illustration of an arbitrary earthquake source volume. | 131 |

List of Tables

| | | |
|-----|---|-----|
| 3.1 | Seismic stations in eastern Africa and neighbouring regions. | 24 |
| 5.1 | Focal mechanism solutions for the 2000-10-02 Lake Tanganyika event. . . . | 45 |
| 7.1 | Stress inversion results for eastern Africa. | 70 |
| 7.2 | Average extension rates for the rift segments of the East African Rift. . . . | 76 |
| A.1 | Results of the frequency sensitive moment tensor inversion. | 106 |
| A.2 | <i>CMT</i> -solutions for eastern Africa 1994-2002. | 107 |
| A.3 | Earthquakes in eastern Africa 1994-2002 in the Engdahl catalogue. | 108 |
| A.4 | Focal mechanisms used for stress and strain calculation. | 109 |

Part IV

Appendices

Appendix A

Tables of earthquake locations and moment tensor inversion results

Table A.1: Results of the frequency sensitive moment tensor inversion.

| Nr | yr-mo-day | hr:min:s | Lat | Lon | D | M_{11} | M_{22} | M_{33} | M_{12} | M_{13} | M_{23} | M_0 | M_W | Str | Dip | Ra | Σ | p | σ | F_{final} |
|----|------------|------------|-------|------|----|----------|----------|----------|----------|----------|----------|--------|-------|-----|-----|------|----------|------|----------|-------------|
| 1 | 1995-04-27 | 02:32:21.0 | -12.6 | 42.5 | 25 | -0.45 | 0.69 | -0.24 | -0.46 | -0.91 | 0.4 | 1.25 | 4.7 | 283 | 30 | -24 | 6 | 95.8 | 0.43 | 18-29 |
| 2 | 1995-04-29 | 11:50:53.9 | -1.3 | 28.6 | 6 | -5.7 | -3.1 | 8.7 | -3.2 | -10 | 6.9 | 14.9 | 5.4 | 229 | 22 | -55 | 6 | 30.0 | 0.55 | 20-29 |
| 3 | 1995-07-20 | 05:08:28.4 | -12.4 | 41.5 | 18 | 1.2 | -0.27 | -0.97 | -3 | -1.1 | 2.9 | 4.44 | 5.0 | 174 | 48 | 160 | 6 | 60.2 | 0.19 | 19-29 |
| 4 | 1995-11-12 | 19:00:09.8 | -13.8 | 31.6 | 33 | -8.4 | 5.5 | 2.9 | 1.7 | 7.1 | 7.8 | 13 | 5.3 | 76 | 36 | -45 | 6 | 76.2 | 0.20 | 17-29 |
| 5 | 1995-12-08 | 23:40:51.8 | -4.6 | 38.8 | 18 | -2.3 | 1.6 | 0.69 | -0.24 | -1.4 | -1.5 | 2.91 | 4.9 | 102 | 43 | -128 | 8 | 84.8 | 0.47 | 19-29 |
| 6 | 1996-02-29 | 07:14:18.7 | -2.4 | 47.0 | 10 | -0.59 | -0.59 | -0.83 | -1.9 | -0.34 | -0.91 | 2.5 | 4.9 | 19 | 26 | 42 | 7 | 81.2 | 0.33 | 20-29 |
| 7 | 1996-08-30 | 06:58:45.2 | -15.4 | 34.1 | 10 | -0.44 | 0.022 | 0.41 | -0.33 | 0.36 | 0.041 | 0.651 | 4.5 | 21 | 27 | -46 | 9 | 57.0 | 0.36 | 21-29 |
| 8 | 1996-12-21 | 08:34:06.2 | -5.3 | 35.8 | 25 | -11 | -3.9 | 15 | -15 | 3 | 1.5 | 20.1 | 5.5 | 33 | 49 | -37 | 9 | 32.2 | 0.31 | 10-22 |
| 9 | 1997-02-23 | 01:39:34.9 | -5.3 | 34.8 | 10 | 0.64 | 0.19 | -0.83 | -2 | 1.1 | 0.16 | 2.44 | 4.9 | 190 | 14 | 155 | 10 | 69.4 | 0.44 | 15-29 |
| 10 | 1997-04-15 | 19:04:29.2 | -8.7 | 26.4 | 18 | -1.5 | -1.5 | 3 | -2 | -0.61 | 1.1 | 3.56 | 5.0 | 156 | 49 | -154 | 7 | 99.2 | 0.71 | 17-27 |
| 11 | 1998-04-12 | 10:49:00.8 | -12.4 | 25.5 | 33 | -1.1 | -0.38 | 1.5 | 1.1 | 0.16 | 0.32 | 1.75 | 4.8 | 340 | 46 | -141 | 7 | 67.8 | 0.31 | 17-27 |
| 12 | 1998-08-15 | 17:29:19.0 | 0.7 | 30.0 | 10 | -0.43 | 0.2 | 0.23 | 0.34 | 0.023 | 0.47 | 0.684 | 4.5 | 13 | 41 | -138 | 8 | 66.8 | 0.49 | 19-29 |
| 13 | 1998-08-24 | 12:12:11.1 | -13.8 | 34.9 | 10 | -0.56 | 0.031 | 0.53 | 0.36 | 0.31 | -0.03 | 0.722 | 4.5 | 339 | 33 | -129 | 6 | 55.4 | 0.44 | 18-29 |
| 14 | 1998-09-22 | 19:27:35.2 | -20.1 | 45.4 | 33 | -2.3 | 1.6 | 0.68 | 0.3 | 3.3 | 1.8 | 4.27 | 5.0 | 78 | 30 | -35 | 19 | 76.4 | 0.29 | 18-29 |
| 15 | 1999-04-06 | 04:16:47.0 | -8.5 | 39.4 | 14 | -3 | -0.16 | 3.2 | 0.57 | -2.8 | 1.5 | 4.51 | 5.0 | 223 | 31 | -50 | 10 | 92.2 | 0.33 | 15-28 |
| 16 | 1999-05-07 | 02:10:45.1 | -7.5 | 31.6 | 25 | -0.78 | -0.39 | 1.2 | 1.3 | 0.88 | -0.81 | 2.03 | 4.8 | 305 | 48 | -152 | 16 | 38.0 | 0.53 | 19-29 |
| 17 | 1999-05-07 | 14:07:32.9 | -7.5 | 31.7 | 25 | -6.4 | 2.1 | 4.3 | 3.1 | 2.6 | -5.1 | 8.62 | 5.2 | 294 | 52 | -130 | 16 | 91.0 | 0.42 | 13-24 |
| 18 | 1999-08-06 | 17:22:48.8 | -8.6 | 21.6 | 10 | 0.7 | -0.018 | -0.68 | -0.22 | -0.84 | -0.029 | 1.11 | 4.6 | 354 | 19 | 73 | 7 | 94.0 | 0.47 | 17-29 |
| 19 | 1999-09-01 | 04:07:56.5 | -10.1 | 34.2 | 10 | -0.39 | -0.23 | 0.62 | -0.52 | -1.2 | -0.013 | 1.38 | 4.7 | 147 | 16 | -144 | 7 | 86.0 | 0.38 | 18-29 |
| 20 | 2000-01-04 | 00:25:09.4 | -16.1 | 36.1 | 25 | -1.4 | 0.22 | 1.1 | 0.3 | -1 | 0.11 | 1.67 | 4.8 | 194 | 26 | -70 | 8 | 70.2 | 0.60 | 15-24 |
| 21 | 2000-01-14 | 03:32:44.2 | -16.0 | 41.9 | 6 | 0.82 | -0.16 | -0.66 | -0.91 | -1.4 | 0.11 | 1.81 | 4.8 | 347 | 14 | 49 | 6 | 61.4 | 0.32 | 21-29 |
| 22 | 2000-03-02 | 02:44:55.5 | -2.2 | 28.4 | 6 | -1.2 | 0.3 | 0.89 | 0.95 | -0.17 | 0.68 | 1.6 | 4.7 | 9 | 42 | -133 | 11 | 62.4 | 0.48 | 19-29 |
| 23 | 2000-03-02 | 04:29:50.2 | -2.4 | 28.2 | 25 | -0.43 | 0.28 | 0.15 | -0.67 | -0.89 | 0.7 | 1.37 | 4.7 | 33 | 75 | -103 | 6 | 43.4 | 0.44 | 17-28 |
| 24 | 2000-03-03 | 05:03:22.3 | -2.4 | 28.2 | 33 | -0.23 | 0.79 | -0.56 | -0.5 | -0.42 | 0.36 | 1.03 | 4.6 | 37 | 83 | -137 | 7 | 48.6 | 0.56 | 17-29 |
| 25 | 2000-10-05 | 23:08:35.9 | -8.0 | 30.5 | 25 | -1.8 | 0.65 | 1.1 | -0.083 | 0.74 | -0.31 | 1.76 | 4.8 | 161 | 57 | -84 | 12 | 47.2 | 0.39 | 21-29 |
| 26 | 2000-10-07 | 01:39:10.4 | -8.0 | 30.7 | 25 | -0.8 | 1.2 | -0.4 | 0.49 | 0.66 | -0.9 | 1.61 | 4.7 | 149 | 56 | -32 | 10 | 99.0 | 0.34 | 21-29 |
| 27 | 2000-10-23 | 12:02:14.7 | 1.5 | 30.7 | 25 | -1.3 | -0.36 | 1.7 | -1 | 0.86 | 0.94 | 2.23 | 4.8 | 52 | 48 | -37 | 10 | 81.4 | 0.52 | 19-29 |
| 28 | 2000-12-02 | 04:16:43.0 | -7.3 | 27.8 | 18 | -1.2 | 0.39 | 0.83 | 0.073 | -0.42 | 0.7 | 1.36 | 4.7 | 230 | 40 | -68 | 10 | 93.6 | 0.35 | 16-24 |
| 29 | 2000-12-15 | 10:01:22.8 | -5.5 | 29.4 | 33 | -0.94 | -0.38 | 1.3 | -0.64 | -0.055 | -0.66 | 1.49 | 4.7 | 12 | 52 | -40 | 14 | 83.4 | 0.36 | 21-29 |
| 30 | 2001-01-31 | 19:15:29.2 | 0.6 | 30.2 | 33 | -0.001 | 0.67 | -0.67 | 0.71 | -0.57 | 0.4 | 1.2 | 4.7 | 32 | 40 | -179 | 9 | 78.0 | 0.41 | 18-29 |
| 31 | 2001-03-25 | 18:54:14.2 | -5.7 | 35.9 | 33 | -0.021 | -0.026 | 0.047 | 0.013 | -0.061 | -0.0047 | 0.0747 | 4.5 | 202 | 17 | -53 | 6 | 41.6 | 0.43 | 15-28 |
| 32 | 2001-04-17 | 04:39:03.4 | -6.2 | 22.8 | 33 | -0.62 | 0.96 | -0.34 | -0.28 | -0.42 | 0.38 | 1.06 | 4.6 | 287 | 43 | -37 | 12 | 59.8 | 0.53 | 21-29 |
| 33 | 2001-07-13 | 19:24:02.4 | -6.9 | 30.9 | 42 | -0.46 | 0.15 | 0.31 | 0.48 | 0.66 | 0.01 | 0.917 | 4.6 | 12 | 12 | -110 | 10 | 61.8 | 0.29 | 21-29 |
| 34 | 2001-09-18 | 11:01:02.1 | -7.5 | 31.6 | 10 | -0.095 | -0.14 | 0.24 | 0.45 | 0.042 | 0.27 | 0.566 | 4.4 | 350 | 37 | -169 | 11 | 69.8 | 0.56 | 19-29 |
| 35 | 2002-01-04 | 13:02:21.2 | -0.2 | 29.8 | 10 | -3.9 | 4.1 | -0.16 | 0.34 | 5.4 | 3.1 | 7.43 | 5.2 | 90 | 38 | -32 | 6 | 69.0 | 0.17 | 15-26 |
| 36 | 2002-01-17 | 20:01:30.7 | -1.7 | 29.2 | 25 | -1.9 | -0.59 | 2.5 | -0.87 | -2.9 | 0.39 | 3.77 | 5.0 | 16 | 71 | -82 | 9 | 71.6 | 0.23 | 18-26 |
| 37 | 2002-01-19 | 17:09:31.7 | -1.9 | 29.6 | 33 | -0.42 | -0.36 | 0.78 | -0.27 | -1.7 | 0.15 | 1.82 | 4.8 | 9 | 80 | -88 | 8 | 61.8 | 0.32 | 13-27 |
| 38 | 2002-10-24 | 07:12:19.7 | -1.9 | 28.9 | 33 | -3.9 | 5.5 | -1.6 | 4.7 | -0.88 | 3.6 | 7.74 | 5.2 | 33 | 37 | -146 | 9 | 64.6 | 0.53 | 16-29 |

Columns as follows: number of event, date of occurrence, time, latitude, longitude, depth [km], moment tensor elements [10^{16} Nm] (six columns), seismic moment [10^{16} Nm], moment magnitude, strike, dip, rake, number of waveform traces inverted Σ (N_{final}), percentage of double couple p , variance σ , inverted frequency range F_{final} [mHz].

Table A.2: *CMT*-solutions for eastern Africa 1994-2002.

| yr-mo-day | hr:min:s | Lat | Lon | D | M_{11} | M_{22} | M_{33} | M_{12} | M_{13} | M_{23} | M_0 | exp | M_W | Str | Dip | Ra | Σ_b | Σ_m | p |
|------------|------------|-------|------|----|----------|----------|----------|----------|----------|----------|-------|-----|-------|-----|-----|------|------------|------------|------|
| 1994-02-05 | 23:34:14.1 | 0.5 | 29.9 | 15 | -1.4 | 0.015 | 1.4 | 0.57 | -1.5 | 0.18 | 2.12 | 18 | 6.2 | 203 | 25 | -57 | 123 | 51 | 84.6 |
| 1994-08-18 | 00:45:52.7 | -7.7 | 31.8 | 25 | -6.3 | 2.2 | 4.1 | -2.1 | 5.8 | -2.6 | 8.67 | 17 | 5.9 | 317 | 23 | -107 | 118 | 15 | 87.9 |
| 1995-08-10 | 00:41:08.7 | -15.5 | 41.4 | 15 | -7.9 | -0.086 | 8 | 2.1 | 2.4 | -1.9 | 8.78 | 16 | 5.2 | 332 | 41 | -115 | 56 | 0 | 94.8 |
| 1995-12-11 | 17:54:42.6 | -6.2 | 26.6 | 15 | -2.1 | -0.45 | 2.6 | 2.1 | -2.2 | -0.18 | 3.85 | 17 | 5.7 | 200 | 27 | -41 | 8 | 0 | 84.5 |
| 1996-03-24 | 08:24:31.7 | 0.3 | 29.9 | 15 | -0.73 | -0.31 | 1 | -0.044 | -0.79 | 0.032 | 1.19 | 17 | 5.3 | 179 | 24 | -94 | 26 | 0 | 53.7 |
| 1996-12-20 | 03:53:24.6 | -5.2 | 36.0 | 15 | -1.5 | -4.3 | 5.9 | 1.7 | -2.5 | 1 | 6.11 | 16 | 5.1 | 229 | 57 | -10 | 9 | 0 | 66.2 |
| 1997-09-21 | 18:13:32.5 | -7.3 | 30.3 | 30 | -5.7 | -0.66 | 6.3 | 1.7 | 4.5 | -2.9 | 8.27 | 17 | 5.9 | 315 | 36 | -133 | 108 | 38 | 92.9 |
| 1998-03-28 | 22:00:02.7 | -5.9 | 29.2 | 15 | 2.3 | -6.2 | 4 | -0.78 | -8.9 | 4.3 | 10.8 | 16 | 5.3 | 257 | 45 | 16 | 50 | 0 | 36.4 |
| 2000-05-21 | 02:58:45.8 | -12.5 | 43.3 | 15 | 0.47 | 3.2 | -3.7 | 5.2 | -3.9 | -3.9 | 7.86 | 16 | 5.2 | 59 | 44 | 171 | 26 | 0 | 29.1 |
| 2000-10-02 | 02:25:38.4 | -7.8 | 30.6 | 40 | -5 | 0.001 | 5 | 0.76 | -2.3 | -1 | 5.68 | 18 | 6.4 | 172 | 32 | -85 | 144 | 129 | 93.4 |
| 2001-06-29 | 23:40:08.0 | 0.3 | 30.0 | 15 | -6.7 | -1.1 | 7.9 | -2.5 | 4.2 | -0.16 | 8.82 | 16 | 5.2 | 17 | 33 | -60 | 23 | 0 | 90.5 |
| 2002-01-20 | 00:14:47.9 | -1.7 | 29.2 | 15 | -3.8 | -2.6 | 6.4 | -1.5 | 1.3 | 1.4 | 5.94 | 16 | 5.1 | 39 | 49 | -42 | 29 | 0 | 51.8 |
| 2002-01-21 | 04:39:24.9 | -1.8 | 29.0 | 15 | -3.1 | 1.1 | 2 | 3.4 | 1.7 | 2.3 | 5.23 | 16 | 5.1 | 18 | 26 | -128 | 21 | 0 | 84.6 |
| 2002-01-22 | 15:32:08.6 | -1.5 | 28.9 | 15 | -2.7 | -2.6 | 5.3 | -1.2 | -5.5 | 3.3 | 7.41 | 16 | 5.2 | 233 | 26 | -43 | 26 | 0 | 22.7 |
| 2002-02-20 | 19:07:21.3 | -8.2 | 32.0 | 45 | -1.8 | 1.2 | 0.63 | 0.31 | 0.02 | -1.1 | 1.98 | 17 | 5.5 | 135 | 42 | -79 | 84 | 0 | 78.9 |
| 2002-03-05 | 17:07:47.0 | -11.8 | 24.6 | 15 | -3 | 2 | 1 | 0.94 | -6 | 1.2 | 6.41 | 16 | 5.1 | 230 | 15 | -40 | 15 | 0 | 42.8 |
| 2002-05-18 | 15:15:13.8 | -3.0 | 33.6 | 15 | -0.34 | 2.1 | -1.8 | 0.9 | -0.15 | -1 | 7.78 | 17 | 5.5 | 150 | 76 | 10 | 86 | 0 | 53.6 |
| 2002-07-16 | 14:50:20.7 | -11.7 | 41.0 | 15 | -5.6 | -0.93 | 6.5 | 3.5 | -3.1 | -1.1 | 7.78 | 16 | 5.2 | 195 | 34 | -50 | 45 | 0 | 95.9 |
| 2002-08-31 | 22:52:38.6 | -10.2 | 34.3 | 15 | -4.5 | 0.9 | 3.6 | 1.6 | -4.1 | -3 | 6.65 | 16 | 5.1 | 136 | 25 | -109 | 31 | 0 | 75.5 |
| 2002-10-24 | 06:08:42.9 | -1.9 | 28.7 | 15 | -2.1 | 0.16 | 1.9 | 0.26 | -0.4 | 0.71 | 2.17 | 18 | 6.2 | 210 | 42 | -75 | 149 | 117 | 97.2 |
| 2002-12-23 | 02:50:42.2 | -1.8 | 34.7 | 15 | 0.31 | 5.9 | -6.2 | -3.1 | 2.1 | -0.34 | 7.16 | 16 | 5.2 | 225 | 59 | 175 | 46 | 0 | 86.0 |

Columns as follows: date of occurrence, time, latitude, longitude, depth [km], moment tensor elements [10^{exp} Nm] (six columns), seismic moment [10^{exp} Nm], Exponent, moment magnitude, strike, dip, rake, number of waveform traces inverted Σ_b ($T \geq 45$ s), Σ_m ($T \geq 135$ s), percentage of double couple p .

Appendix A. Tables of earthquake locations and moment tensor inversion results

Table A.3: Earthquakes in eastern Africa 1994-2002 in the Engdahl catalogue.

| yr-mo-day | hr:min:s | Lat | Lon | D | m_b | MT | yr-mo-day | hr:min:s | Lat | Lon | D | m_b | MT |
|------------|------------|-------|------|----|-------|-----|------------|------------|-------|------|----|-------|-----|
| 1994-02-05 | 23:34:11.3 | 0.6 | 30.1 | 14 | 5.8 | CMT | 1999-09-01 | 04:07:56.6 | -10.1 | 34.2 | 15 | 4.5 | #19 |
| 1994-04-24 | 09:52:59.2 | -9.1 | 30.5 | 27 | 5.1 | | 2000-01-04 | 00:25:09.4 | -16.1 | 36.1 | 20 | 4.8 | #20 |
| 1994-08-18 | 00:45:48.8 | -7.5 | 31.7 | 25 | 5.9 | CMT | 2000-01-14 | 03:32:44.2 | -16.0 | 41.9 | 18 | 4.5 | #21 |
| 1995-01-20 | 07:14:28.9 | 7.1 | 38.4 | 12 | 5.0 | | 2000-03-02 | 02:44:55.5 | -2.2 | 28.4 | 12 | 5.3 | #22 |
| 1995-04-27 | 02:32:20.9 | -12.6 | 42.5 | 15 | 4.7 | #01 | 2000-03-02 | 04:29:50.3 | -2.4 | 28.2 | 10 | 4.9 | #23 |
| 1995-04-29 | 11:50:53.9 | -1.3 | 28.6 | 6 | 5.0 | #02 | 2000-03-03 | 05:03:22.3 | -2.4 | 28.2 | 13 | 4.9 | #24 |
| 1995-07-20 | 05:08:28.4 | -12.4 | 41.5 | 15 | 5.0 | #03 | 2000-05-21 | 02:58:45.6 | -12.2 | 43.7 | 15 | 5.0 | CMT |
| 1995-07-22 | 13:31:59.4 | -14.0 | 34.8 | 35 | 4.9 | | 2000-07-10 | 17:48:32.1 | -7.2 | 27.7 | 28 | 4.7 | |
| 1995-08-10 | 00:41:08.1 | -15.6 | 41.5 | 24 | 5.0 | CMT | 2000-09-05 | 07:11:33.0 | 1.0 | 25.9 | 15 | 4.5 | |
| 1995-09-30 | 20:46:07.5 | -13.8 | 34.4 | 28 | 4.7 | | 2000-09-12 | 16:51:20.2 | -2.3 | 28.7 | 15 | 4.5 | |
| 1995-11-12 | 19:00:09.8 | -13.8 | 31.6 | 28 | 4.8 | #04 | 2000-10-02 | 02:25:33.3 | -8.0 | 30.8 | 34 | 6.0 | CMT |
| 1995-12-08 | 23:40:51.8 | -4.6 | 38.8 | 15 | 5.0 | #05 | 2000-10-05 | 23:08:35.9 | -8.0 | 30.5 | 27 | 4.7 | #25 |
| 1995-12-11 | 17:54:41.5 | -6.2 | 26.7 | 11 | 5.4 | CMT | 2000-10-07 | 01:39:10.5 | -8.0 | 30.7 | 34 | 4.7 | #26 |
| 1996-02-29 | 07:14:18.7 | -2.4 | 47.0 | 16 | 5.0 | #06 | 2000-10-23 | 12:02:14.8 | 1.5 | 30.7 | 19 | 4.4 | #27 |
| 1996-03-24 | 08:24:26.4 | 0.5 | 30.0 | 6 | 5.0 | CMT | 2000-12-02 | 04:16:43.0 | -7.3 | 27.8 | 9 | 5.0 | #28 |
| 1996-05-31 | 09:36:22.7 | -13.8 | 34.3 | 28 | 4.5 | | 2000-12-15 | 10:01:22.9 | -5.5 | 29.4 | 15 | 3.9 | #29 |
| 1996-06-09 | 20:12:35.9 | -12.6 | 26.2 | 12 | 4.9 | | 2001-01-31 | 19:15:29.2 | 0.6 | 30.2 | 15 | 4.0 | #30 |
| 1996-06-15 | 10:02:44.0 | -16.5 | 41.6 | 18 | 5.0 | | 2001-02-03 | 17:05:14.1 | -16.8 | 28.6 | 13 | 4.2 | |
| 1996-08-22 | 07:14:49.3 | -14.7 | 41.3 | 28 | 4.5 | | 2001-03-25 | 18:54:14.3 | -5.7 | 35.9 | 15 | 3.6 | #31 |
| 1996-08-30 | 06:58:45.2 | -15.4 | 34.1 | 26 | 4.5 | #07 | 2001-04-17 | 04:39:03.4 | -6.3 | 22.8 | 17 | 3.7 | #32 |
| 1996-12-20 | 03:53:24.4 | -5.3 | 35.9 | 10 | 4.8 | CMT | 2001-06-29 | 23:40:03.7 | 0.2 | 30.0 | 19 | 4.7 | CMT |
| 1996-12-21 | 08:34:06.2 | -5.3 | 35.8 | 18 | 4.7 | #08 | 2001-07-13 | 19:24:02.4 | -6.9 | 30.9 | 45 | 4.7 | #33 |
| 1997-02-23 | 01:39:35.0 | -5.3 | 34.8 | 20 | 4.5 | #09 | 2001-08-26 | 17:56:15.3 | -5.7 | 36.1 | 10 | 3.8 | |
| 1997-04-15 | 19:04:29.4 | -8.7 | 26.4 | 8 | 4.8 | #10 | 2001-09-18 | 11:01:02.1 | -7.5 | 31.6 | 15 | 3.5 | #34 |
| 1997-07-18 | 01:45:15.3 | 2.4 | 31.6 | 15 | 4.7 | | 2002-01-04 | 13:02:21.3 | -0.2 | 29.8 | 15 | 4.8 | #35 |
| 1997-07-18 | 03:17:27.7 | 2.5 | 31.6 | 15 | 4.7 | | 2002-01-17 | 20:01:30.7 | -1.7 | 29.2 | 14 | 4.7 | #36 |
| 1997-09-21 | 18:13:26.8 | -7.4 | 30.3 | 24 | 5.5 | CMT | 2002-01-19 | 17:09:31.7 | -1.9 | 29.6 | 15 | 4.6 | #37 |
| 1997-10-11 | 04:11:27.3 | -10.6 | 24.8 | 33 | 4.5 | | 2002-01-20 | 00:14:47.2 | -1.7 | 29.0 | 16 | 4.9 | CMT |
| 1998-03-28 | 21:59:58.5 | -6.1 | 29.5 | 16 | 5.2 | CMT | 2002-01-21 | 04:39:24.2 | -1.8 | 29.0 | 15 | 4.9 | CMT |
| 1998-04-12 | 10:49:00.8 | -12.4 | 25.5 | 22 | 4.9 | #11 | 2002-01-22 | 15:32:07.8 | -1.6 | 29.0 | 15 | 4.9 | CMT |
| 1998-08-15 | 17:29:19.0 | 0.7 | 30.0 | 16 | 4.7 | #12 | 2002-02-20 | 19:07:18.5 | -7.7 | 31.9 | 35 | 5.7 | CMT |
| 1998-08-24 | 12:12:11.2 | -13.8 | 34.9 | 45 | 4.7 | #13 | 2002-03-05 | 17:07:45.6 | -11.8 | 24.8 | 18 | 5.1 | CMT |
| 1998-08-29 | 04:49:57.8 | -2.0 | 27.6 | 5 | 4.5 | | 2002-05-18 | 15:15:12.0 | -2.8 | 33.8 | 15 | 5.2 | CMT |
| 1998-09-22 | 19:27:35.2 | -20.1 | 45.4 | 28 | 4.8 | #14 | 2002-07-10 | 11:04:06.8 | -5.5 | 35.8 | 8 | 4.7 | |
| 1999-04-06 | 04:16:47.7 | -8.5 | 39.4 | 16 | 4.8 | #15 | 2002-07-16 | 14:50:16.2 | -11.8 | 41.1 | 12 | 5.1 | CMT |
| 1999-05-07 | 02:10:45.2 | -7.6 | 31.6 | 18 | 5.1 | #16 | 2002-08-31 | 22:52:37.2 | -9.9 | 34.2 | 26 | 4.9 | CMT |
| 1999-05-07 | 14:07:33.0 | -7.5 | 31.7 | 25 | 5.5 | #17 | 2002-10-13 | 04:46:34.8 | -5.4 | 35.9 | 10 | 4.7 | |
| 1999-05-25 | 21:28:25.7 | -12.8 | 27.4 | 15 | 4.5 | | 2002-10-24 | 06:08:39.5 | -1.9 | 29.0 | 11 | 5.9 | CMT |
| 1999-08-04 | 06:42:15.4 | -6.2 | 26.6 | 8 | 4.8 | | 2002-10-24 | 07:12:19.7 | -1.9 | 28.9 | 8 | 5.3 | #38 |
| 1999-08-06 | 17:22:48.8 | -8.6 | 21.6 | 10 | 4.5 | #18 | 2002-10-24 | 10:19:24.5 | -1.9 | 29.0 | 10 | 4.8 | |
| 1999-09-01 | 04:07:56.6 | -10.1 | 34.2 | 15 | 4.5 | | 2002-10-26 | 12:56:48.8 | -1.8 | 29.0 | 10 | 4.7 | |
| 2000-01-04 | 00:25:09.4 | -16.1 | 36.1 | 20 | 4.8 | | 2002-12-23 | 02:50:39.9 | -1.7 | 35.0 | 7 | 4.6 | CMT |

Columns as follows: date of occurrence, time, latitude, longitude, depth [km], body-wave magnitude, moment tensor (MT) calculated by Harvard-CMT or in this work.

Table A.4: Focal mechanisms used for stress and strain calculation.

| yr-mo-day | Lat | Lon | D | Str | Dip | Ra | M_W | yr-mo-day | Lat | Lon | D | Str | Dip | Ra | M_W |
|-------------------------|-------|------|----|-----|-----|------|-------|------------|-------|------|----|-----|-----|------|-------|
| 1964-05-07 ³ | -3.9 | 34.9 | 34 | 283 | 89 | 44 | 6.4 | 1990-05-15 | -3.1 | 35.4 | 15 | 59 | 43 | -136 | 5.5 |
| 1966-03-20 ⁴ | 0.8 | 29.9 | 6 | 33 | 42 | -100 | 7.0 | 1990-05-15 | -3.4 | 35.8 | 15 | 332 | 29 | -106 | 5.4 |
| 1966-03-21 ¹ | 0.8 | 29.6 | 7 | 40 | 60 | -102 | 5.3 | 1990-05-20 | 5.3 | 32.3 | 15 | 224 | 67 | 176 | 7.1 |
| 1966-05-06 ¹ | -15.7 | 34.6 | 17 | 227 | 50 | -56 | 5.3 | 1990-05-24 | 5.7 | 31.7 | 15 | 232 | 43 | -131 | 7.1 |
| 1966-05-17 ⁴ | 0.8 | 29.9 | 6 | 3 | 53 | -92 | 5.8 | 1990-05-24 | 5.9 | 31.6 | 25 | 236 | 39 | -104 | 6.5 |
| 1966-10-05 ¹ | 0.0 | 29.9 | 23 | 156 | 54 | -116 | 5.3 | 1990-07-09 | 5.8 | 31.6 | 15 | 28 | 44 | -149 | 6.3 |
| 1967-10-14 ¹ | -3.3 | 38.2 | 10 | 142 | 70 | -125 | 5.1 | 1990-07-28 | 6.0 | 32.0 | 15 | 277 | 45 | -90 | 5.3 |
| 1968-05-15 ⁴ | -15.9 | 26.2 | 30 | 36 | 34 | -114 | 5.7 | 1990-09-04 | -0.1 | 29.4 | 15 | 229 | 77 | 6 | 5.3 |
| 1968-12-02 ⁴ | -14.0 | 23.8 | 11 | 35 | 36 | -81 | 5.6 | 1990-09-07 | 5.1 | 31.6 | 15 | 44 | 43 | -147 | 5.5 |
| 1972-02-13 ¹ | -4.5 | 34.1 | 6 | 340 | 62 | -61 | 5.0 | 1990-11-03 | -21.5 | 33.3 | 15 | 345 | 35 | -111 | 5.1 |
| 1972-12-18 ¹ | -16.7 | 28.1 | 7 | 234 | 58 | -52 | 5.3 | 1991-02-22 | -3.9 | 35.9 | 15 | 182 | 45 | -104 | 5.2 |
| 1974-04-25 ¹ | 1.1 | 30.1 | 10 | 9 | 40 | -87 | 4.9 | 1991-03-29 | 5.4 | 31.8 | 15 | 130 | 15 | -51 | 5.4 |
| 1975-02-15 ² | -16.5 | 41.5 | 25 | 350 | 20 | -75 | 5.2 | 1991-04-21 | -18.5 | 46.4 | 15 | 327 | 44 | -128 | 5.5 |
| 1975-03-26 ¹ | -5.3 | 30.1 | 16 | 354 | 51 | -112 | 5.0 | 1991-07-24 | -18.3 | 34.6 | 15 | 180 | 45 | -90 | 5.1 |
| 1975-04-04 ¹ | -21.2 | 45.1 | 11 | 74 | 85 | 40 | 5.3 | 1991-10-09 | 2.2 | 31.2 | 15 | 260 | 56 | -41 | 5.6 |
| 1976-09-19 ⁴ | -11.1 | 32.8 | 29 | 349 | 42 | -123 | 5.7 | 1992-09-11 | -5.9 | 26.4 | 22 | 196 | 38 | -132 | 6.3 |
| 1977-01-06 | -2.3 | 28.4 | 15 | 241 | 45 | -90 | 5.1 | 1992-09-23 | -5.6 | 26.5 | 18 | 42 | 50 | -55 | 5.5 |
| 1977-07-06 ¹ | -6.3 | 29.6 | 14 | 168 | 63 | -77 | 5.2 | 1992-11-14 | -23.0 | 45.5 | 15 | 350 | 45 | -90 | 5.0 |
| 1977-12-15 | -4.8 | 34.7 | 15 | 151 | 31 | -64 | 5.7 | 1993-02-13 | 7.8 | 39.1 | 14 | 90 | 74 | 10 | 5.3 |
| 1978-01-08 | -11.8 | 34.5 | 15 | 338 | 45 | -90 | 4.9 | 1994-02-05 | 0.5 | 29.9 | 25 | 203 | 25 | -57 | 6.2 |
| 1979-11-06 | -12.0 | 41.6 | 15 | 318 | 35 | -135 | 5.2 | 1994-08-18 | -7.7 | 31.8 | 15 | 317 | 23 | -107 | 5.9 |
| 1980-01-09 | -2.7 | 27.6 | 29 | 45 | 48 | -142 | 5.2 | 1995-08-10 | -15.5 | 41.4 | 34 | 332 | 41 | -115 | 5.2 |
| 1981-07-30 | -2.4 | 28.1 | 15 | 235 | 45 | -90 | 5.1 | 1995-12-11 | -6.2 | 26.6 | 18 | 200 | 27 | -41 | 5.7 |
| 1981-11-18 | -2.5 | 22.8 | 16 | 133 | 66 | -7 | 5.5 | 1996-03-24 | 0.3 | 29.9 | 15 | 179 | 24 | -94 | 5.3 |
| 1982-04-29 | -10.0 | 41.6 | 10 | 356 | 45 | -90 | 5.1 | 1996-12-20 | -5.2 | 36.0 | 15 | 229 | 57 | -10 | 5.1 |
| 1982-07-03 | -3.6 | 29.0 | 15 | 328 | 50 | -136 | 5.3 | 1997-09-21 | -7.3 | 30.3 | 15 | 315 | 36 | -133 | 5.9 |
| 1983-01-31 | -23.0 | 44.4 | 15 | 326 | 45 | -90 | 5.1 | 1998-03-28 | -5.9 | 29.2 | 15 | 257 | 45 | 16 | 5.3 |
| 1983-07-07 | -7.2 | 27.9 | 15 | 200 | 41 | -111 | 5.8 | 2000-05-21 | -12.5 | 43.3 | 15 | 59 | 44 | 171 | 5.2 |
| 1983-09-03 | -15.3 | 41.0 | 10 | 340 | 45 | -90 | 5.0 | 2000-10-02 | -7.8 | 30.6 | 15 | 172 | 32 | -85 | 6.4 |
| 1983-12-02 | 7.4 | 38.6 | 10 | 342 | 40 | -101 | 5.3 | 2001-06-29 | 0.3 | 30.0 | 15 | 17 | 33 | -60 | 5.2 |
| 1983-12-27 | -17.9 | 45.0 | 15 | 158 | 35 | -98 | 5.1 | 2002-01-20 | -1.7 | 29.2 | 15 | 39 | 49 | -42 | 5.1 |
| 1984-01-11 | -6.7 | 27.4 | 12 | 19 | 62 | -157 | 5.6 | 2002-01-21 | -1.8 | 29.0 | 15 | 18 | 26 | -128 | 5.1 |
| 1984-08-25 | -7.9 | 32.8 | 15 | 126 | 42 | -122 | 5.3 | 2002-01-22 | -1.5 | 28.9 | 15 | 233 | 26 | -43 | 5.2 |
| 1984-10-26 | -15.8 | 28.6 | 15 | 215 | 13 | -71 | 5.3 | 2002-02-20 | -8.2 | 32.0 | 15 | 135 | 42 | -79 | 5.5 |
| 1985-05-14 | -10.3 | 41.4 | 15 | 170 | 34 | -89 | 6.3 | 2002-03-05 | -11.8 | 24.6 | 35 | 230 | 15 | -40 | 5.1 |
| 1985-05-14 | -10.3 | 41.5 | 24 | 178 | 43 | -70 | 6.0 | 2002-05-18 | -3.0 | 33.6 | 15 | 150 | 76 | 10 | 5.5 |
| 1985-05-30 | -10.2 | 41.6 | 15 | 148 | 38 | -104 | 5.3 | 2002-07-16 | -11.7 | 41.0 | 10 | 195 | 34 | -50 | 5.2 |
| 1985-06-28 | -2.3 | 29.0 | 15 | 211 | 45 | -90 | 4.9 | 2002-08-31 | -10.2 | 34.3 | 15 | 136 | 25 | -109 | 5.2 |
| 1985-06-28 | -10.3 | 41.5 | 15 | 346 | 44 | -93 | 5.6 | 2002-10-24 | -1.9 | 28.7 | 15 | 210 | 42 | -75 | 6.2 |
| 1985-08-20 | 5.7 | 36.0 | 15 | 258 | 31 | -45 | 5.4 | 2002-12-23 | -1.8 | 34.7 | 15 | 225 | 59 | 175 | 5.2 |
| 1985-10-04 | -18.1 | 48.6 | 14 | 147 | 32 | -115 | 5.5 | 2003-03-20 | -3.0 | 29.6 | 15 | 17 | 45 | -23 | 5.2 |
| 1986-03-14 | -10.5 | 27.2 | 32 | 208 | 33 | -105 | 4.9 | 2003-04-10 | -5.2 | 29.1 | 45 | 61 | 46 | -49 | 5.1 |
| 1986-06-29 | -5.0 | 29.5 | 15 | 318 | 22 | -148 | 5.8 | 2003-06-14 | -5.7 | 36.0 | 15 | 340 | 26 | -112 | 5.0 |
| 1986-07-18 | -16.1 | 28.4 | 15 | 238 | 43 | -84 | 5.2 | 2003-08-05 | -0.8 | 29.4 | 15 | 330 | 34 | -155 | 5.2 |
| 1987-10-07 | 6.5 | 37.3 | 10 | 216 | 20 | -79 | 5.3 | 2004-03-14 | -10.1 | 34.4 | 15 | 162 | 44 | -117 | 4.8 |
| 1987-10-25 | 5.8 | 36.4 | 10 | 232 | 38 | -51 | 6.2 | 2004-08-21 | -10.6 | 34.4 | 15 | 346 | 61 | -17 | 4.7 |
| 1987-10-28 | 5.9 | 36.6 | 10 | 211 | 45 | -78 | 6.0 | 2005-01-04 | -10.3 | 41.4 | 15 | 177 | 39 | -58 | 5.0 |
| 1988-04-16 | -10.2 | 27.4 | 17 | 10 | 26 | -120 | 5.1 | 2005-01-15 | -6.1 | 39.2 | 10 | 159 | 45 | -116 | 5.0 |
| 1989-03-09 | -13.4 | 34.3 | 15 | 128 | 23 | -118 | 5.6 | 2005-12-05 | -6.2 | 29.6 | 30 | 149 | 50 | -122 | 6.8 |
| 1989-03-10 | -13.4 | 34.3 | 15 | 142 | 17 | -102 | 6.3 | 2005-12-06 | -6.2 | 29.5 | 40 | 19 | 40 | -58 | 5.2 |
| 1989-06-08 | 7.3 | 38.2 | 10 | 200 | 45 | -90 | 4.9 | 2005-12-08 | -6.1 | 29.5 | 15 | 184 | 39 | -90 | 5.1 |
| 1989-09-05 | -11.8 | 34.5 | 20 | 63 | 52 | 149 | 5.4 | 2005-12-08 | -6.1 | 29.6 | 15 | 190 | 44 | -107 | 5.0 |
| 1990-03-13 | -3.9 | 40.5 | 10 | 323 | 46 | -121 | 5.5 | 2005-12-09 | -6.2 | 29.7 | 15 | 33 | 39 | -54 | 5.5 |
| 1990-04-05 | -3.0 | 36.0 | 29 | 352 | 45 | -90 | 5.1 | | | | | | | | |

Columns as follows: date of occurrence, latitude, longitude, depth [km], strike, dip, rake, moment magnitude. Superscripts refer to following studies: ¹Shudofsky (1985), ²Grimison and Chen (1988), ³Nyblade and Langston (1995) and ⁴Foster and Jackson (1998). Other data are *CMT*-solutions (e.g. Dziewonski et al., 1987b).

Appendix B

Figures of moment tensor inversion results

The following pages show figures of the summarised results of the frequency sensitive moment tensor inversion for 38 earthquakes in eastern Africa. Quantitative description is given in Table A.1. Figures are listed chronologically and geographical earthquake locations are given following the seismo-tectonic *Flinn-Engdahl*-regionalisation scheme (Flinn et al., 1974).

For each event three figures are shown: (1) the frequency sensitive inversion of N_{final} (STEP 3A of the processing, lower right); (2) the depth-variance analysis for N_{final} and F_{final} (STEP 3B, upper right) and (3) the final inversion with synthetics displayed for each waveform component included in the final dataset N_{final} (left side, compare Fig. 3.3, 3.4). The detailed captions are:

(1) Frequency sensitive moment tensor inversion for 8 mHz wide pass-bands and discrete hypocentral depths. Inversion of the final dataset N_{final} (STEP 3A); the right column gives the inversion results for N_{final} and the full frequency range from 10–29 mHz.

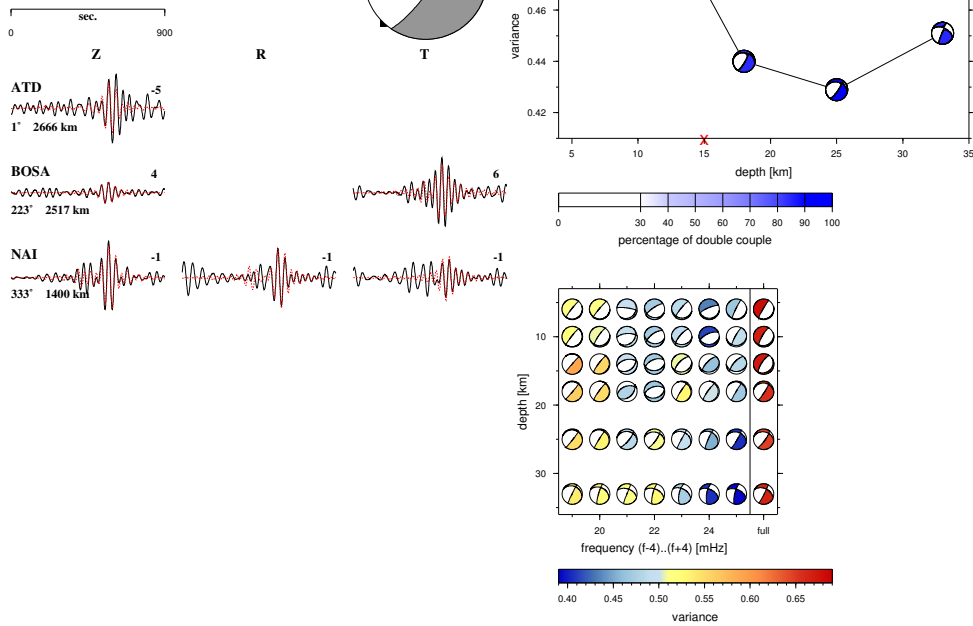
(2) Variance σ of focal mechanism solutions in dependence on hypocentral depth for the final dataset N_{final} and the final frequency range F_{final} given in subfigure (3). Blue colour indicates the percentage of double couple p . The red cross marks the depth determination of the Engdahl catalogue with standard deviation (red lines, Engdahl et al., 1998). When no standard deviation is plotted the source depths is fixed to 15 km.

(3) Final solution of the moment tensor inversion for N_{final} and F_{final} (fourth header line). Triangles around the focal mechanism indicate station azimuth. The inverted waveform traces on the vertical, radial and transversal component (Z, R, T) are plotted as black solid lines, synthetics as red dashed lines (including a 5% cosine taper on both sides). Station name and time shift Δt is given above each trace, azimuth and epicentral distance below. Amplitudes are plotted normalised to the maximum of each station.

Appendix B. Figures of moment tensor inversion results

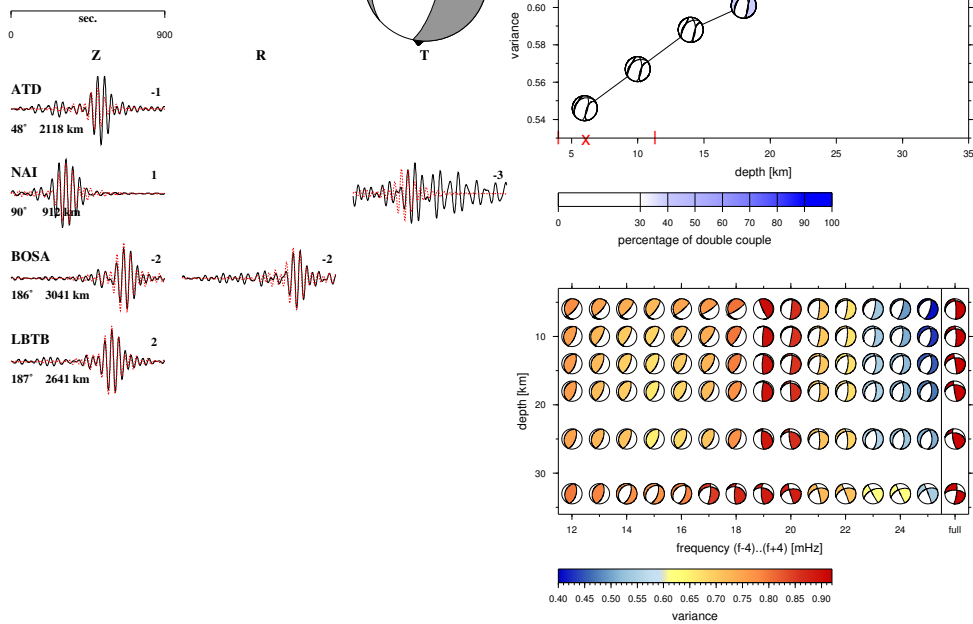
(# 01) NORTHWEST OF MADAGASCAR

Date: 27. 4.95 Time: 2:32:21.0 Lat: -12.60 Long: 42.50 Depth: 25
 Plane (strike/dip/slip) NP1: 283/30/-24 NP2: 34/77/-118
 Frequency range (Hz): .0180-.0290 Variance: 0.429 Mw: 4.7
 95.8% double couple



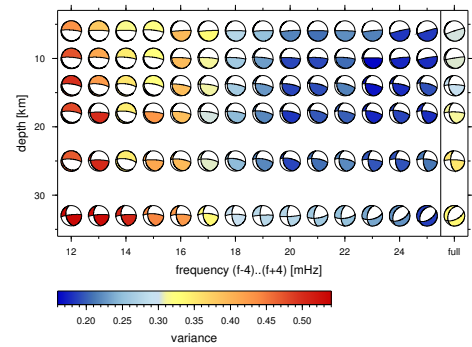
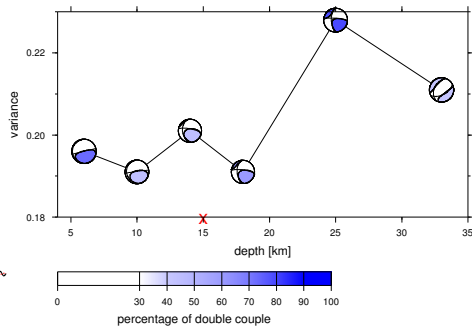
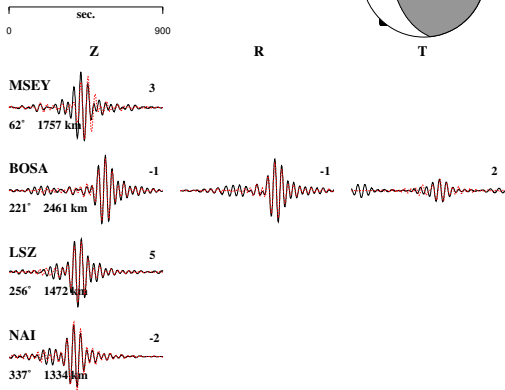
(# 02) DEMOCRATIC REP OF CONGO

Date: 29. 4.95 Time: 11:50:53.9 Lat: -1.30 Long: 28.60 Depth: 6
 Plane (strike/dip/slip) NP1: 229/22/-55 NP2: 12/71/-103
 Frequency range (Hz): .0200-.0290 Variance: 0.546 Mw: 5.4
 30% double couple



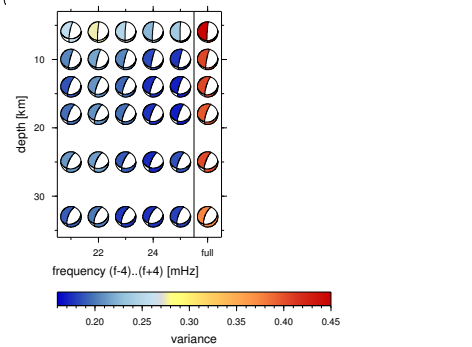
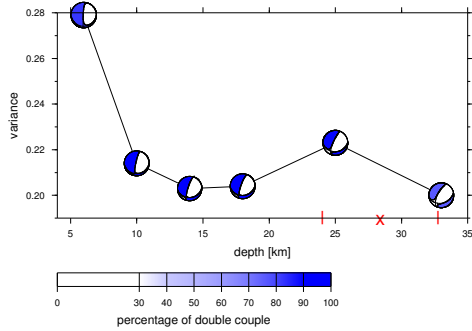
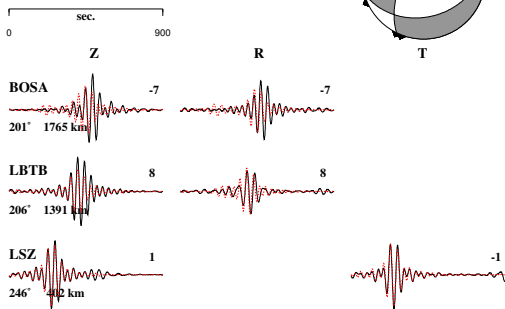
(# 03) NORTHWEST OF MADAGASCAR

Date: 20. 7.95 Time: 5: 8:28.4 Lat:-12.40 Long: 41.50 Depth: 18
 Plane (strike/dip/slip) NP1: 174/ 48/ 160 NP2: 277/ 75/ 43
 Frequency range (Hz): .0190-.0290 Variance: 0.191 Mw: 5.0
 60.2% double couple

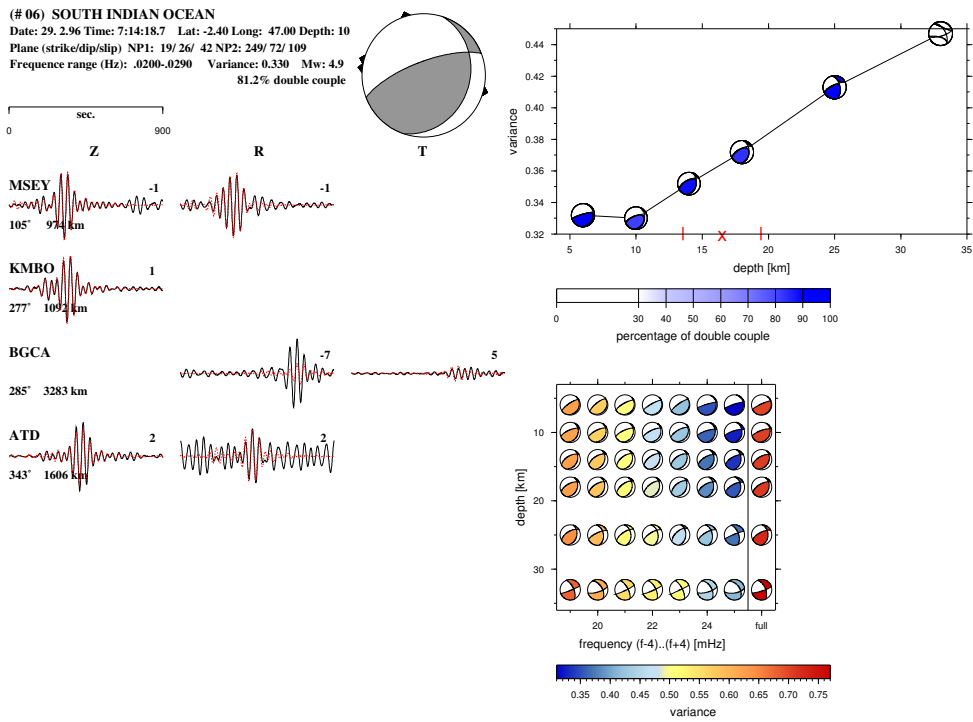
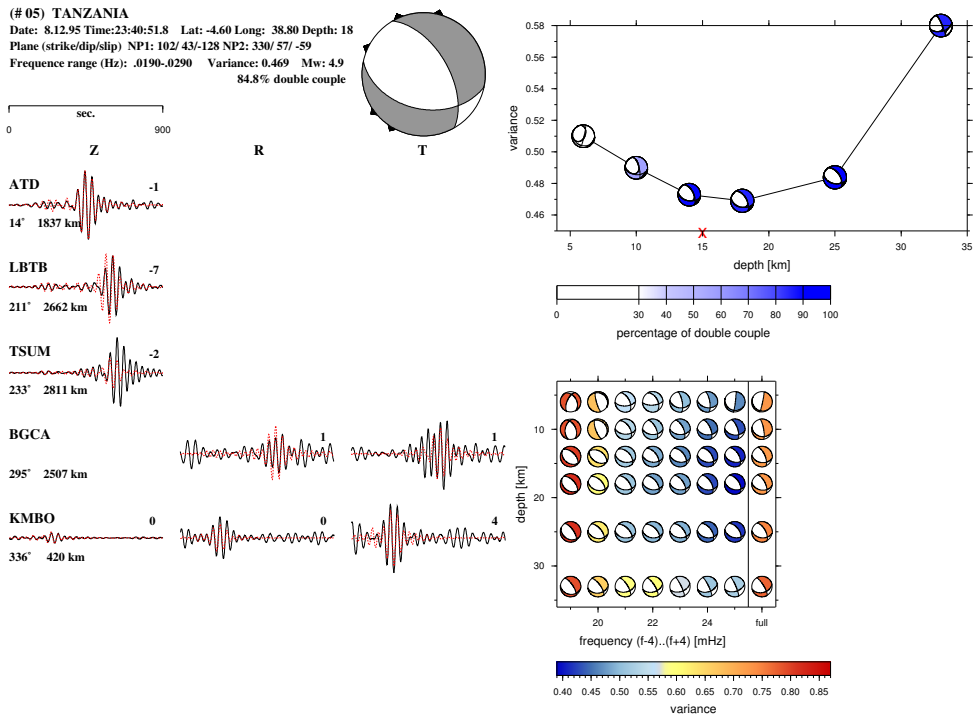


(# 04) ZAMBIA

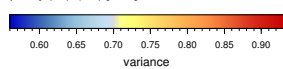
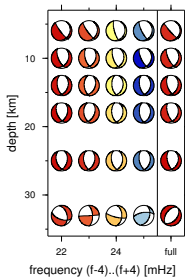
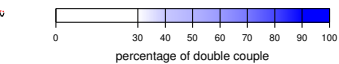
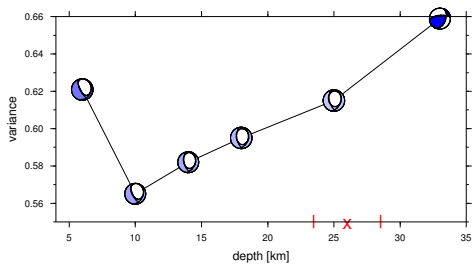
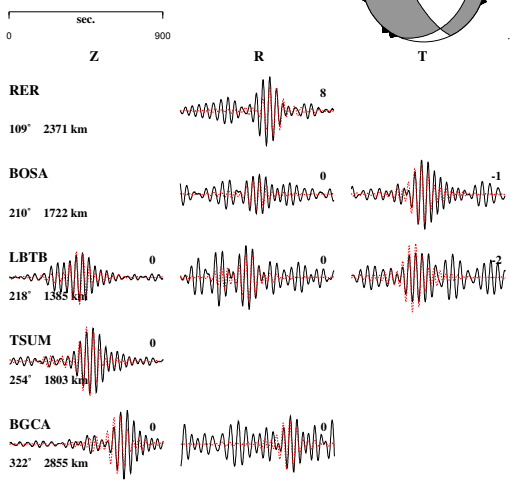
Date: 12.11.95 Time:19: 0: 9.8 Lat:-13.80 Long: 31.60 Depth: 33
 Plane (strike/dip/slip) NP1: 76/ 36/ -45 NP2: 206/ 64/-117
 Frequency range (Hz): .0170-.0290 Variance: 0.200 Mw: 5.3
 76.2% double couple



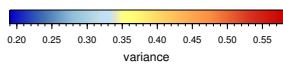
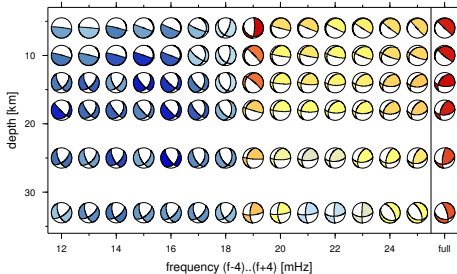
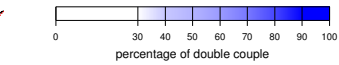
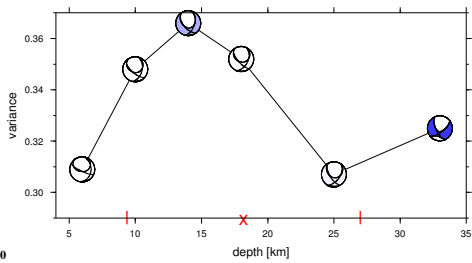
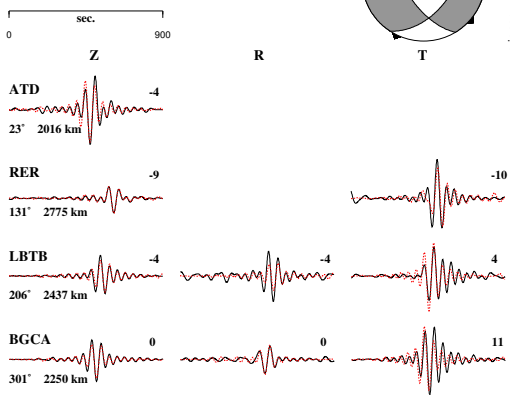
Appendix B. Figures of moment tensor inversion results



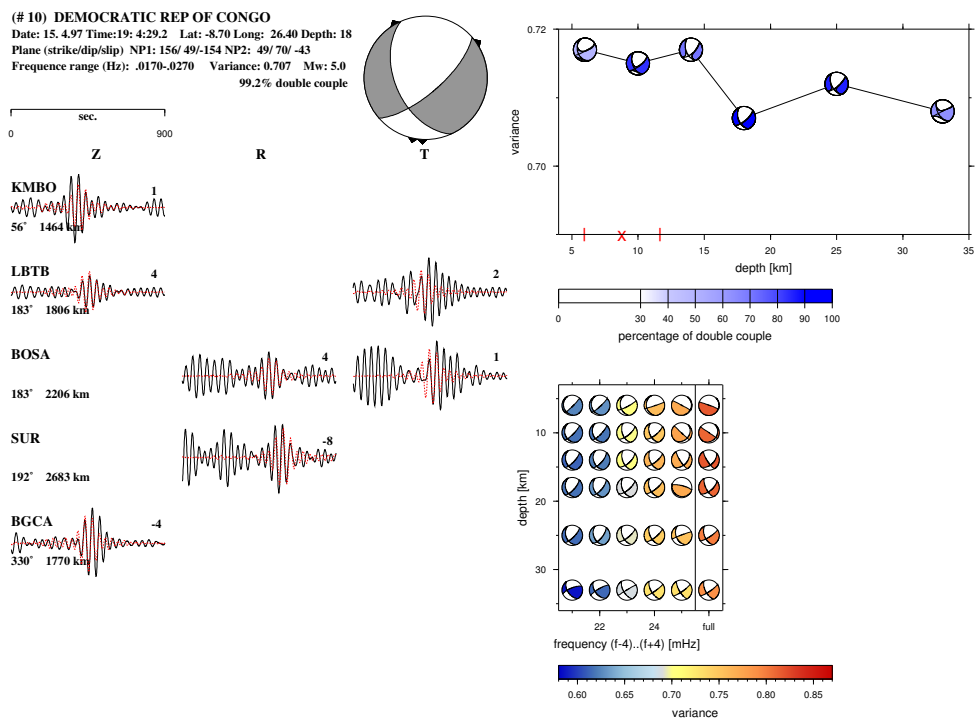
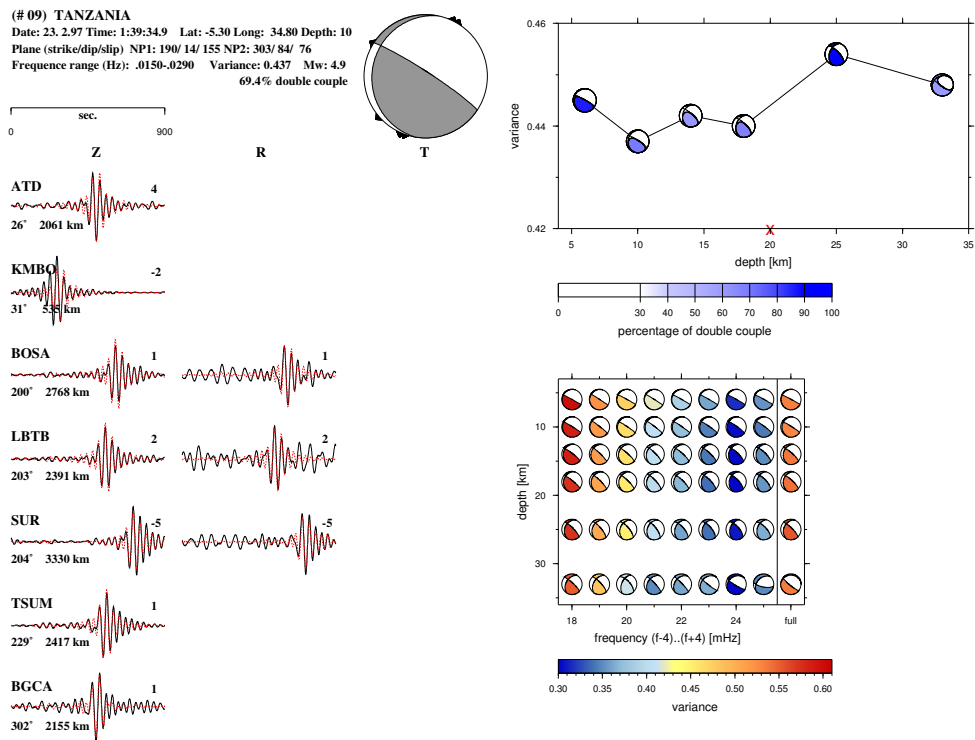
(# 07) MALAWI
 Date: 30. 8.96 Time: 6:58:45.2 Lat: -15.40 Long: 34.10 Depth: 10
 Plane (strike/dip/slip) NP1: 21/ 27/ -46 NP2: 154/ 70/-109
 Frequency range (Hz): .0210-.0290 Variance: 0.565 Mw: 4.5
 57% double couple



(# 08) TANZANIA
 Date: 21.12.96 Time: 8:34: 6.2 Lat: -5.30 Long: 35.80 Depth: 25
 Plane (strike/dip/slip) NP1: 33/ 49/ -37 NP2: 149/ 62/-133
 Frequency range (Hz): .0100-.0220 Variance: 0.307 Mw: 5.5
 32.2% double couple

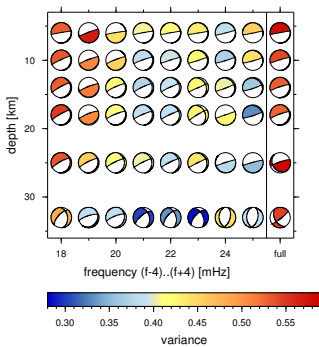
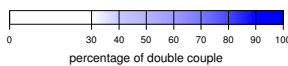
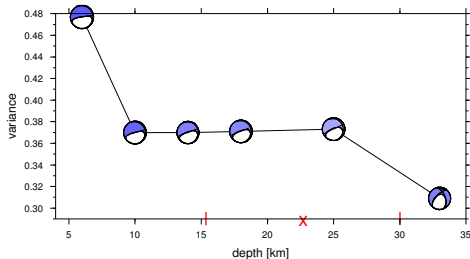
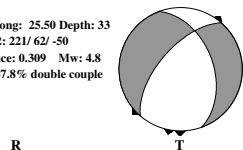
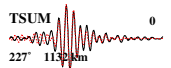
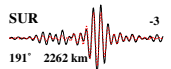
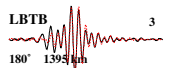
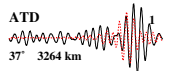
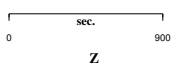


Appendix B. Figures of moment tensor inversion results



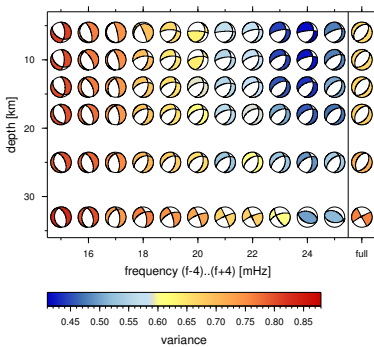
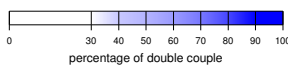
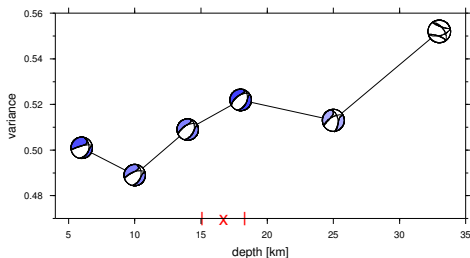
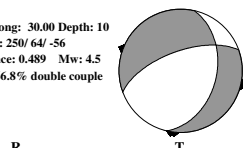
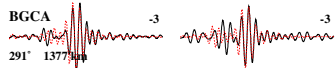
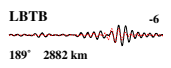
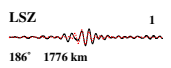
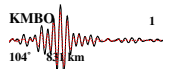
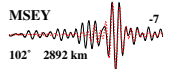
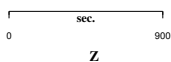
(# 11) ZAMBIA

Date: 12. 4.98 Time:10:49: 0.8 Lat:-12.40 Long: 25.50 Depth: 33
 Plane (strike/dip/slip) NP1: 340/ 46/-141 NP2: 221/ 62/ -50
 Frequency range (Hz): .0170-.0270 Variance: 0.309 Mw: 4.8
 67.8% double couple

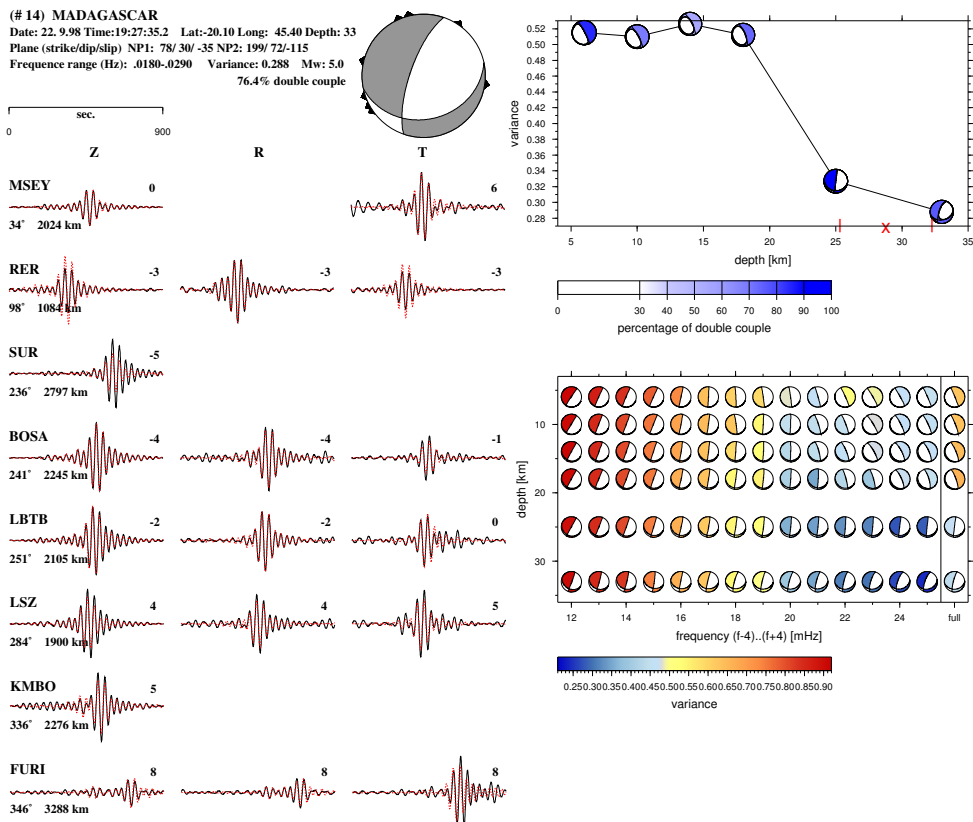
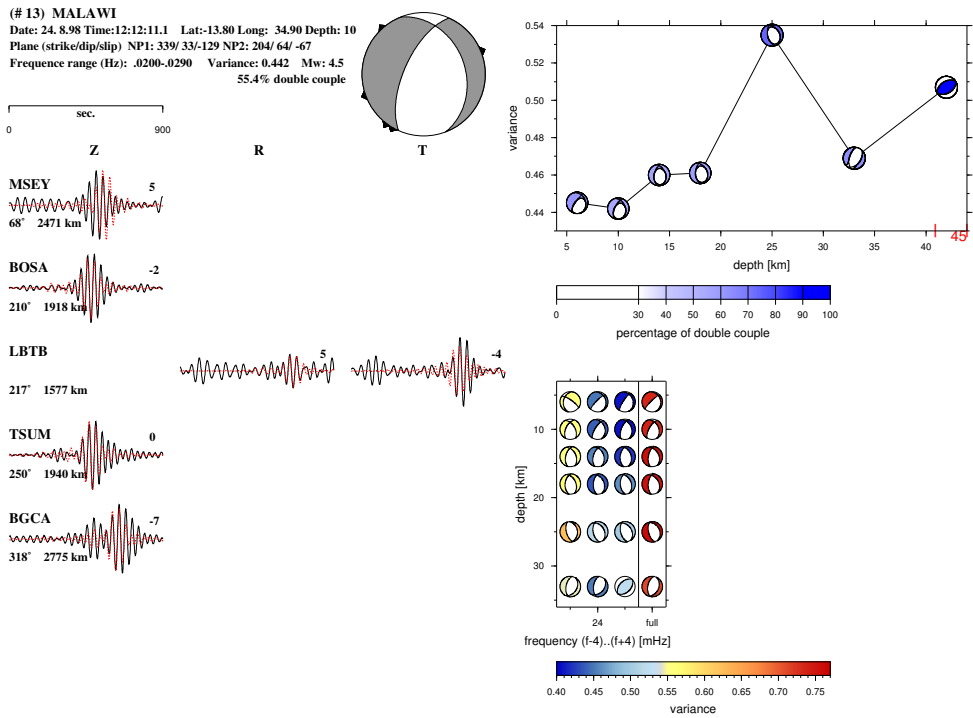


(# 12) UGANDA

Date: 15. 8.98 Time:17:29:19.0 Lat: 0.70 Long: 30.00 Depth: 10
 Plane (strike/dip/slip) NP1: 13/ 41/-138 NP2: 250/ 64/ -56
 Frequency range (Hz): .0190-.0290 Variance: 0.489 Mw: 4.5
 66.8% double couple

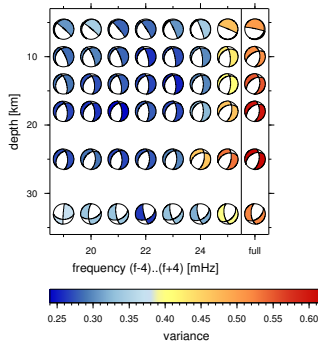
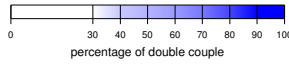
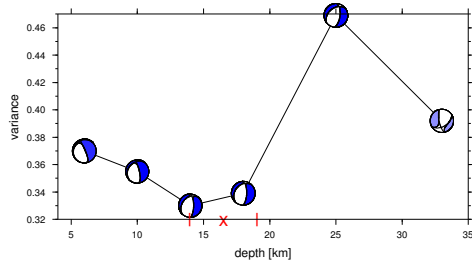
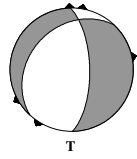
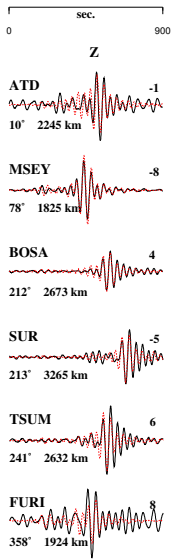


Appendix B. Figures of moment tensor inversion results



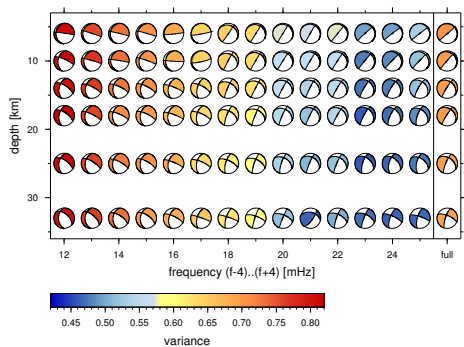
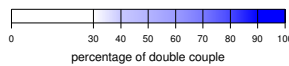
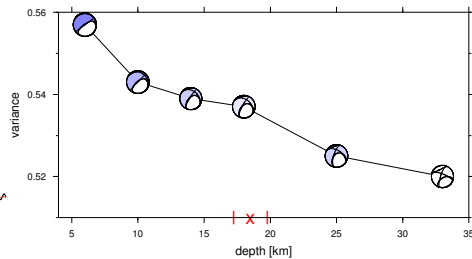
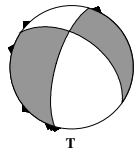
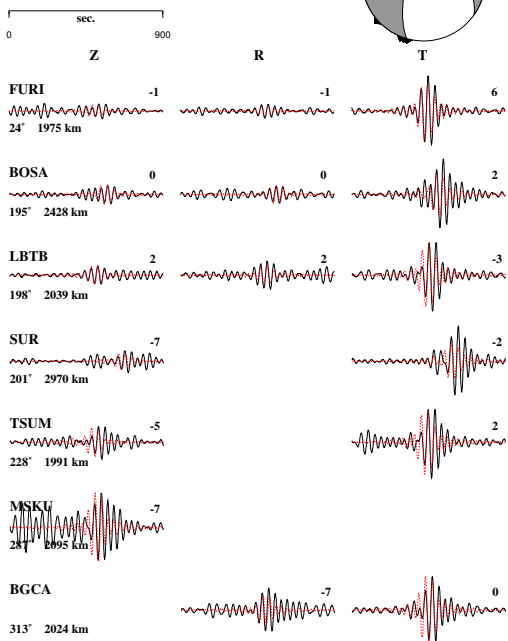
(# 15) TANZANIA

Date: 6. 4.99 Time: 4:16:47.0 Lat: -8.50 Long: 39.40 Depth: 14
 Plane (strike/dip/slip) NP1: 223/31/-50 NP2: 359/66/-110
 Frequency range (Hz): .0150-.0280 Variance: 0.330 Mw: 5.0
 92.2% double couple



(# 16) LAKE TANGANYIKA REGION

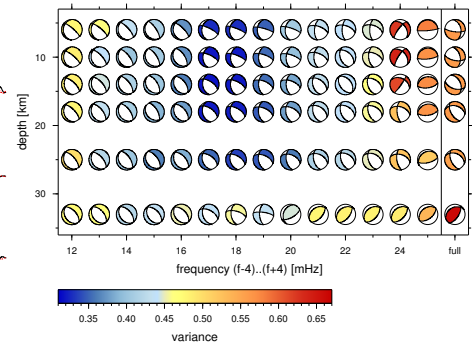
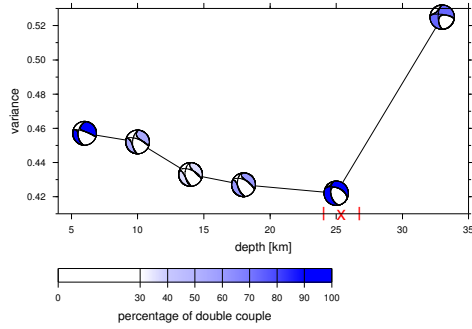
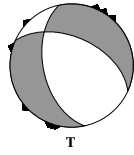
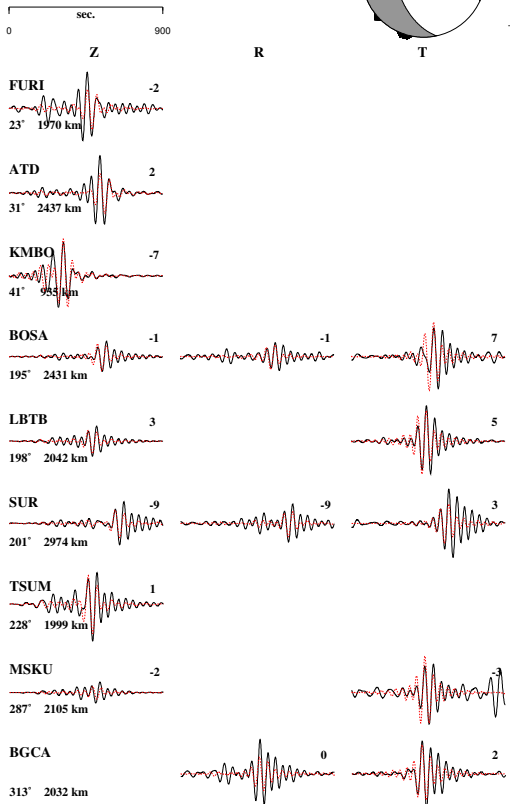
Date: 7. 5.99 Time: 2:10:45.1 Lat: -7.50 Long: 31.60 Depth: 25
 Plane (strike/dip/slip) NP1: 305/48/-152 NP2: 196/69/-44
 Frequency range (Hz): .0190-.0290 Variance: 0.525 Mw: 4.8
 38% double couple



Appendix B. Figures of moment tensor inversion results

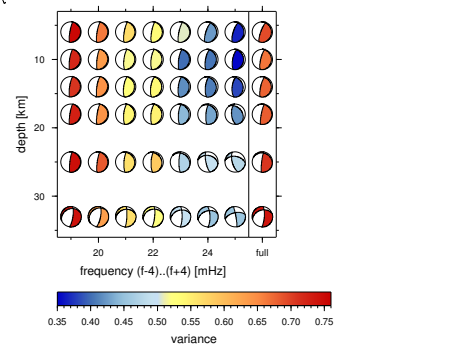
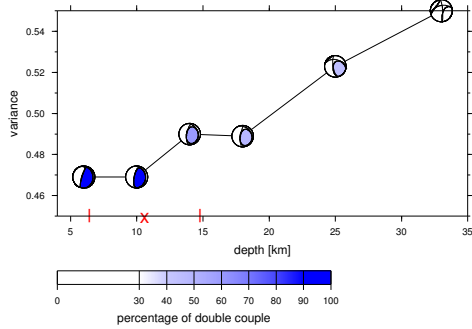
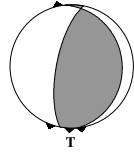
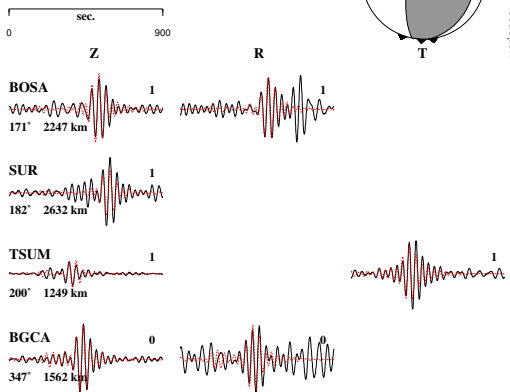
(# 17) LAKE TANGANYIKA REGION

Date: 7. 5.99 Time:14: 7:32.9 Lat: -7.50 Long: 31.70 Depth: 25
 Plane (strike/dip/slip) NP1: 294/ 52/-130 NP2: 168/ 52/ -50
 Frequency range (Hz): .0130-.0240 Variance: 0.422 Mw: 5.2
 91% double couple



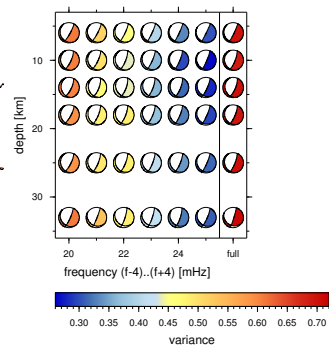
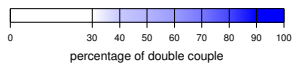
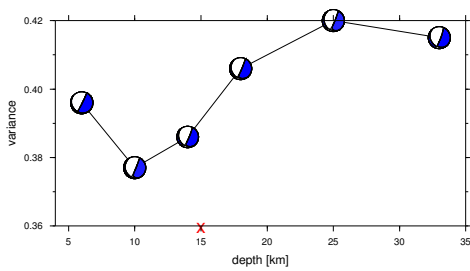
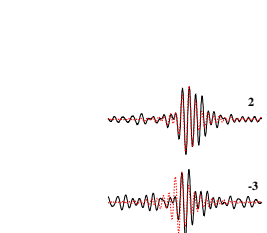
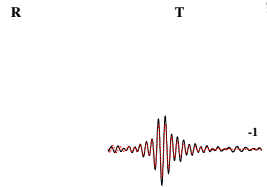
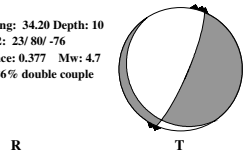
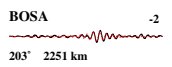
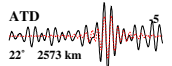
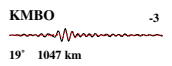
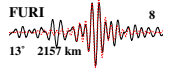
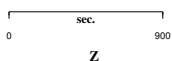
(# 18) ANGOLA

Date: 6. 8.99 Time:17:22:48.8 Lat: -8.60 Long: 21.60 Depth: 10
 Plane (strike/dip/slip) NP1: 354/ 19/ 73 NP2: 191/ 70/ 95
 Frequency range (Hz): .0170-.0290 Variance: 0.469 Mw: 4.6
 94% double couple



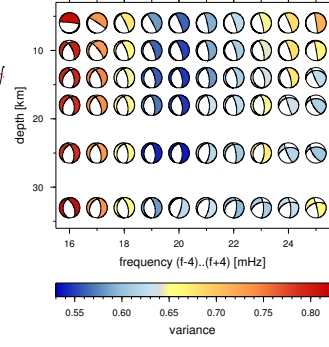
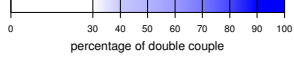
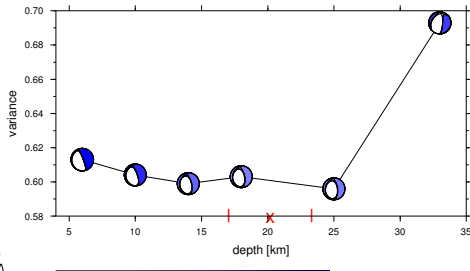
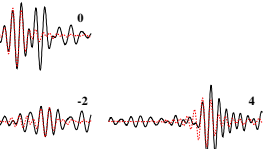
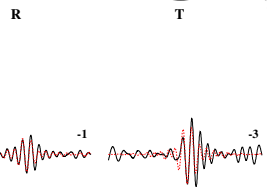
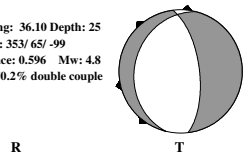
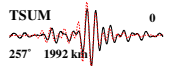
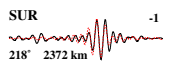
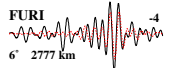
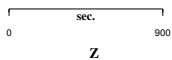
(# 19) MALAWI

Date: 1. 9.99 Time: 4: 7:56.5 Lat:-10.10 Long: 34.20 Depth: 10
 Plane (strike/dip/slip) NP1: 147/16/-144 NP2: 23/80/-76
 Frequency range (Hz): .0180-.0290 Variance: 0.377 Mw: 4.7
 86% double couple

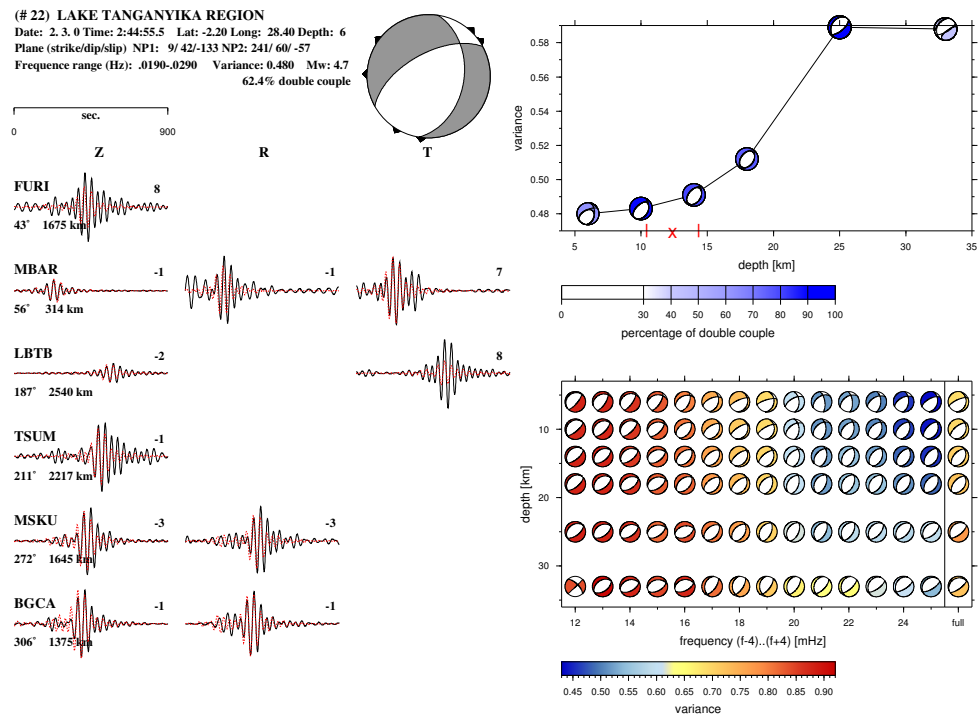
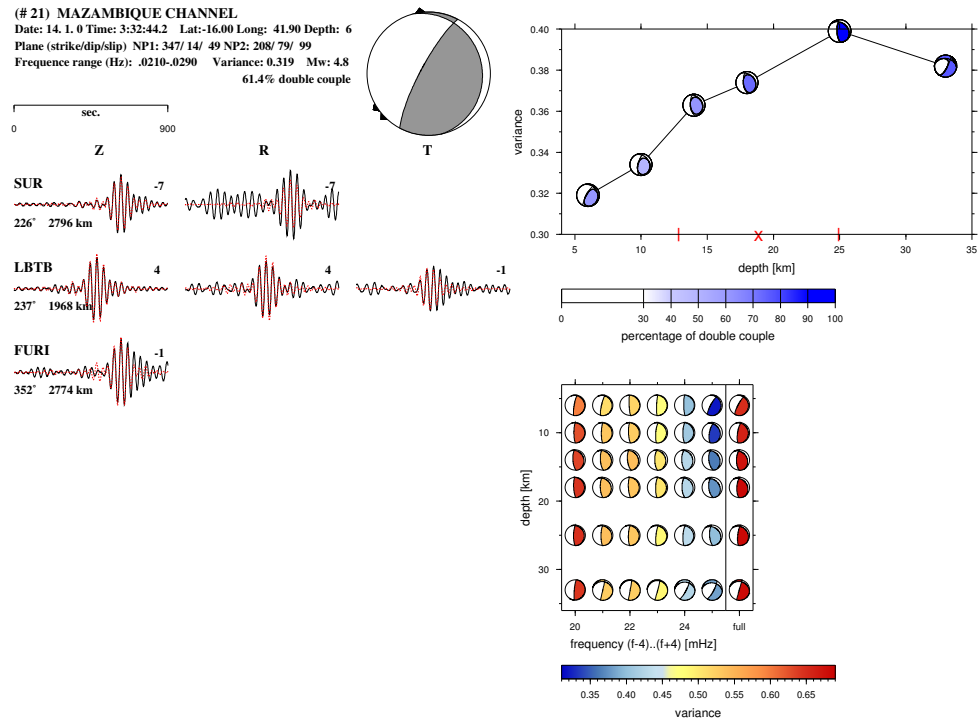


(# 20) MOZAMBIQUE

Date: 4. 1. 0 Time: 0:25: 9.4 Lat:-16.10 Long: 36.10 Depth: 25
 Plane (strike/dip/slip) NP1: 194/26/-70 NP2: 353/65/-99
 Frequency range (Hz): .0150-.0240 Variance: 0.596 Mw: 4.8
 70.2% double couple

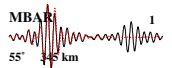
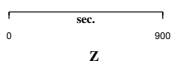


Appendix B. Figures of moment tensor inversion results



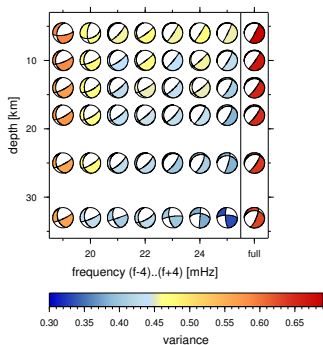
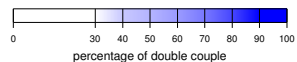
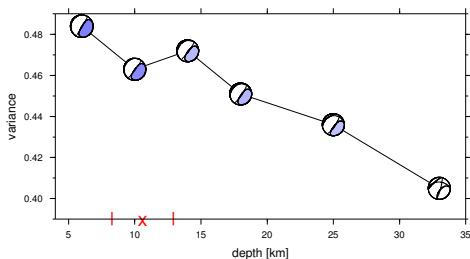
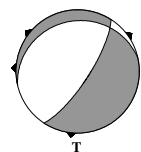
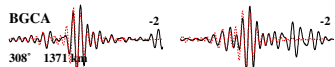
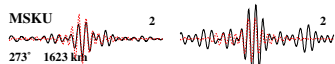
(# 23) LAKE TANGANYIKA REGION

Date: 2. 3. 0 Time: 4:29:50.2 Lat: -2.40 Long: 28.20 Depth: 25
 Plane (strike/dip/slip) NP1: 257/19/-47 NP2: 33/75/-103
 Frequency range (Hz): .0170-.0280 Variance: 0.436 Mw: 4.7
 43.4% double couple



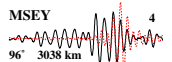
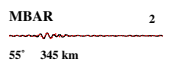
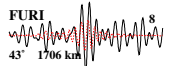
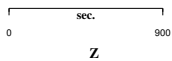
LBTB

186° 2516 km



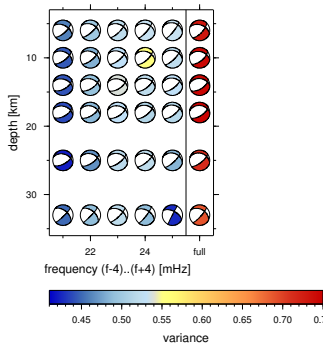
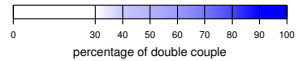
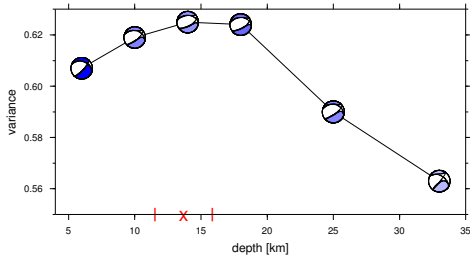
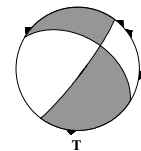
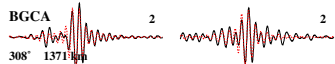
(# 24) LAKE TANGANYIKA REGION

Date: 3. 3. 0 Time: 5: 3:22.3 Lat: -2.40 Long: 28.20 Depth: 33
 Plane (strike/dip/slip) NP1: 301/47/-8 NP2: 37/83/-137
 Frequency range (Hz): .0170-.0290 Variance: 0.563 Mw: 4.6
 48.6% double couple



LBTB

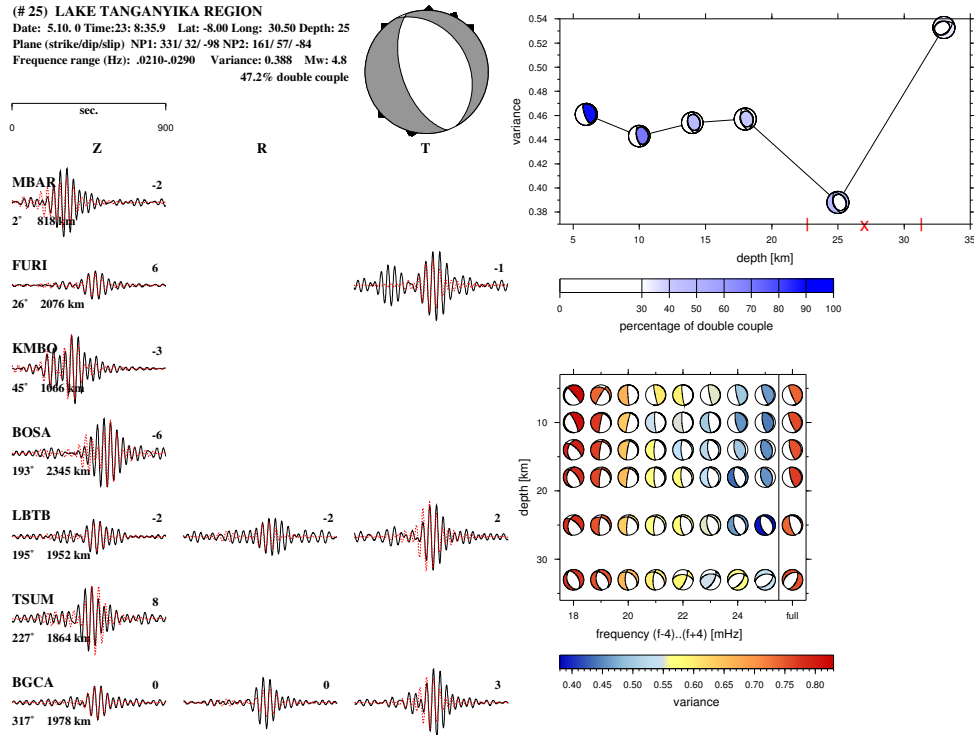
186° 2516 km



Appendix B. Figures of moment tensor inversion results

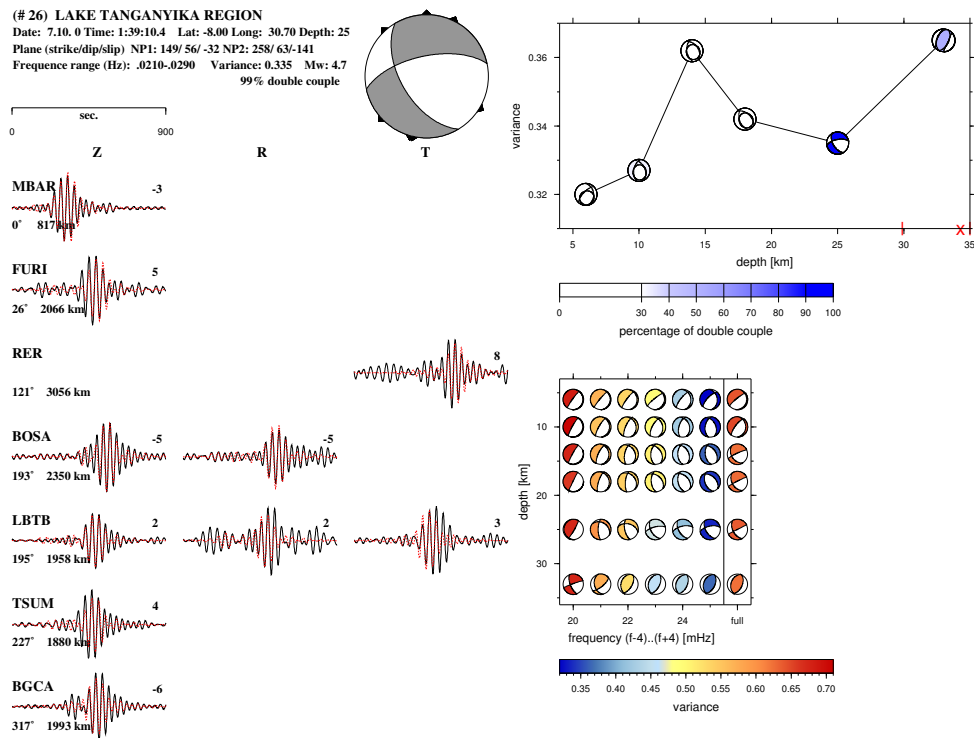
(# 25) LAKE TANGANYIKA REGION

Date: 5.10.0 Time:23:8:35.9 Lat: -8.00 Long: 30.50 Depth: 25
 Plane (strike/dip/slip) NP1: 331/32/-98 NP2: 161/57/-84
 Frequency range (Hz): .0210-.0290 Variance: 0.388 Mw: 4.8
 47.2% double couple



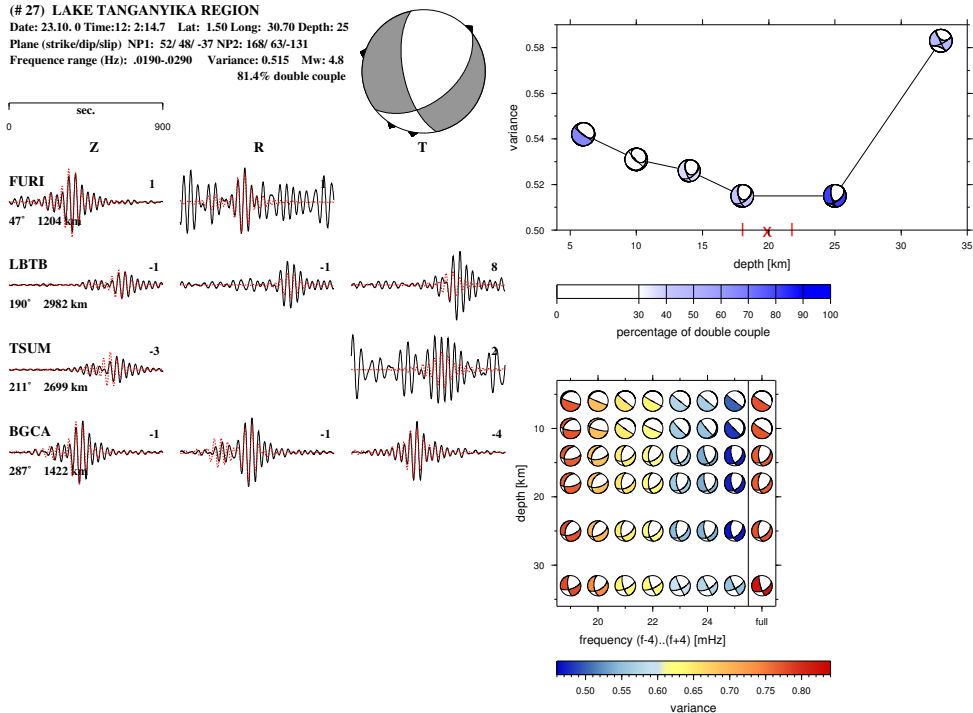
(# 26) LAKE TANGANYIKA REGION

Date: 7.10.0 Time:1:39:10.4 Lat: -8.00 Long: 30.70 Depth: 25
 Plane (strike/dip/slip) NP1: 149/56/-32 NP2: 258/63/-141
 Frequency range (Hz): .0210-.0290 Variance: 0.335 Mw: 4.7
 99% double couple



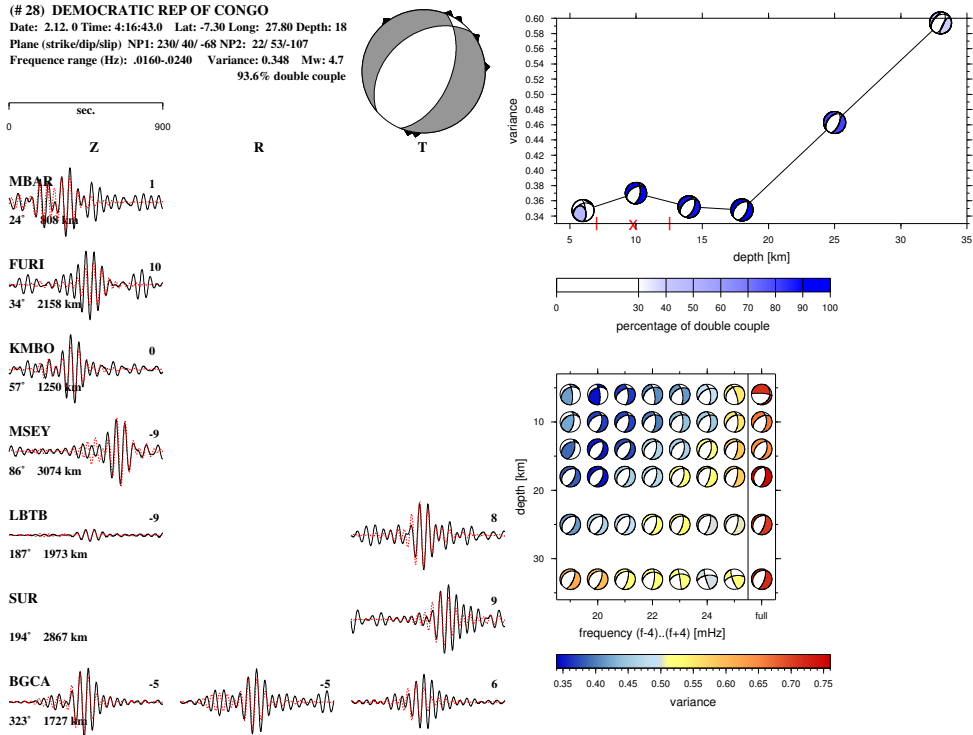
(# 27) LAKE TANGANYIKA REGION

Date: 23.10. 0 Time: 12:2:14.7 Lat: 1.50 Long: 30.70 Depth: 25
 Plane (strike/dip/slip) NP1: 52/ 48/ -37 NP2: 168/ 63/-131
 Frequency range (Hz): .0190-.0290 Variance: 0.515 Mw: 4.8
 81.4% double couple

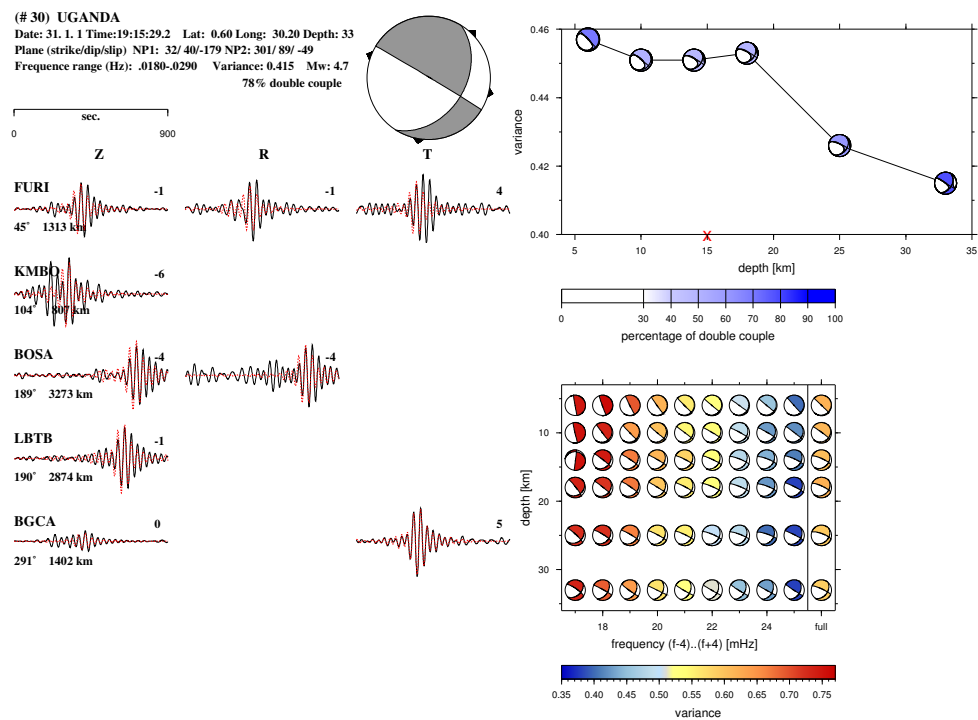
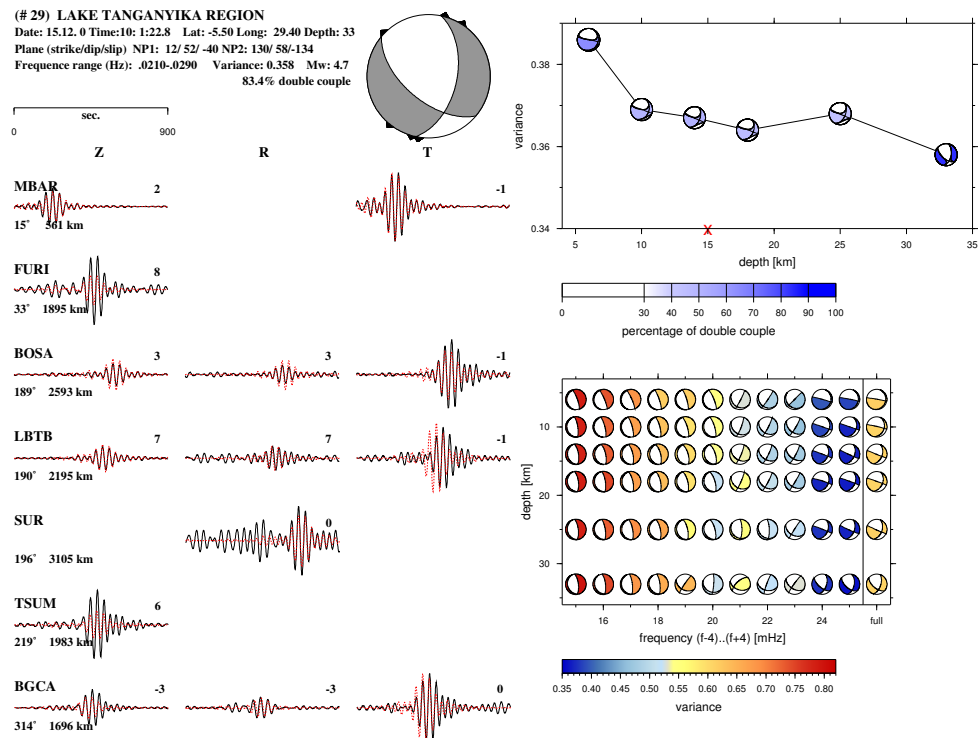


(# 28) DEMOCRATIC REP OF CONGO

Date: 2.12. 0 Time: 4:16:43.0 Lat: -7.30 Long: 27.80 Depth: 18
 Plane (strike/dip/slip) NP1: 230/ 40/ -68 NP2: 22/ 53/-107
 Frequency range (Hz): .0160-.0240 Variance: 0.348 Mw: 4.7
 93.6% double couple

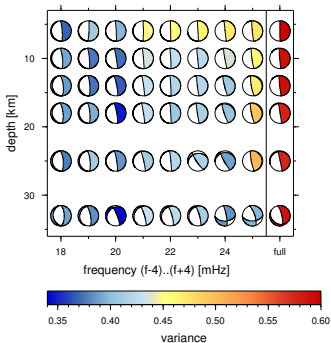
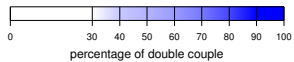
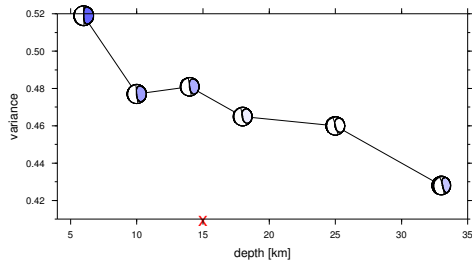
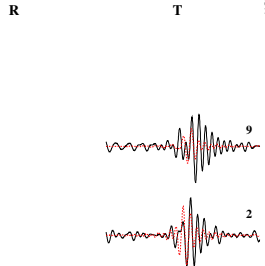
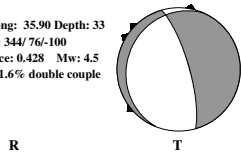
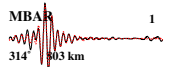
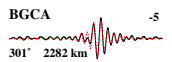
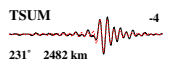
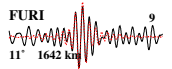
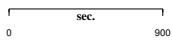


Appendix B. Figures of moment tensor inversion results



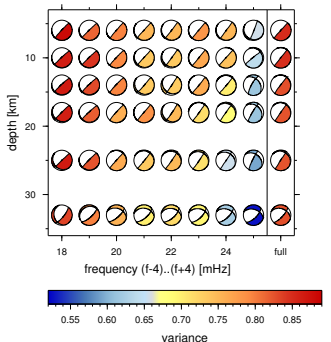
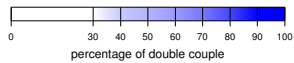
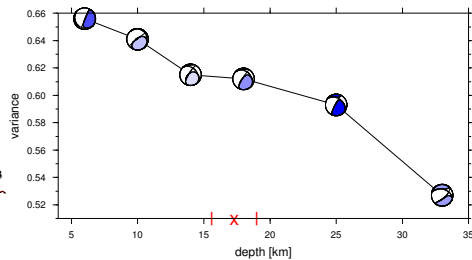
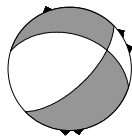
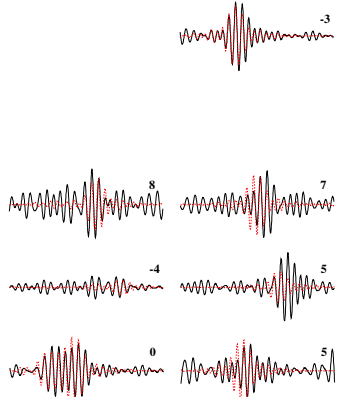
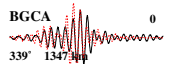
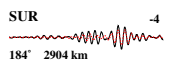
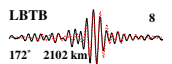
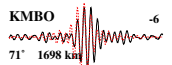
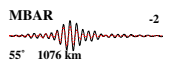
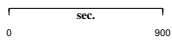
(# 31) TANZANIA

Date: 25. 3. 1 Time: 18:54:14.2 Lat: -5.70 Long: 35.90 Depth: 33
 Plane (strike/dip/slip) NP1: 202/17/-53 NP2: 344/76/-100
 Frequency range (Hz): .0150-.0280 Variance: 0.428 Mw: 4.5
 41.6% double couple



(# 32) DEMOCRATIC REP OF CONGO

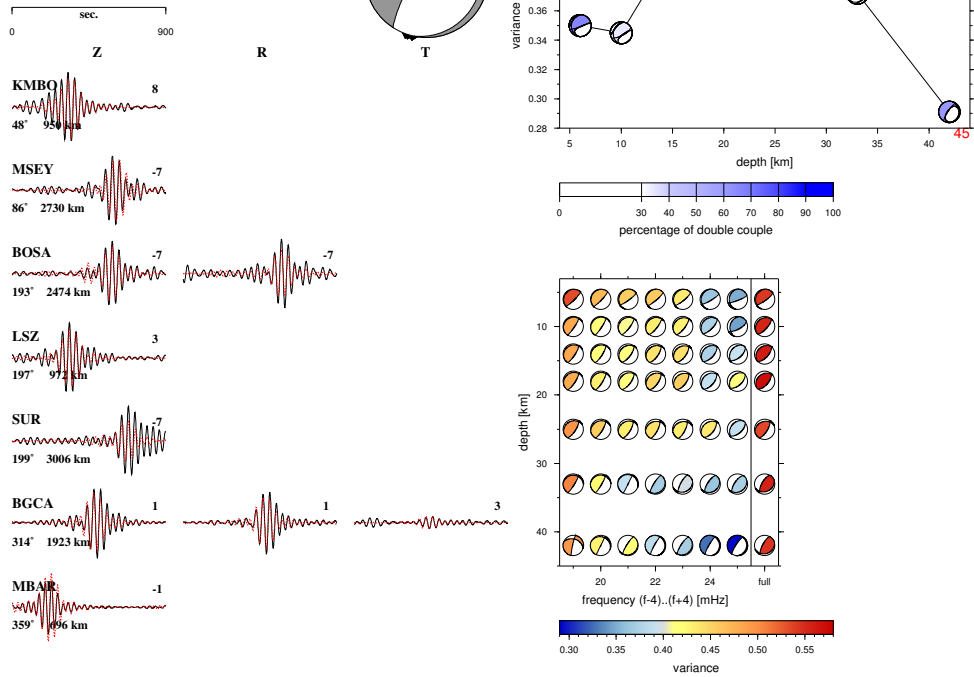
Date: 17. 4. 1 Time: 4:39:3.4 Lat: -6.20 Long: 22.80 Depth: 33
 Plane (strike/dip/slip) NP1: 287/43/-37 NP2: 46/65/-126
 Frequency range (Hz): .0210-.0290 Variance: 0.527 Mw: 4.6
 59.8% double couple



Appendix B. Figures of moment tensor inversion results

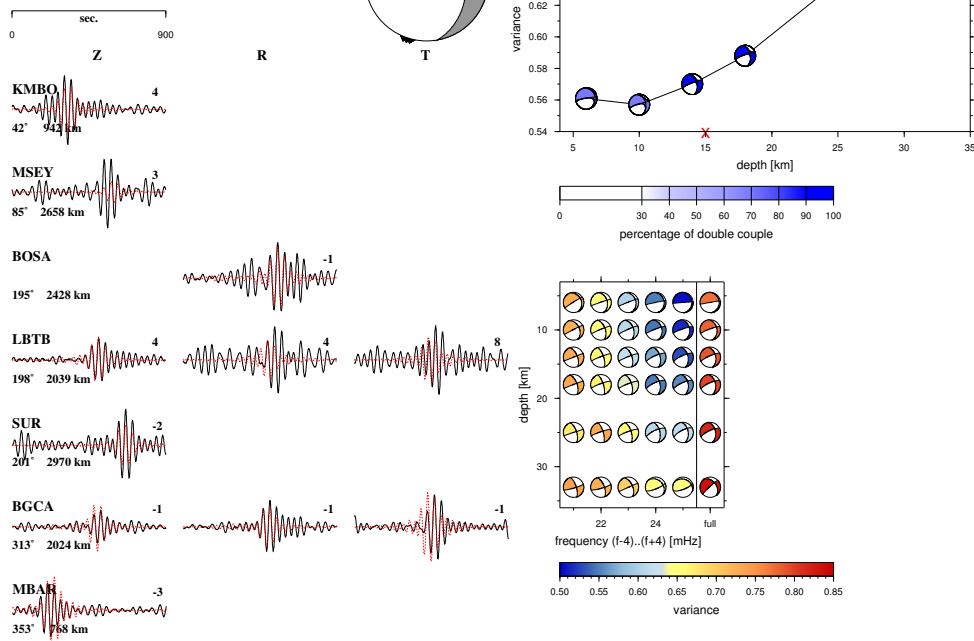
(# 33) LAKE TANGANYIKA REGION

Date: 13. 7. 1 Time: 19:24: 2.4 Lat: -6.90 Long: 30.90 Depth: 42
 Plane (strike/dip/slip) NP1: 12/12/-110 NP2: 213/77/-85
 Frequency range (Hz): .0210-.0290 Variance: 0.291 Mw: 4.6
 61.2% double couple



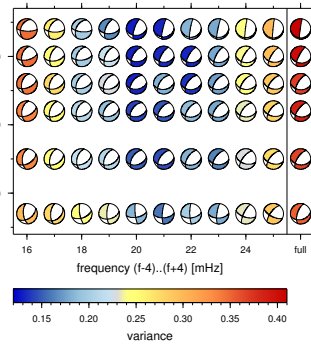
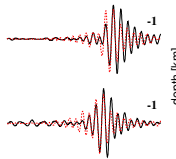
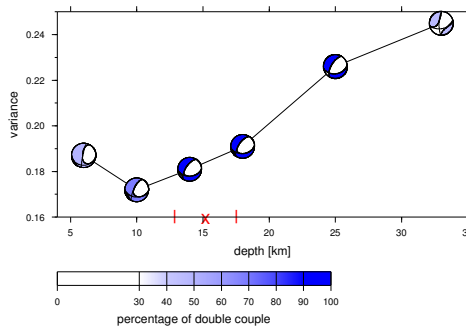
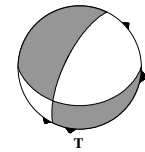
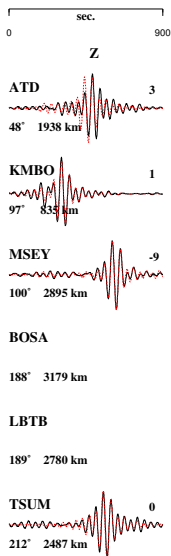
(# 34) LAKE TANGANYIKA REGION

Date: 18. 9. 1 Time: 11: 1: 2.1 Lat: -7.50 Long: 31.60 Depth: 10
 Plane (strike/dip/slip) NP1: 350/37/-169 NP2: 251/83/-53
 Frequency range (Hz): .0190-.0290 Variance: 0.557 Mw: 4.4
 69.8% double couple



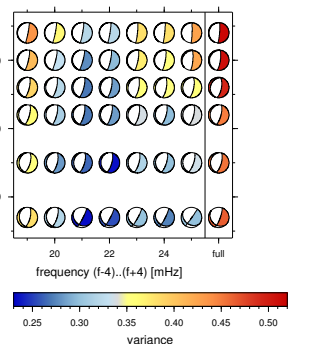
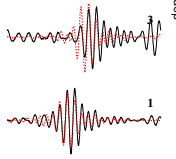
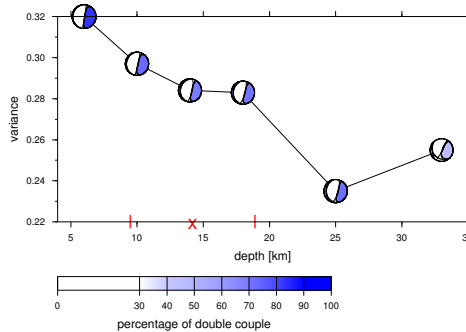
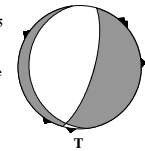
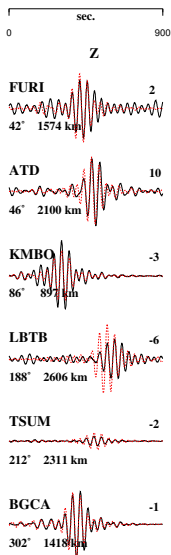
(# 35) DEMOCRATIC REP OF CONGO

Date: 4. 1. 2 Time:13: 2:21.2 Lat: -0.20 Long: 29.80 Depth: 10
 Plane (strike/dip/slip) NP1: 90/38/-32 NP2: 206/70/-123
 Frequency range (Hz): .0150-.0260 Variance: 0.172 Mw: 5.2
 69% double couple



(# 36) LAKE TANGANYIKA REGION

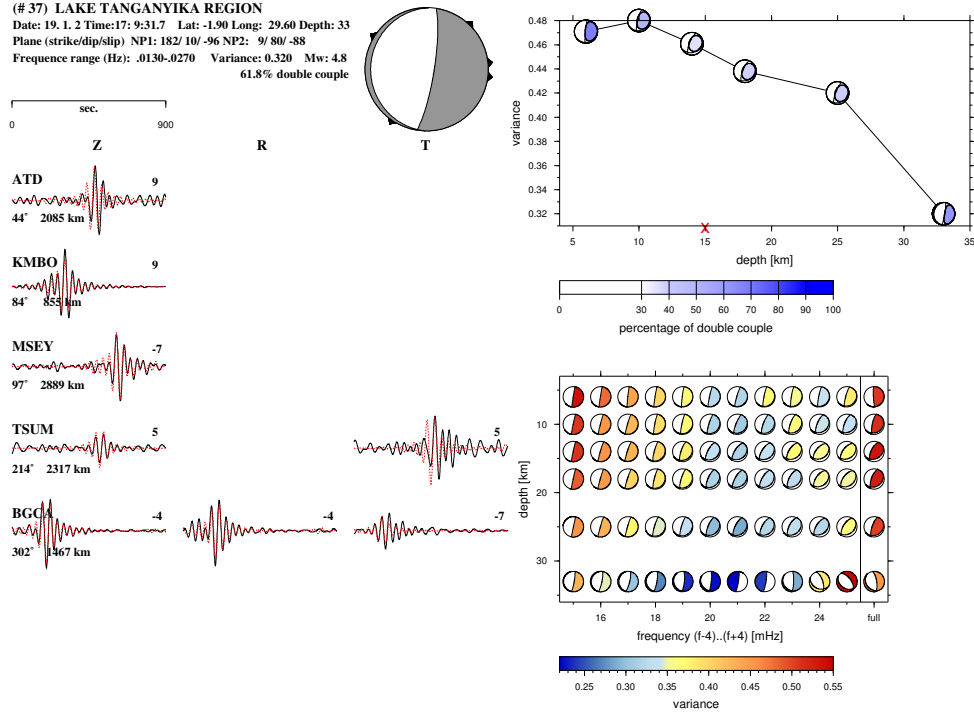
Date: 17. 1. 2 Time:20: 1:30.7 Lat: -1.70 Long: 29.20 Depth: 25
 Plane (strike/dip/slip) NP1: 173/19/-111 NP2: 16/71/-82
 Frequency range (Hz): .0180-.0260 Variance: 0.235 Mw: 5.0
 71.6% double couple



Appendix B. Figures of moment tensor inversion results

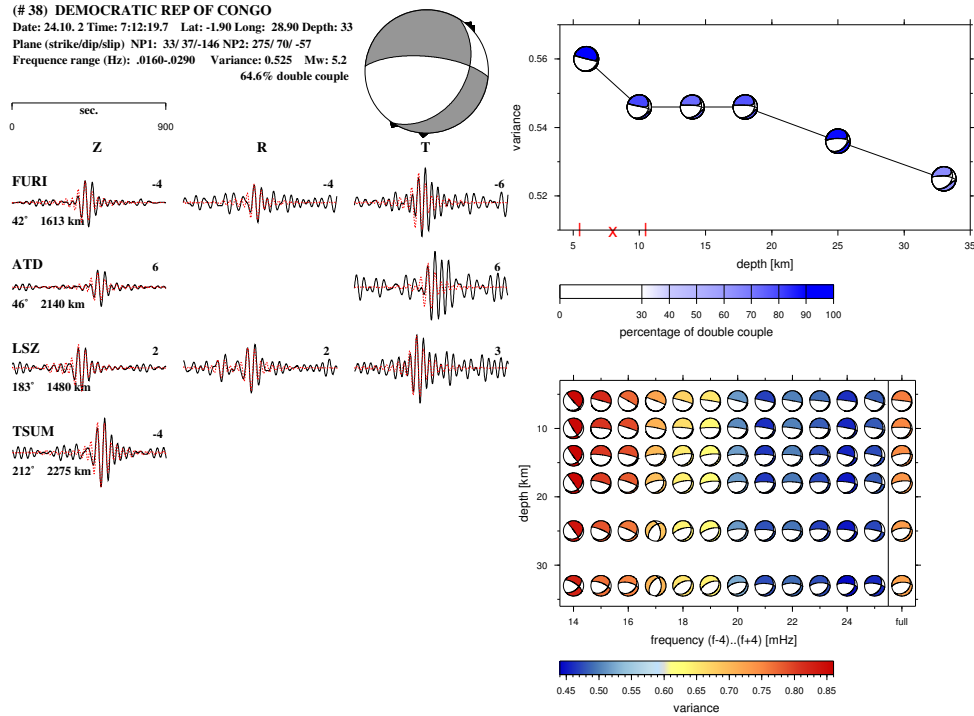
(# 37) LAKE TANGANYIKA REGION

Date: 19. 1. 2 Time: 17: 9: 31. 7 Lat: -1. 90 Long: 29. 60 Depth: 33
 Plane (strike/dip/slip) NP1: 182/ 10/ -96 NP2: 9/ 80/ -88
 Frequency range (Hz): .0130-.0270 Variance: 0.320 Mw: 4.8
 61.8% double couple



(# 38) DEMOCRATIC REP OF CONGO

Date: 24.10. 2 Time: 7: 12: 19. 7 Lat: -1. 90 Long: 28. 90 Depth: 33
 Plane (strike/dip/slip) NP1: 33/ 37/ -146 NP2: 275/ 70/ -57
 Frequency range (Hz): .0160-.0290 Variance: 0.525 Mw: 5.2
 64.6% double couple



Appendix C

Equivalent forces

In section 2.1 the equivalent force densities \mathbf{f} and \mathbf{t} were introduced as the representation of the internal forces of a rupture process (eqn. 2.13):

$$\mathbf{f} = -\nabla \cdot \mathbf{\Gamma}, \quad \mathbf{t} = \hat{\mathbf{n}} \cdot \mathbf{\Gamma}. \quad (\text{C.1})$$

The following derivation will show that these force densities do satisfy the conservation of momentum and angular momentum in the case of a symmetric stress glut tensor $\mathbf{\Gamma}$. Figure C.1 illustrates a source volume V_F with a surface S_F that cuts the earth surface on a rupture are R_F . Since Hook's law (eqn. 2.11) is valid everywhere but in the source volume V_F and on the surface rupture area R_F , the stress glut $\mathbf{\Gamma}$ is zero elsewhere, including the surface of the buried source $S_F - R_F$:

$$\mathbf{\Gamma} \neq \mathbf{0} \text{ in } V_F \text{ and } R_F, \quad \mathbf{\Gamma} = \mathbf{0} \text{ elsewhere including } S_F - R_F. \quad (\text{C.2})$$

Hence the applied net force \mathbf{F} is:

$$\mathbf{F} = \int_{V_F} \mathbf{f} dV + \int_{R_F} \mathbf{t} dS. \quad (\text{C.3})$$

Using Gauss' theorem and including equations C.1 and C.2 yields:

$$\mathbf{F} = - \int_{V_F} \nabla \cdot \mathbf{\Gamma} dV + \int_{R_F} \hat{\mathbf{n}} \cdot \mathbf{\Gamma} dS = - \int_{S_F - R_F} \hat{\mathbf{n}} \cdot \mathbf{\Gamma} dS = \mathbf{0}. \quad (\text{C.4})$$

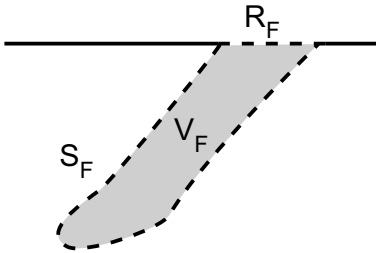


Figure C.1: Schematic illustration of an arbitrary earthquake source volume V_F with surface S_F and intersection R_F of the earth's surface (vertical cross-section).

I.e. no net force is applied on the earth. The net torque N is:

$$\mathbf{N} = \int_{V_F} \mathbf{x} \times \mathbf{f} dV + \int_{R_F} \mathbf{x} \times \mathbf{t} dS. \quad (\text{C.5})$$

Inserting equation C.1, the first term is:

$$\begin{aligned} (\mathbf{x} \times \mathbf{f})_i &= -(\mathbf{x} \times \nabla \Gamma)_i \\ &= -\varepsilon_{ijk} x_j (\nabla \Gamma)_k \\ &= -\varepsilon_{ijk} x_j (\partial_l \Gamma_{lk}) \\ &= \varepsilon_{ijk} (\partial_l \Gamma_{lj}) x_k \\ &= \partial_l (\varepsilon_{ijk} \Gamma_{lj} x_k) - \varepsilon_{ijk} (\partial_l x_k) \Gamma_{lj} \\ &= \partial_l (\Gamma \times \mathbf{x})_{li} - \varepsilon_{ijk} \Gamma_{jk} \\ &= [\nabla \cdot (\Gamma \times \mathbf{x})]_i - (\wedge \Gamma)_i, \end{aligned} \quad (\text{C.6})$$

with the wedge operator (\wedge) defined as:

$$\wedge \Gamma = \varepsilon_{ijk} \Gamma_{jk}. \quad (\text{C.7})$$

Applying Gauss' theorem and the result of equation C.6 on equation C.5 gives:

$$\begin{aligned} \mathbf{N} &= - \int_{V_F} \mathbf{x} \times \nabla \Gamma dV + \int_{R_F} \mathbf{x} \times \hat{\mathbf{n}} \cdot \Gamma dS \\ &= \int_{V_F} (\nabla \cdot (\Gamma \times \mathbf{x}) - \wedge \Gamma) dV + \int_{R_F} \mathbf{x} \times \hat{\mathbf{n}} \cdot \Gamma dS \\ &= - \int_{V_F} \wedge \Gamma dV + \int_{S_F} \hat{\mathbf{n}} \cdot (\Gamma \times \mathbf{x}) + \int_{R_F} \mathbf{x} \times \hat{\mathbf{n}} \cdot \Gamma dS \\ &= - \int_{V_F} \wedge \Gamma dV - \int_{S_F - R_F} \mathbf{x} \times \hat{\mathbf{n}} \cdot \Gamma dS = \mathbf{0}. \end{aligned} \quad (\text{C.8})$$

The second term equals zero because of equation C.2. Since the earthquake, represented by the equivalent forces, does not exert any net force or net torque upon the earth, the first term must vanish as well, that is identical to the condition of a symmetric stress glut tensor Γ :

$$\wedge \Gamma = \varepsilon_{ijk} \Gamma_{jk} = \mathbf{0} \quad \iff \quad (\Gamma)^T = \Gamma. \quad (\text{C.9})$$

Acknowledgements

Credits for data and software

The seismic waveforms were provided by the networks of GEOFON, GEOSCOPE, GSN and GTSN, available online via the *IRIS*-datacenter Washington (<http://www.iris.edu/SeismicQuery/>) or using the *BREQ_FAST* e-mail client as done in this work. Seismic data was processed with *SeismicHandler* (Stammler, 1993) and inverted for the moment tensor by the *gminl*-software (Giardini, 1992). The majority of the figures were made using *GMT* (Wessel and Smith, 1998).

Persönliche Danksagung

Ich bedanke mich bei Prof. Friedemann Wenzel für die Betreuung meiner Arbeit, besonders für gute Ideen sowie die Unterstützung bei Planung und Vorgehensweise. Prof. Domenico Giardini danke ich für die Übernahme des Korreferats, die Bereitstellung des ursprünglichen Programmcodes zur Momententensorinversion und einen kritischen Blick für seismische Wellenformen.

Für technische Hilfe und die Einführung in die Momententensorinversion danke ich Dr. Purnchandra Rao, Dr. Jochen Braunmiller und Dr. Fabrizio Bernardi. Viele anregende Diskussionen habe ich mit Dr. Oliver Heidbach geführt, der geophysikalische Fragestellungen auf den Punkt und mich zum Hinterfragen gebracht hat, Danke. Ihm und PD Dr. Joachim Ritter danke ich auch für das Durchsehen dieser Arbeit. Darüber hinaus danke ich PD Dr. Joachim Ritter, Thies Buchmann, Andreas Eckert, Dr. Olivier Sèbe und Prof. Karl Fuchs für viele erhellende Diskussionen. Insgesamt gebührt allen Mitarbeitern und Studenten der Arbeitsgruppe „Tektonische Spannungen“ und dem ganzen Geophysikalischen Institut Dank für eine angenehme Atmosphäre.

Danke Sandra, für Deine Anwesenheit, Dein Verständnis und das Leben zwischen *CTG*'s und *CMT*'s!